The University of Maine
DigitalCommons@UMaine

Honors College

Spring 2019

VHF Near Field Antenna Design for Wireless Sensing Applications in Harsh Environments

Nicholas Aiken
University of Maine

Follow this and additional works at: https://digitalcommons.library.umaine.edu/honors

 Part of the Electrical and Computer Engineering Commons

Recommended Citation

Aiken, Nicholas, "VHF Near Field Antenna Design for Wireless Sensing Applications in Harsh Environments" (2019). *Honors College*. 493.
https://digitalcommons.library.umaine.edu/honors/493

This Honors Thesis is brought to you for free and open access by DigitalCommons@UMaine. It has been accepted for inclusion in Honors College by an authorized administrator of DigitalCommons@UMaine. For more information, please contact um.library.technical.services@maine.edu.

VHF NEAR FIELD ANTENNA DESIGN FOR WIRELESS SENSING APPLICATIONS IN HARSH ENVIRONMENTS

by

Nicholas F. Aiken

A Thesis Submitted in Partial Fulfillment
of the Requirements for a Degree with Honors
(Electrical Engineering)

The Honors College

University of Maine

May 2019

Advisory Committee:

Mauricio Pereira da Cunha, Professor of Electrical Engineering, Advisor
Edith Elwood, Adjunct Assistant Professor of Sociology, Preceptor in the Honors College
Nuri Emanetoglu, Associate Professor of Electrical Engineering
Sarah Harlan-Haughey, Associate Professor of English
Robert Lad, Professor of Physics

© 2019 Nicholas F. Aiken

All Rights Reserved

ABSTRACT

High temperature sensors that can operate up to 1000 °C or beyond are in high demand for defense, aerospace, energy exploration and power industries. Wired sensors for high temperature operation has low reliability and high installation costs. Wireless communication provides functionality for operation in harsh environments. Wireless communication in harsh environments must be battery-free because semiconductor electronics is unable to operate beyond a few hundred degrees Celsius and there is a very limited number of alternatives for energy storage at extreme temperatures. The University of Maine's Microwave Acoustics Laboratory (MAL) group has developed Surface Acoustic Wave (SAW) devices which can communicate wirelessly in high temperature environments without power supplies (i.e., passive). Field coupling wireless interrogation technology is attractive for harsh environment applications because of reduced antenna size. The present state-of-the-art allows for operation up to tens of millimeters, where attenuation of the two-way communication can reach 50 to 70 dB. The research presented investigates the possibility for improvement of power transfer to the sensor and from the sensor back to the interrogation unit. The improvement in performance was sought through the refinement in impedance matching for both the interrogating antenna and the sensing antenna and SAW sensor. SAW sensors operate between 180 MHz to 340 MHz. The work entailed radio frequency (RF) circuitry simulation using Advanced Design Systems (ADS) and High Frequency Structure Simulator (HFSS) commercial software packages, fabrication, test, and adjustment. The obtained results for interrogating and sensor antennas and matching circuits presents positive impacts high-temperature harsh-environment wireless SAW sensor communication links.

ACKNOWLEDGEMENTS

I would like to extend gracious thanks to my advisor, Dr. Mauricio Pereira da Cunha, for his continued help and guidance throughout the duration of my research experience. I would also like to thank my committee members for their advice and guidance throughout the writing of this thesis.

TABLE OF CONTENTS

LIST OF FIGURES

CHAPTER I

INTRODUCTION

This thesis describes the optimization of the wireless communication link between an interrogating antenna and a sensing antenna connected to a surface acoustic wave (SAW) sensor under a field coupling interrogation scheme. Industry needs sensors that operate in harsh environments. SAW sensors can operate in harsh environments, meaning temperatures which approach 1000°C (temperature of lava). Industries such as coal and natural gas power plants, smelting and waste management facilities, as well as aerospace, all have processes or applications in high temperature and harsh environments. In these harsh environments, sensors provide critical feedback regarding system efficiency, stability, integrity or failure. Using sensors to initiate preventative actions before system failure reduces costs and is known as condition-based maintenance or health monitoring. Use of sensors also increases safety of operations, process efficiency and overall impact on the environment with less pollutants. Sensing measurands in harsh environments can be temperature, gas concentration, pressure, corrosion and strain, depending upon the application. Wireless operation expands the potential application of harsh environment sensors due to the removal of wired connections and feasibility of sensor placement. By increasing transmission distance, wireless sensors applications can be expanded to more locations and increase signal to noise ratio. Sensors operating under such harsh conditions must also be capable of operating battery-free, due to the limited availability of batteries or energy storage capability in harsh environments.

The technology used for wireless sensing in harsh environments is the SAW sensor. SAW sensors have been proven to perform in harsh environments, sending and receiving power when operating at high temperature in a wireless communication link. Wireless communication using a SAW sensor is possible without the usage of a battery. Radiating antennas can be used for wireless communication but are large. Field coupling antennas are used for wireless applications where antennas must be small. For field coupling antennas you can have electric or magnetic field coupling. Wireless sensing systems using electric field coupling produce a measurable signal at a maximum interrogation distance of 5mm, while magnetic field coupling provided measurable interrogation distance up to about 12 mm. While wireless communication was achieved, it is desirable to extend the communication distance to expand the applicability of the SAW sensor and to increase the signal to noise ratio.

In this thesis, the work focuses upon magnetic field coupling for wireless communication between the interrogating and sensing antenna. The focus of the work is to maximize interrogating distance with electrically small antennas. The research conducted circuit analysis and radio frequency (RF) simulation software to investigate feasible antenna and circuit design changes to improve the wireless communication system.

Surface Acoustic Wave Devices

Surface acoustic wave (SAW) devices are electrical devices that operate using piezoelectric properties. Piezoelectric effect can be described as the mechanical deformation that occurs in the material (substrate) when an electric field is applied. This effect is consistently symmetrical in the sense that a deformation in such material also

generates an electric field. If the produced electrical signal is periodic with a sinusoidal function, then the deformation is also periodic and generates waves which propagate in the substrate, either at the surface (surface waves) or towards the bulk of the material (bulk waves). The surface acoustic wave is guided on the surface. If no shear particle component parallel to the direction if propagation is present, the wave is labeled as a Rayleigh wave, and the material particle has an elliptical motion in the sagittal plane as depicted in Figure 1.

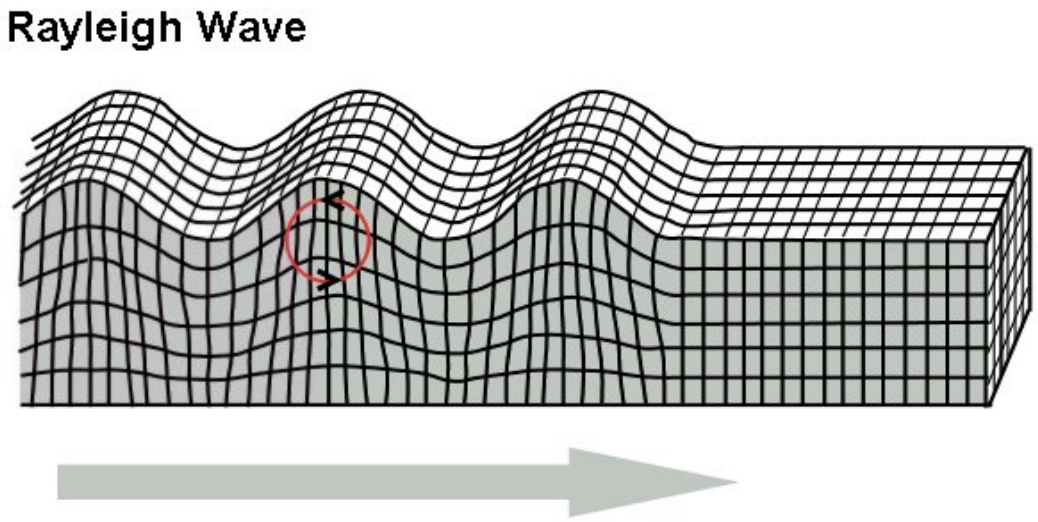

Figure 1: Depiction of Rayleigh wave. [1]

The most common piezoelectric materials for SAW devices are quartz, lithium niobite (LNB) and lithium tantalite (LtO). Each of these materials and their properties depend upon their crystalline structure and constituent components which affect their elastic, dielectric and piezoelectric constants and thus the coupling coefficient.

Euler characteristics describe the planes and orientations of piezoelectric materials. Euler angles are used to identify planes, propagation and orientations of the crystal lattice of the

piezoelectric. Upon application of a stress the material deformation generates an electric field. The field is dependent upon the crystalline structure and orientation.

Different piezoelectric materials operate well at different temperatures. Materials such as quartz, LNB, and LtO operate well at temperatures between 200 and 300° C, other materials like langasite or aluminum nitride can be operated at higher temperatures. The SAW sensor material used in this research is langasite (LGS). langasite can operate above 1000 ℃.

There are several different types of SAW devices which are used for different applications. SAW sensors can be used for applications such as cellular phone filters, frequency control devices, and sensors. The sensing capability is dependent on the piezoelectric material, its orientation, and the device design. A 2-port delay line is presented in Figure 2.

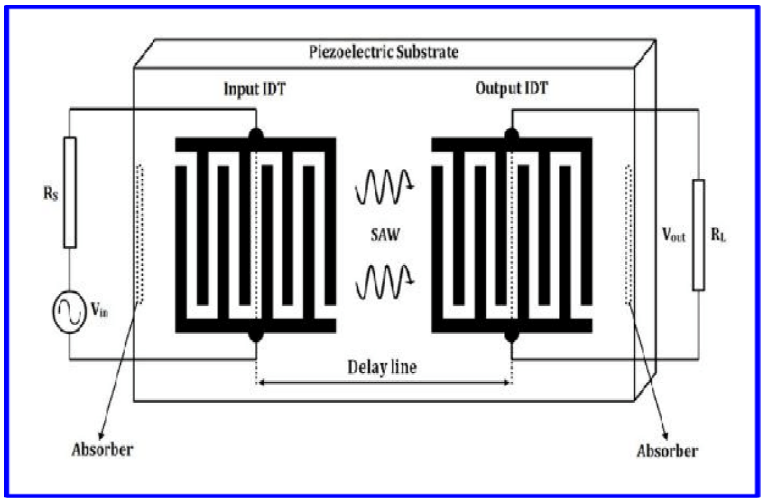

Figure 2: 2 Port SAW delay line. [2]

For the delay line in Figure 2 there is an input IDT which is connected to an AC source where the SAW is excited. Electrodes are printed using photolithography at the surface of

the piezoelectric material and under periodic electrical excitation, mechanical disturbances are produced and vice-versa. The SAW travels across the substrate before output via the output IDT which delivers the electrical signal produced to a load. Delay lines have the feature of producing a delay between the input and output due to the phase velocity 10^5 orders lower with respect to an electromagnetic wave.

The saw design used in this work is a single port resonator, meaning that the sensor input, and output share the same port. A diagram of a single port SAW resonator is presented in Figure 3.

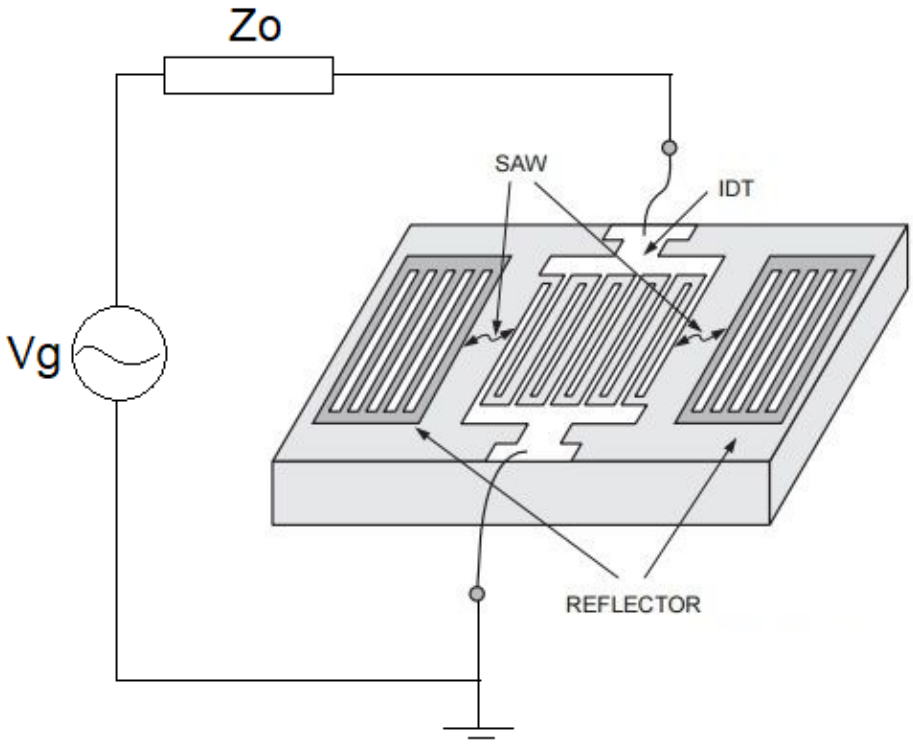

Figure 3: SAW Resonator. [1]

As presented in Figure 3, the SAW resonator employs at least one inter-digitated transducer (IDT) and reflectors on both sides of the IDT. The produced SAW energy is

confined in the distributed cavity between the reflectors. This characterizes resonator operation. In the case shown in Figure 3, the steady state wave produced is measured through the same port used to excite the device. The sensors used in this work operate in a frequency range between 180-340 MHz, on langasite. The size of SAW devices operating between 180-340 MHz on langasite are on the order of a few millimeters with feature dimensions on the order of micrometers. An image of the SAW sensor used in the described research is presented in Figure 4.

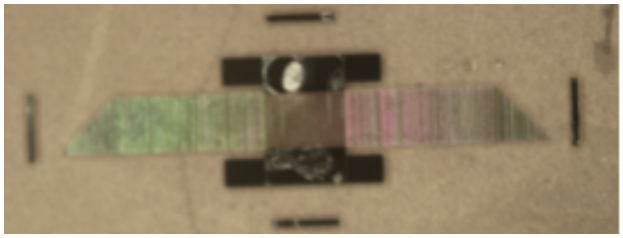

Figure 4: SAW sensor used during performed research.

As indicated in Figure 4, the SAW sensor's reflectors are depicted by the rainbow-colored gradient, while the conductive pads connecting to the IDT structures are in black. SAW devices are fabricated using a thin film fabrication process. All electrodes used for the SAW device used in this work are fabricated using platinum/alumina composite electrode, and bond pads (indicated in black) are pure platinum. A capping later is placed on the top, made of a protective Al_2O_3 thin film. The electrodes were spaced by 3.8 μm, leading to device operation at roughly 180 MHz. Device operation around 300 MHz is achieved by electrodes spaced at roughly 2 μm.

Relevant Background For The Performed Work

Working with devices operating between 180-340 MHz requires an understanding microwave engineering. At high frequencies, voltage and current measurement are not

feasible since the wavelength is comparable to the connecting lines. Transmitted and reflected power is measured instead. Power is given by

$$P = Re\{VI^*\} \tag{1}$$

And impedance is

$$Z_s = \frac{V}{I} = R_s \pm jX_s \tag{2}$$

which can be represented as the summation of series resistance and series reactance. Measurement of reflected power can be quantified with respect to the voltage standing wave ratio (VSWR). VSWR is the ratio of the maximum voltage and the minimum voltage on a medium where both forward and backward traveling waves are present. A standing wave is the result of the forward traveling wave and backward traveling wave produced due to reflection at the load. A visual representation of a standing wave is presented in Figure 5.

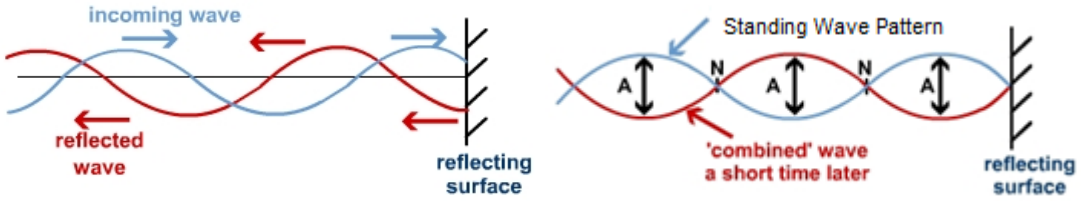

(a) (b)

Figure 5: (a) Independent forward and backward traveling waves, (b) standing wave formed. [5]

When the reflection coefficient of a system under test is -1, this signifies complete reflection due to a short circuit load. When the reflection coefficient is 1, all the signal is reflected as well, and in this situation is equivalent to an open circuit. When the load is equal to the conjugate of the input impedance or to the characteristic impedance Z_o, then the reflection coefficient is zero. In such case it is said that the load is matched to the input or to the line. Magnitude of the reflection coefficient can be calculated by

$$|\Gamma| = \frac{|V^-|}{|V^+|} \tag{3}$$

and

$$SWR = \frac{1+|\Gamma|}{1-|\Gamma|}. \tag{4}$$

The reflection coefficient (magnitude and phase) is calculated by

$$\Gamma = \frac{Z_L - Z_o}{Z_L + Z_o} \tag{5}$$

where Z_o is the characteristic impedance of the line. The reflection coefficient could be measured using a vector network analyzer (VNA) which uses the concept of a fixed Z_o. Using (5), the reflection coefficient and Z_o, the load impedance can be calculated. Loads under measurement using a VNA are often connected using a coaxial line. To compensate for coaxial lines connecting between the VNA and the load, the line is calibrated to the port. In some cases, the line cannot be calibrated to the port and the reflection coefficient must be transformed to compensate for the length of line. The reflection coefficient Γ_{in} where

$$\Gamma_{in} = |\Gamma_L| e^{-2\alpha(d+\Delta l)} \angle(\phi_L - 2\beta d - 2\beta \Delta l) \tag{6}$$

represents the reflection coefficient which compensates for a length of line between the generator and the load. Here alpha is the attenuation constant of the line in nepers per meter, d is the original length of the line, and Δl is the change in the length of the line. The variable $\boldsymbol{\phi_L}$ represents the angle of the reflection coefficient of the load and β is represented in (7) as

$$\beta = \frac{2\pi}{\lambda}. \tag{7}$$

A one port SAW resonator operating at resonance of the motional arm can be modeled by a resistor in parallel with a static capacitance. Resonance occurs at the frequency when

the SAW's motional capacitance and motional inductance are at resonance. The static capacitance comes from the interdigitated nature of the interdigitated transducer. A figure of the circuit model for a SAW resonator is presented in Figure 6.

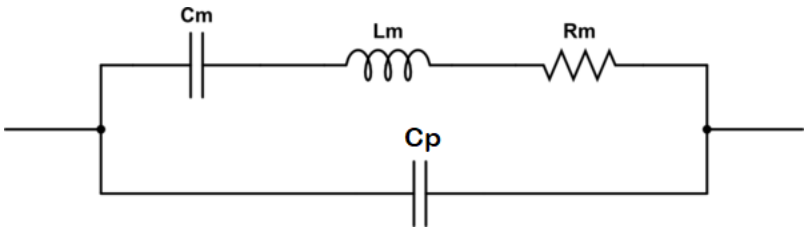

Figure 6: SAW resonator circuit model.

The SAW is admittance Y can be expressed as

$$Y = \frac{1}{Z_p} = G_P + jB_P \tag{8}$$

where

$$G_P = \frac{1}{Rm} \tag{9}$$

and

$$B_P = \omega C_p \tag{10}$$

and

$$Z_p = Z_s. \tag{11}$$

The SAW is characterized in terms of admittance because of its parallel device model, where the resonance frequency occurs at the frequency where the real component G_P of the SAW is a maximum. A plot of the admittance of a SAW device is presented in Figure 7.

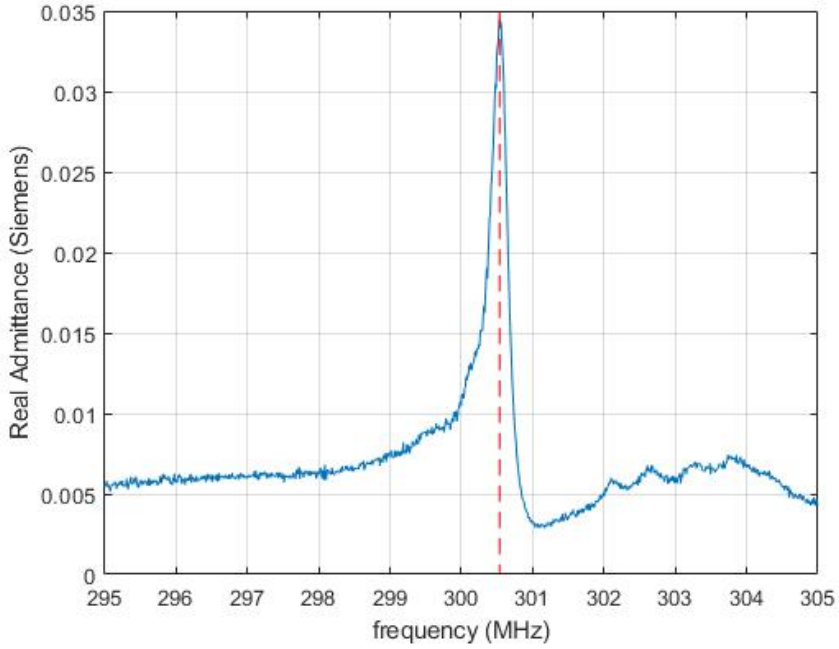

(a)

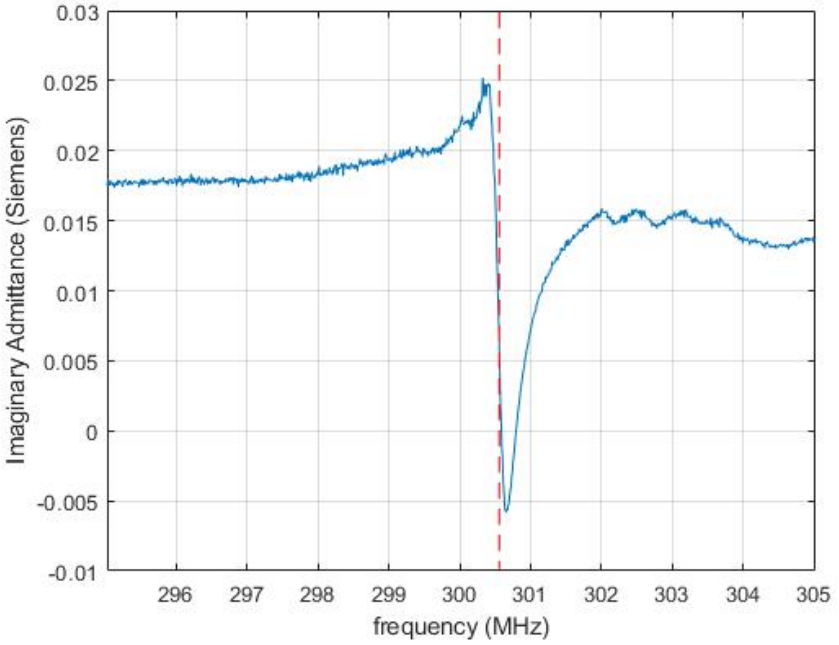

(b)

Figure 7: (a) Real part of SAW admittance, (b) imaginary part of SAW admittance

The resonance frequency is used to calculate the equivalent series impedance of the SAW at resonance. The equivalent series impedance can be transformed into parallel equivalent impedance model of the SAW impedance at resonance. The parallel equivalent impedance is calculated where

$$Z_p = \frac{jR_pX_p}{R_p+jX_p} = \frac{R_pX_p{}^2}{R_p{}^2+X_p{}^2} + j\frac{X_pR_p{}^2}{R_p{}^2+X_p{}^2}. \quad (12)$$

and

$$R_s = \frac{R_pX_p{}^2}{R_p{}^2+X_p{}^2} \quad (13a)$$

and

$$X_s = \frac{X_pR_p{}^2}{R_p{}^2+X_p{}^2}. \quad (13b)$$

Using (13a) and (13b) R_p and X_p can be calculated as,

$$R_p = R_s\left(1+\left(\frac{X_s}{R_s}\right)^2\right) \quad (14a)$$

and

$$X_p = X_s\left(1+\frac{1}{\left(\frac{X_s}{R_s}\right)^2}\right). \quad (14b)$$

The parallel reactance is then converted into capacitance where

$$C_p = \frac{1}{2\pi f X_p}. \quad (15)$$

With methods for characterizing impedance of microwave circuits considered, impedance matching, and tuning can be described. Impedance matching is a method used to transform impedance between the generator and the load to maximize power transfer. Figure 8 provides the circuit model for VNA and a load.

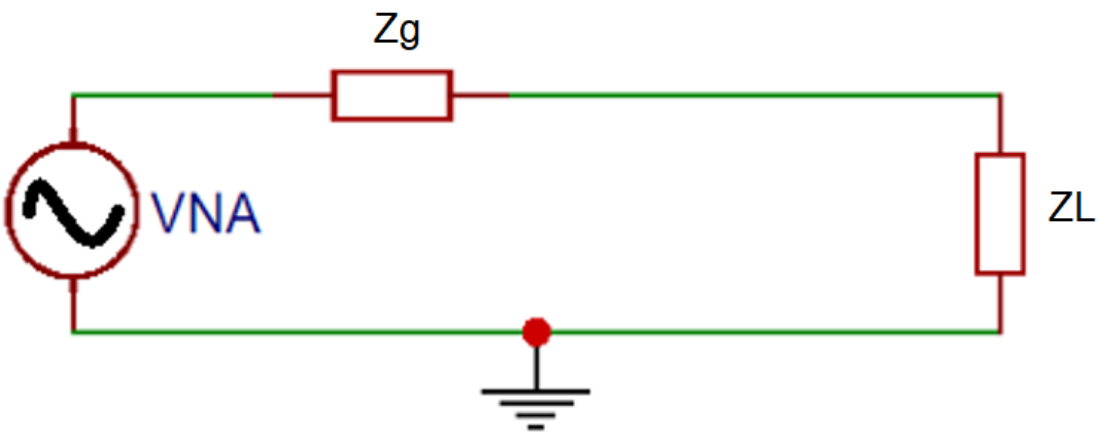

Figure 8: Simplified model for SAW measurement using VNA and coaxial line connection.

Maximum power transfer occurs when the load impedance is equal to the conjugate of the generator impedance, where

$$Z_L = Z_g^*. \tag{16}$$

For transmission line applications, the generator impedance is equal to the characteristic impedance of the line. In practice, the characteristic impedance of most cables are 50 Ω.

For the described research, there are two cases of impedance matching. The first case is when interrogating antenna is connected to a VNA and the second case is the connection of the sensing antenna and SAW sensor. For the first case, the impedance of the generator is equal to the characteristic impedance of the VNA and coaxial line (50 Ω). For case 2, the generator impedance changes depending upon how the source is modeled in the circuit. When the sensing antenna acts as the source, the impedance of the sensing antenna is represented as the generator impedance. When the SAW is the source, the SAW impedance is represented as the generator impedance. For both instances for case 2, the generator impedance is not equal to a characteristic impedance of 50 Ω. Ballpark

values for SAW impedance is 25-j10 Ω. Sensing antenna impedance roughly 10+j250 Ω while interrogating antenna impedance varies from 20+j300 Ω to 40+j500 Ω.

Different combinations of lumped element components can be used to adjust the equivalent impedance looking into the tuning network from the source. Use of components to match the source to the load requires at least two components unless the real part of the load is equal to the real part of the generator's impedance. Two impedance matching networks which will be considered in this thesis. These networks are the T circuit and an L circuit in Figure 9.

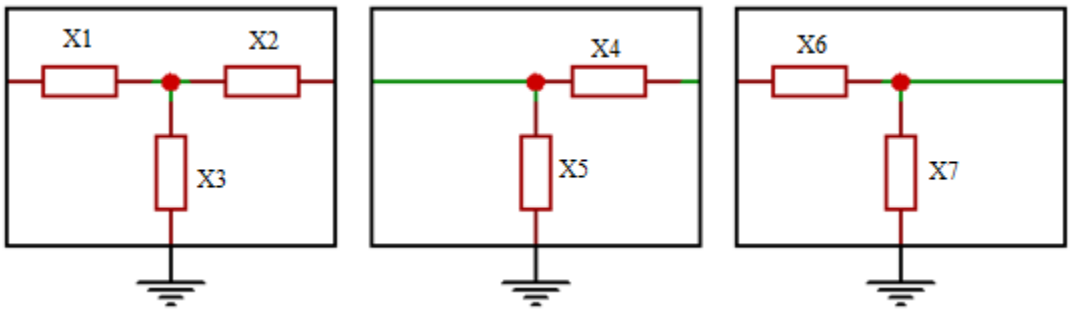

(a) (b) (c)

Figure 9: (a) T circuit (b) L circuit configuration 1, (c) L circuit configuration 2.

Each of the different configurations in Figure 9 provide different advantages. While matching can always be achieved with two components, the T circuit provides an additional degree of freedom due because of the third matching component. The three-component network such as the T network can provide flexibility in selection component values used for matching and allows for control of phase and amplitude in feedback circuitry. There is also another three-component network called the π network, which was

not considered but provides similar functionality as the T circuit. For the L circuit in Figure 9 (b) and (c), use of inductance or capacitance, or a combination of the two can be used to match the load. Depending on the generator impedance and load impedance component values and types (inductance or capacitance) can lead to a matched condition. Matching networks are implemented in the equivalent circuit model for the general case presented in Figure 10.

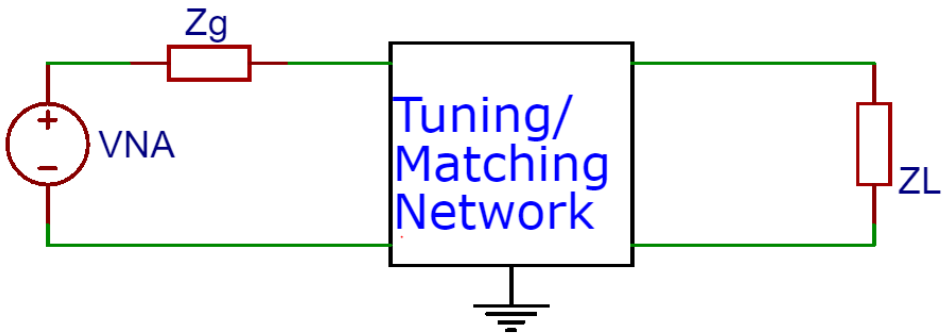

Figure 10: General circuit model including tuning/matching network.

A single element can compensate for the reactive match between generator impedance and load impedance. The impedance a single element is used in series as in Figure 11.

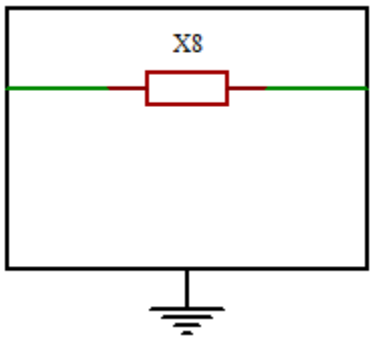

Figure 11: Tuning element used in series between generator and the load.

For the case of impedance matching, a matching network achieves the condition in (15). Use of a single tuning element in series only enables when the sensing antenna is the source (and has a reactance of 250 Ω). When the SAW sensor is the source in case 2, a

single tuning element in series will tune the equivalent reactance of the load to 10 Ω (when the SAW reactance is -10 Ω).

The final introductory topic pertains to wireless communication and the characterization of far field, near field and field coupling wireless communication techniques. Antennas can operate in three different regions, the radiating far field, Fresnel region, and the near field. Each of these regions are defined with respect to wavelength, antenna dimension, and radiation distance is presented in Figure 12.

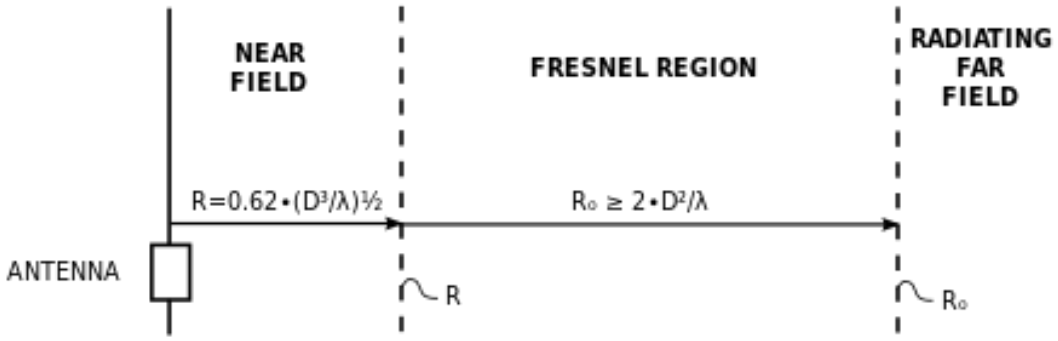

Figure 12: Fields of antenna operation [4].

As indicated in Figure 12, the maximum antenna dimension is D, wavelength is λ and R is the radiation distance. A common example of antennas operating in the far field are cell phones. Cell phones operate with frequencies in the GHz range, so antenna dimensions can be physically small. Cellular communication systems also requires cell phones access an external power source like a battery and cannot be powered solely by a wireless signal. Other examples of wireless communication systems operating in the far-field are

satellites and radio towers. Antennas operating in the far field enables increased power transfer with respect to distance, where power drops off with approximately $\frac{1}{R^2}$.

For this research, SAW devices fabricated on LGS operate between 180-340 MHz, which requires antenna dimensions of roughly 1 foot to operate in the far field region. Antenna dimensions of this size are not desirable for small antenna applications where dimensions range between 10mm to 20 mm. For electrically small antennas in the described research, near field operation results in power drops off with $\frac{1}{R^6}$. The proposed research also requires SAW sensors are powered by the wireless signal. Two different near field antenna design approaches can be used to communicate wirelessly for the proposed application. The first method for coupling energy in the near field is electric field coupling with system diagram presented in Figure 13.

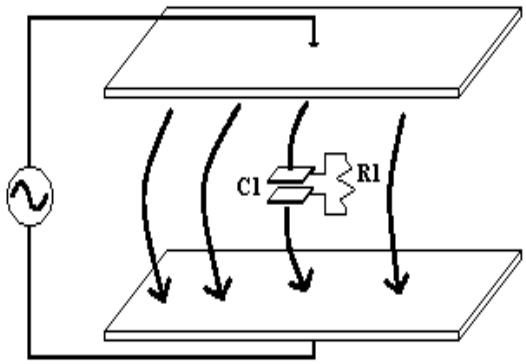

Figure 13: Electric field coupling near field wireless link.

In the case of Figure 13, the electric field is used to transmit and receive signal. The interrogating antenna is a capacitor, such as the larger plates connected to the AC source in Figure 13. The inner sensing antenna is another capacitor connected to a load R1. The

inner sensing antenna attached to R1 couples to the electric field from the transmitting antenna. Figure 14 shows the magnetic field coupling between two coils.

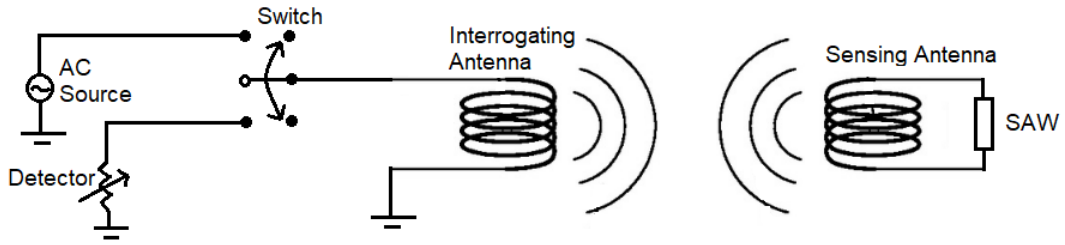

Figure 14: Magnetic field coupling near field wireless link.

The first antenna is connected to an AC source which generates magnetic field which is then coupled to the second antenna, with the model enabling the SAW to act as the source and as the load.

This thesis focuses upon near field magnetic field coupling for wireless sensor interrogation. Antenna design with respect to magnetic field requires an understanding of the relationship between current, inductance and magnetic field. Amperes law states that there is a magnetic field produced around an electric current is proportional to the source current. The magnetic flux (Φ), which is the total magnetic field produced by the inductor is directly proportional to the inductance and the current as presented in (17) [3] where

$$\Phi(i) = L * i \ . \tag{17}$$

The relationship between antenna design parameters and inductance is presented in (18).

$$L = \frac{\mu N^2 A}{l} \ . \tag{18}$$

In (18) μ is the magnetic permeability, A is the area of the inductor, l is the length of the inductor and N is the number of loops. This equation is derived with respect to a solenoid

structure but represents the relationships between the four parameters which can be adjusted by the designer to produce the best magnetic field coupling possible with respect to size, materials and the operation frequency constraints. There is a tradeoff between the inductance and antenna dimensions with respect to the operation frequency. If the inductance becomes too large the antenna can become self-resonant at the operation frequency which is undesirable.

Previous State-Of-The-Art

The primary goal of the present research is to maximize operational distance between the interrogating antenna and sensing antennas. Figure 15 depicts that the interrogating antenna (IA) connected to a VNA, which sources an AC signal to the antenna, and measures the signal transmitted back by the SAW. The signal that is transmitted from the interrogating antenna is coupled to the sensing antenna (SA) which is connected to the SAW device. The SAW device receives the signal and resonates. The resonance of the SAW affected by the sensor measured produces a source signal on the return path, which is then sent back to the sensing antenna. The sensing antenna then transmits the resonance signal from the SAW back to the interrogating antenna, where the signal is received and measured by the VNA. This process is called a two-way wireless communication link.

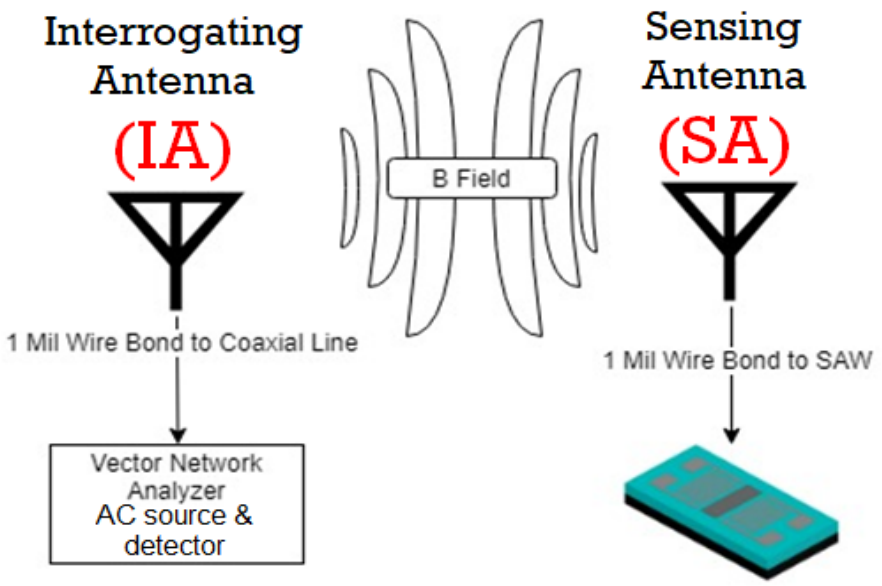

Figure 15: Complete magnetic field wireless sensor link.

Before the technical discussion of the research goals of the project can be presented, previous research and the previous state-of-the-art wireless link must be defined. Both magnetic and electric field coupling techniques have been tested in previous work conducted by the Maine Acoustics Laboratory (MAL) at the University of Maine. Maximum distances where a measurable signal was achieved were approximately 12 mm with magnetic field coupling techniques. The antennas used for this design were a planar loop antenna design, fabricated on Alumina with gold paste. Photographs of the original magnetic field coupling wireless system are presented in Figure 16 [6]

(a) (b)

Figure 16: Magnetic field (a) SAW sensor antenna, (b) interrogating antenna [6].

Capacitive field coupling techniques were also investigated. The results from previous research regarding electric field coupling indicated a maximum transmission distance of approximately 5 mm. A figure of the SAW sensor antenna and interrogating antenna are presented in Figure 17.

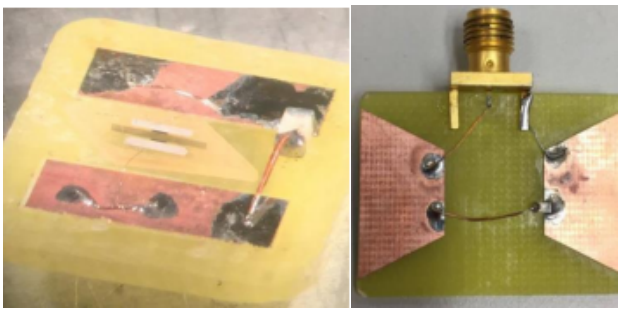

(a) (b)

Figure 17: Electric field (a) SAW sensor antenna, (b) interrogating antenna [6].

The approximately 12 mm transmission distance was achieved for magnetic field coupling is better than approximately 5 mm for electric coupling, which indicates magnetic field coupling is more promising for wireless communication for the system. Previous research indicated that that tuning of the interrogating antenna could improve the signal strength of the wireless link, but the magnitude of improvement has not been quantified. Previous research also indicated that tuning was conducted by considering the equivalent impedance of the interrogating antenna a “short circuit”. These suggestions were investigated to provide direction for the research conducted to maximize operational distance between the interrogating antenna and the sensing antenna [6].

Objective

The described research approach targets better understanding of the limitations of the wireless link presented in Figure 15. The goal of the research is to maximize transmission

distance between the sensing and interrogating antenna, while keeping a fixed footprint (size) for the antennas. The research begins with the interrogating antenna and characterization of the previous state of the art system. Characterization includes impedance measurement and comparison to simulated impedance results for both the sensing and interrogating antenna in the HFSS and ADS environment. Comparison between measured impedance of the antennas and simulated impedance of the antennas provides a baseline by which the system can be improved.

Increased transmission distance can be achieved by performing an impedance transformation between the VNA and the interrogating antenna. Under the matched condition the best case occurs where maximum current flows through the interrogating antenna and maximum power is delivered to the VNA when a signal is received from the sensing antenna. New interrogating antenna designs as well as interrogating antenna matching or tuning to the VNA will be considered to maximize the magnetic field produced by the interrogating antenna, maximize power deliver to the VNA and maximize current flow through the interrogating antenna.

Increased transmission distance also requires the impedance transformation between the SAW and the sensing antenna. The optimum operation condition between the SAW and the sensing antenna occurs when maximum current flows through the sensing antenna and maximum power is delivered to the SAW when a signal is received form the sensing antenna by the interrogating antenna. Maximum current flow produces the largest magnetic field when the sensing antenna is excited by the SAW or when magnetic field is

coupled from the interrogating antenna. Methods considered to achieve these conditions will be sensing antenna design optimization, and sensing antenna matching or tuning to the SAW component.

CHAPTER II

METHODS

Interrogating Antenna Design

There were two approaches by which the interrogating antenna was optimized. The first approach was to maximize the inductance of the interrogating antenna. The constraint for maximizing the inductance of the interrogating antenna are that the footprint must remain the same as the previous state of the art interrogating antenna, and the designed antenna cannot be self-resonant within 180-340 MHz frequency range.

The second design approach considered was matching or tuning of the interrogating antenna. By matching to a characteristic impedance of 50 Ω or tuning the interrogating antenna, the current flowing through the antenna and the power received back by the VNA can be optimized. The combination of these two design approaches are used to optimize the performance of the interrogating antenna and increase the transmission distance between the interrogating antenna and the sensing antenna of the wireless link.

To establish the baseline operation, the previous state-of-the-art was characterized. This characterization began with comparing the impedance simulation of interrogating antenna using ANSYS High Frequency Electromagnetic Field Simulation (HFSS) and the measured impedance. First the 3D design of the original interrogating antenna was drawn and simulated. A figure of the simulated antenna is presented in Figure 18.

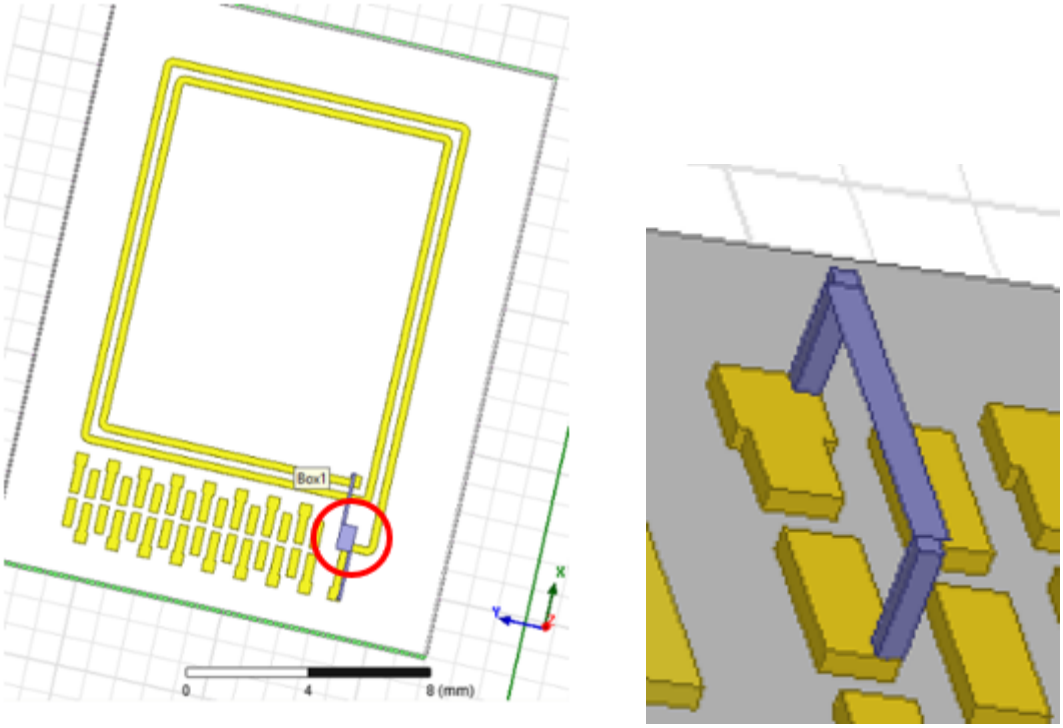

(a) (b)

Figure 18: (a) Simulated original interrogating antenna (b) close-up of a 2D lumped port in HFSS.

The simulated result plotted the reflection coefficient with respect to a port declared in the 3D environment. The small grey rectangle which is highlighted with a red circle presented in Figure 18 (a) is a 2D plane used to represent a lumped port. Figure 18 (b) is an image where the clear differentiation between the 2D lumped port and 3D solids used for 1 mil platinum bonds is depicted. The 2D plane must contact the solids and represents the excitation point where the reflection coefficient is evaluated in the HFSS environment. HFSS plots the reflection coefficient using a Smith chart. A Smith chart is a polar plot of the magnitude and phase of the reflection coefficient, were Γ is translated into normalized impedance according to the conformal mapping where

$$\bar{Z} = \frac{Z}{Z_o} = \frac{1+\Gamma}{1-\Gamma}. \tag{19}$$

The characteristic impedance used was declared in HFSS simulations as 50-ohms.

Simulation of the antenna in Figure 18 was compared to measurement and provided a baseline of the previous-state-of-the-art system. The previous interrogating antenna was measured and set up is shown in Figure 19.

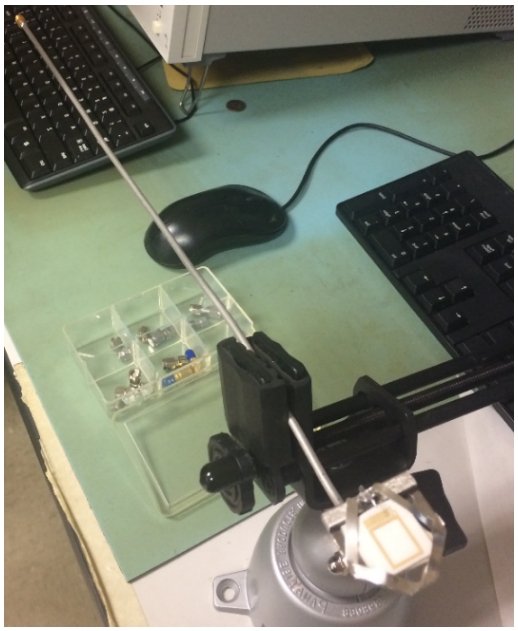

Figure 19: Previous state of the art interrogating antenna.

The original interrogating antenna was printed on an alumina substrate and was printed using a silk-screen mesh and gold paste. The antenna substrate and the conductor were chosen to be able to withstand temperatures up to 1000 °C. The previous state-of-the-art interrogating antenna was connected to a VNA for measurement using high temperature coaxial cable made of Inconel. The interrogating antenna was bonded to the coaxial line by 1 mil platinum wire. 1 mil wire was used because 4 mil wire was too large and would strip off gold conductor when bond wires were removed. Small wire also decreases resistance and parasitic inductance. Platinum wire is used because it is capable of withstanding high temperatures. The measurement of the previous state-of-the-art interrogating antenna with comparison to the HFSS simulations is presented in Figure 20.

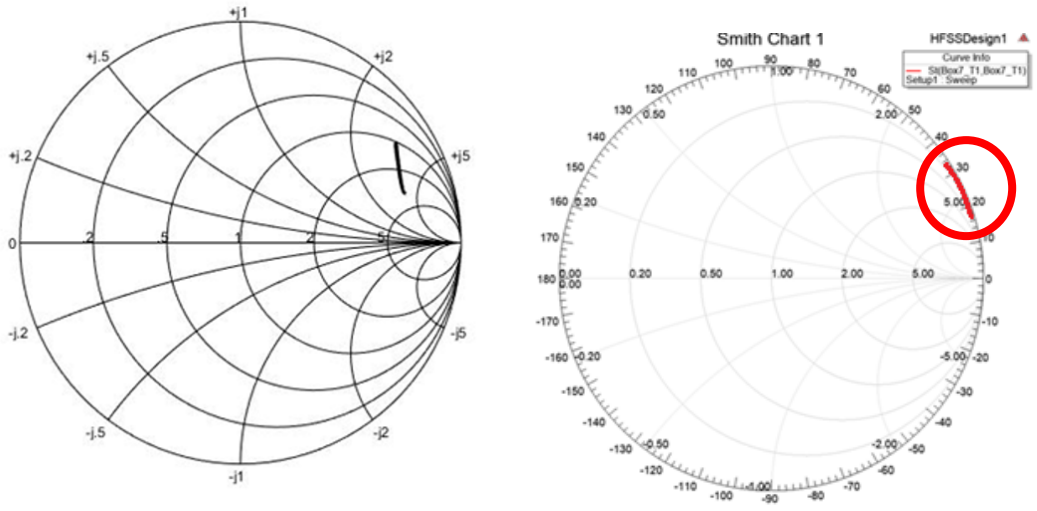

(a) (b)

Figure 20: (a) Measured results, (b) simulated results.

The measured results indicated the presence of a significantly higher resistance with respect to the simulated model using HFSS. This is verified by the reflection coefficients being closer to the inside of the Smith chart in Figure 20 (a) compared to (b). If the attenuation constant was high, the reflection coefficient would approach the center of the Smith chart which indicates loss or high resistance. An Inconel line of 10 cm length was then short circuited using a 1 mil bond wire and the reflection coefficient was measured for a 10 MHz span. The electrical delay required to move the reflection coefficient to the short circuit location was used to determine the attenuation constant using (6). The electrical delay gives a time in seconds which was solved for the exact length of the line, l, which is presented in (20).

$$Delay(s) = \frac{l*\sqrt{\varepsilon_r}}{c} \tag{20}$$

The reflection coefficient at the load is $1\angle 180^{o}$, the attenuation constant was calculated by solving for alpha (α).

The attenuation per unit length for Inconel coaxial lines were 4.3 dB/m at 330 MHz, with attenuation per unit length 0.8 dB/m at 330 MHz for typical lower temperature coaxial cables. Inconel coaxial lines cannot be used for impedance measurement due to their high attenuation constant. It was determined that the significant difference between simulated and measured results was due to loss per unit length of the Inconel line.

Another factor that was considered to improve the HFSS simulations was to use the conductivity of the gold paste used to fabricate the interrogating antenna. Measurement of the previous state-of-the-art interrogating antenna indicated series resistance at 330 MHz on the order of 25 ohms. Previous simulations used pure gold, with conductivity of 4.098E7 siemens/meter. The gold paste used for fabrication was more porous than pure gold and had lower conductivity, with a conductivity of 1.8E7 siemens/meter. This was calculated using the sheet resistance provided by Heraeus for C5729 Pb and Cd free gold conductor paste. The final comparison between the S_{11} of the previous state of the art interrogating antenna S_{11} and simulated S_{11} is presented in Figure 21.

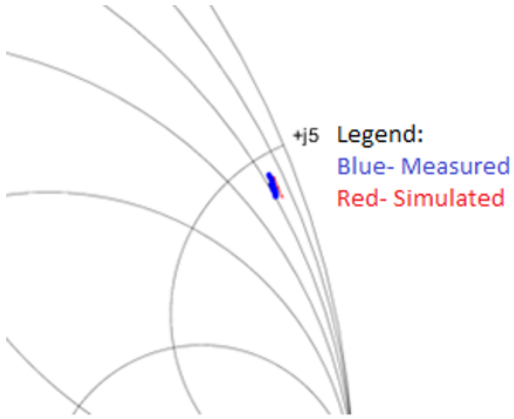

Figure 21: Comparison of S_{11} results for HFSS simulated and measured results.

The results from Figure 21 were within less than 10% of each other. The results from Figure 21 indicate that series resistance increases because of the lower conductivity of gold paste compared to pure gold.

For the interrogating antenna loop design there are three main design constraints: antenna size, number of loops, and spacing between loops. A depiction of the two parameters that were varied to optimize the antenna design is presented in Figure 22.

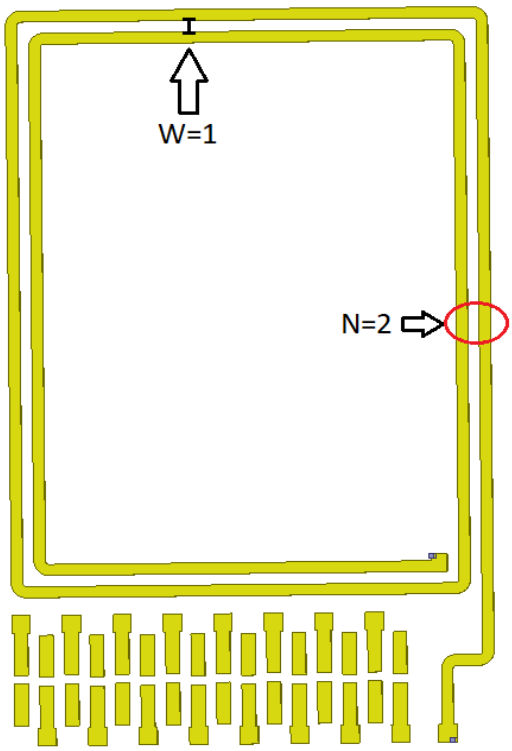

Figure 22: Interrogating antenna with design constraints labeled.

The first parameter is the number of loops, represented by N, and the second parameter in the design is spacing between loops represented by W. The spacing is measured with respect to line widths, where W=1 represents spacing of one-line width. One may think to fit the maximum number of loops possible into the fixed 15x20 mm footprint would

result in maximum inductance. The problem with this design method would be the issue of self-resonance. Each length of line used for a loop represents an inductance, while each loop in parallel has an associated parasitic capacitance. The closer the loops, the larger the parasitic parallel capacitance becomes. The more loops there are, the larger the equivalent parallel capacitance across all loops of the antenna. At the frequency given by

$$f_p = \frac{1}{2*\pi*\sqrt{LC_p}} \tag{21}$$

the structure resonates as an open circuit, no longer operating as an inductor. The circuit model for a self-resonant loop antenna is presented in Figure 23.

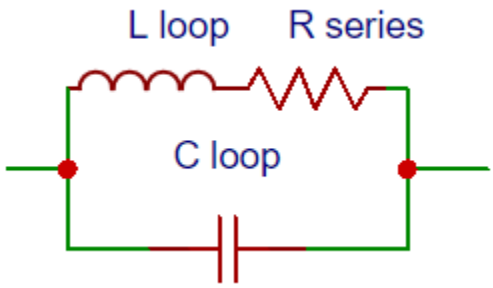

Figure 23: Model for parallel self-resonance of the inductive antenna.

To determine the trade-off between the number of loops and spacing between loops, the designs were simulated, and the resonant frequency was determined for each new design. The method by which designs were considered began by starting with a given number of loops, and then increasing the spacing between loops. This process was repeated until the maximum number of loops and/or spacing between loops was achieved given the 15x20 mm footprint. Feasible designs were chosen if reactance at 300 MHz was 10% or less than the reactance at the resonating frequency. A plot of the width variations for the four loop interrogating antenna simulations is presented in Figure 24.

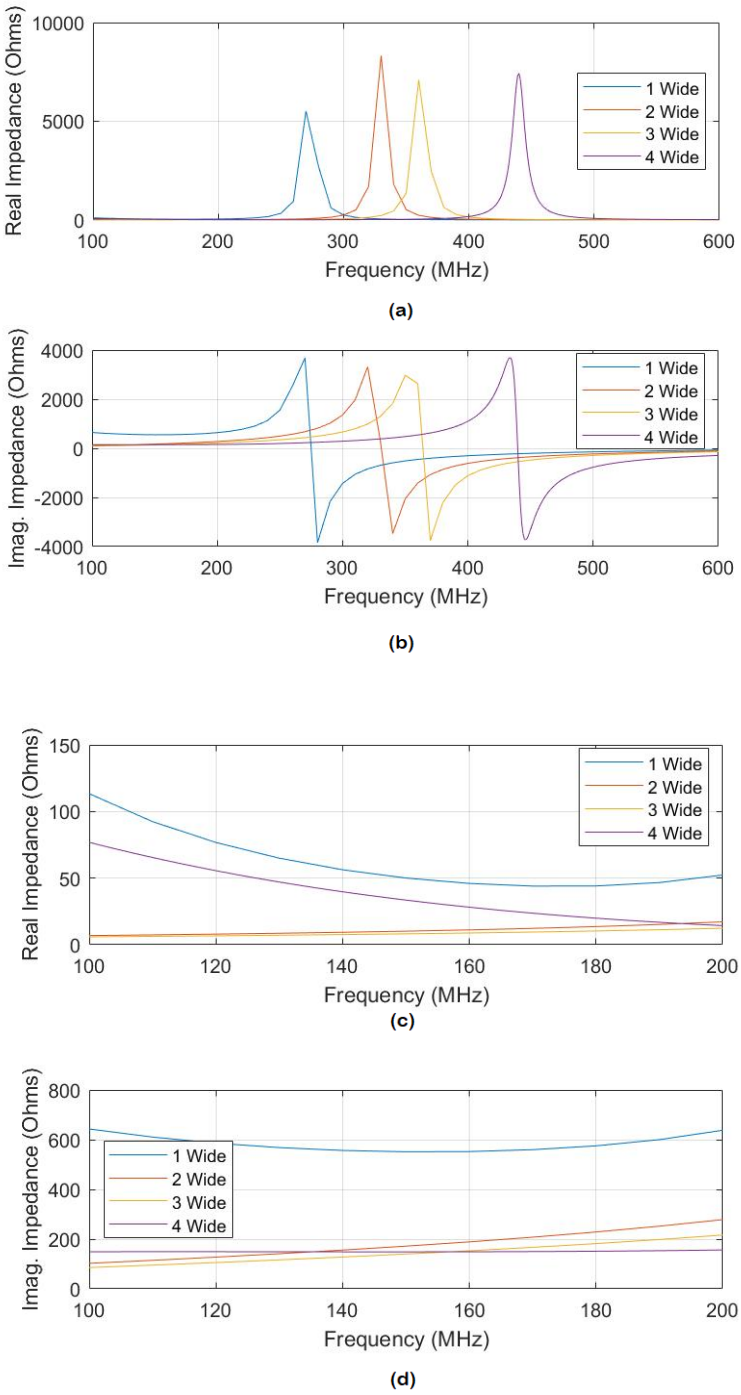

Figure 24: Plot of impedance for four loop interrogating antenna as loop width varies, (a) real impedance, (b) imaginary impedance near resonance, (c) real impedance (d) imaginary impedance before resonance.

All simulated results for all variations of the numbers of loops and spacing between loops for interrogating antennas are available in Appendix A. After simulation of designs, it

was identified that four structures were feasible for implementation and later tuning. The chosen antenna designs exhibited reactance which was 10% or less with respect to the reactance at their resonance frequency. These designs are presented in Figure 25.

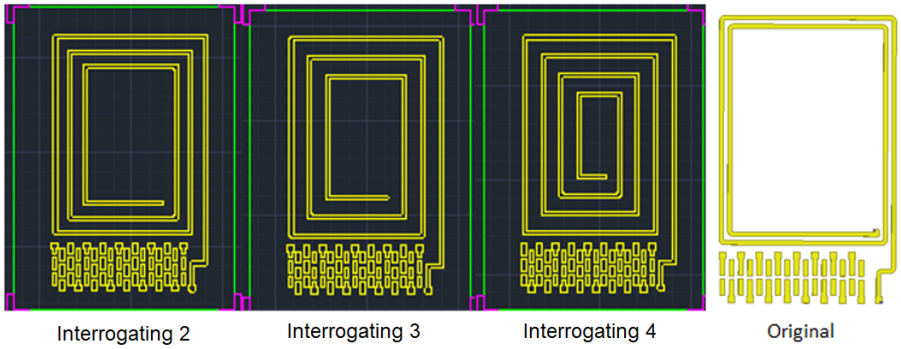

Figure 25: Interrogating antenna designs.

In Figure 25, the number of loops and the spacing between loops were varied with respect to the design parameters indicated in Figure 22. The parameters for each of these antennas is presented in Table 1.

Table 1: Antenna designs and design parameters.

Antenna:	Original	Interrogating 2	Interrogating 3	Interrogating 4
Design Parameter:	2 Loops 1 Width Spacing	3 Loops 3 Width Spacing	3 Loops 4 Width Spacing	4 Loops 4 Width Spacing

For the remainder of the thesis, the interrogating antenna designs will be referenced as one through four, where interrogating antenna one is the original antenna, and two through four are the designs from left to right in Figure 25.

Interrogating Antenna Impedance Transformation

After determining possible designs for the interrogating antenna with respect to self-resonance, it was necessary to understand effects of matching or tuning upon antenna

performance. Previous research suggested that tuning the interrogating antenna to maximize the current required “short circuit tuning”. The term “short circuit tuning” refers to the ideal case where the series resistance of the impedance is zero, and the inductive component of the antenna was tuned to a short circuit equivalent impedance to maximize the magnetic field generated by the antenna. However, previous HFSS simulations proved that the series resistance was far from zero. To understand the ideal method for tuning the interrogating antenna when series resistance is considered, ADS was used. ADS allowed for simulation of high frequency AC lumped element models which were useful to determine the optimum tuning or matching for a given microwave circuit. The model for the interrogating antenna must consider the antenna and the VNA both as a source and load, depending upon whether the signal is going to or coming from the sensor. The matched condition was considered to represent the optimum for two-way communication. Since the VNA has a 50-ohm impedance, simulated S_{11} results were used to determine if the load is mismatched. AC simulation indicated whether the current through the interrogating antenna’s lumped element model was at a maximum. The impedance of interrogating antenna 4 is shown at 300.5 MHz with the simple case of tuning where a single capacitive tuning element is used. This is presented in Figure 26.

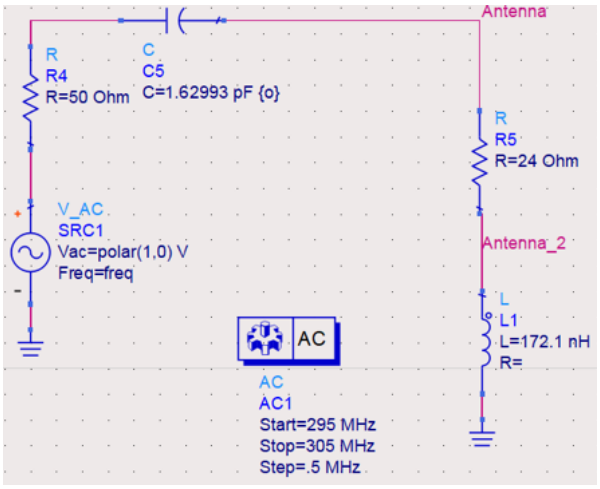

Figure 26: Interrogating antenna lumped element AC simulation model.

The first case with a single tuning element in series examined the simplest case with one degree of freedom. This was the method by which the previous state of the art system was tuned. Using the optimization tool in ADS the goals of the optimization were set such that C5 was adjusted until the current through R5 in Figure 26 was at a maximum. The optimization tool in ADS performs automated adjustment of chosen component values to reach a goal. For this case the goal was set to maximize the current through R5 in Figure 26. When the interrogating antenna acts as the source and the VNA as the load, the goal was set to maximize the power delivered to R4 in Figure 26. To perform this function in ADS, a range of capacitance values must be set. For tuning with a single capacitor, the optimization range was set between 0.1 and 30 pF. The results indicated that a series capacitance of 1.63 pF was necessary to tune the interrogating antenna. The magnitude of the current flowing through the interrogating antenna was plotted in the ADS environment. The current plotted in amps was calculated as the difference between the magnitude of the voltage across the resistance of the interrogating antenna, divided by

the resistance of the interrogating antenna. The magnitude of the current when the interrogating antenna was tuned with a single tuning element is presented in Figure 27.

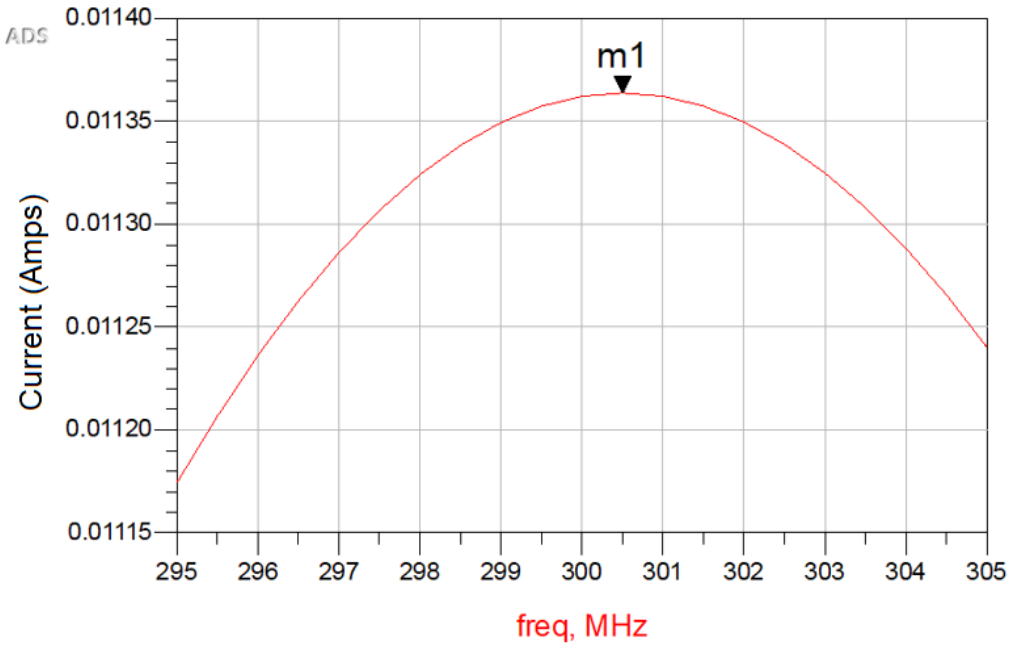

Figure 27: Simulated current through interrogating antenna using single series tuning element.

Power delivered to the real part of the interrogating was calculated as the magnitude of the voltage across the characteristic impedance Z_o multiplied by the characteristic impedance. The equivalent circuit for the tuning simulated in ADS for a single capacitor for Interrogating 4 presented in Figure 28.

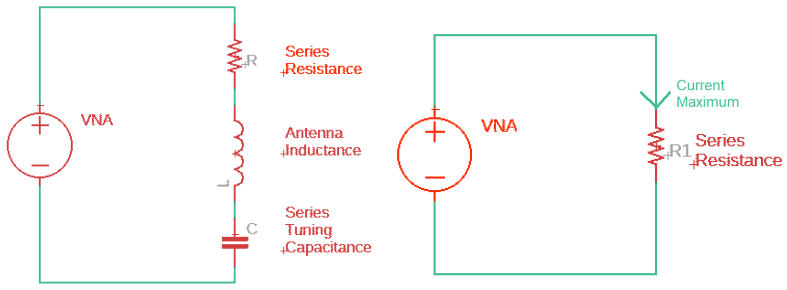

(a) (b)

Figure 28: (a) Equivalent circuit (b) circuit with resonance.

The same process for optimization was conducted with the VNA acting as the load, where the goal was set to calculate the capacitance when maximum power was delivered to the VNA. The final series capacitance values required for each interrogating antenna at 300.5 MHz is presented in Table 2. All simulation results are available for reference in Appendix C.

Table 2: Series capacitance values, current through antenna and power to VNA at 300.5 MHz.

Antenna:	Interrogating 1	Interrogating 2	Interrogating 3	Interrogating 4
Antenna Impedance (300.5 MHz)	24+j324 Ω	32+j331 Ω	36+j349 Ω	38+j439 Ω
Series Capacitance (1 Element)	1.63 pF	1.6 pF	1.51 pF	1.2 pF
Current (Through Antenna)	11.4 mA	11.62 mA	12 mA	13.5 mA
Power (Delivered to VNA)	6.45 mW	6.76 mW	7.425 mW	9.125 mW

The optimum case is when the interrogating antenna is matched to the 50 Ω characteristic impedance of the VNA. The circuit model used in ADS for this case and Interrogating 4 is presented in Figure 29.

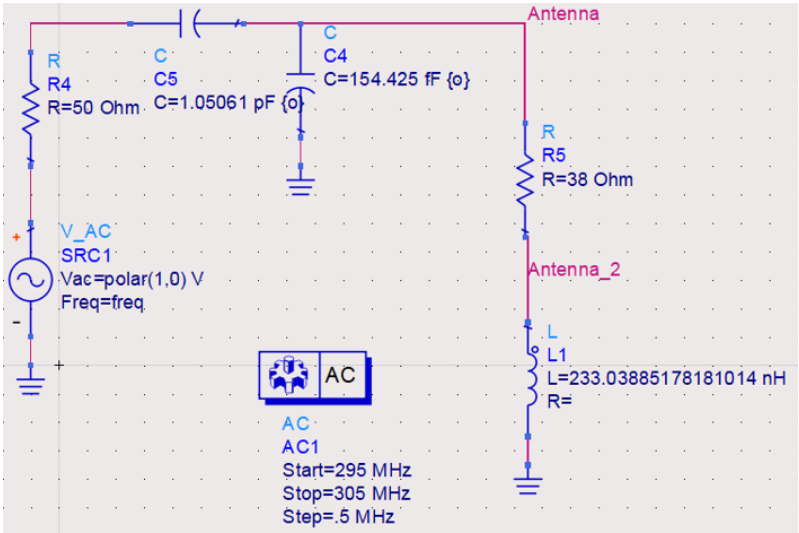

Figure 29: 2 elements tuning of interrogating antenna.

The circuit presented in Figure 29 used two capacitors as the matching network, the first in series followed by a parallel capacitance. By using two components, the input impedance of the matching network and the interrogating antenna became 50 ohms. To achieve this goal, the two capacitance values were adjusted using the optimization tool in ADS. The range for capacitance values was set to 0.1 pF to 30 pF. While there are two potential configurations for use of two capacitances for matching (as indicated in Figure 17) the second configuration was chosen because the first could not be optimized using capacitance values within the chosen range. Capacitance values outside the chosen range would not have been feasible for implementation. To determine if the circuit was matched, the reflection coefficient was plotted on a Smith chart, and the impedance was plotted. The results are presented in Figure 30.

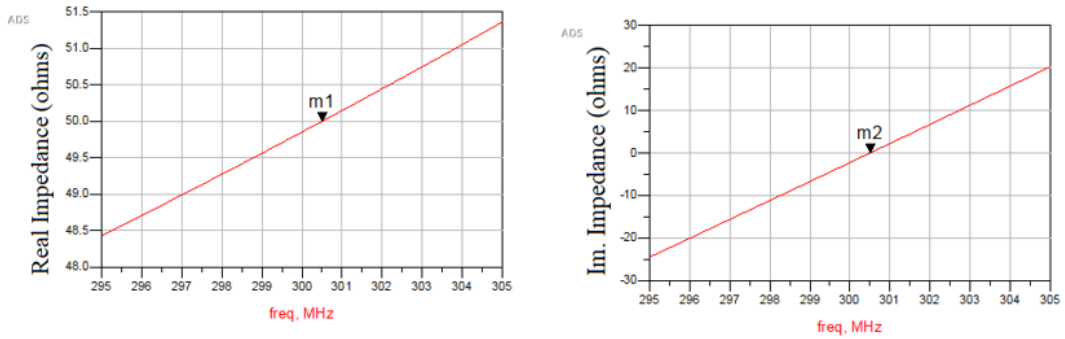

(a) (b)

Figure 30: (a) Real part of impedance calculated from S_{11} simulated result, (b) imaginary part of impedance calculated from S_{11} simulated result for matching using L circuit.

With the S_{11} simulation indicating that the input impedance was matched to the source, the current could then be simulated using an AC simulation of the circuit at 300.5 MHz. The current was calculated using the same method previously indicated for the interrogating antenna.

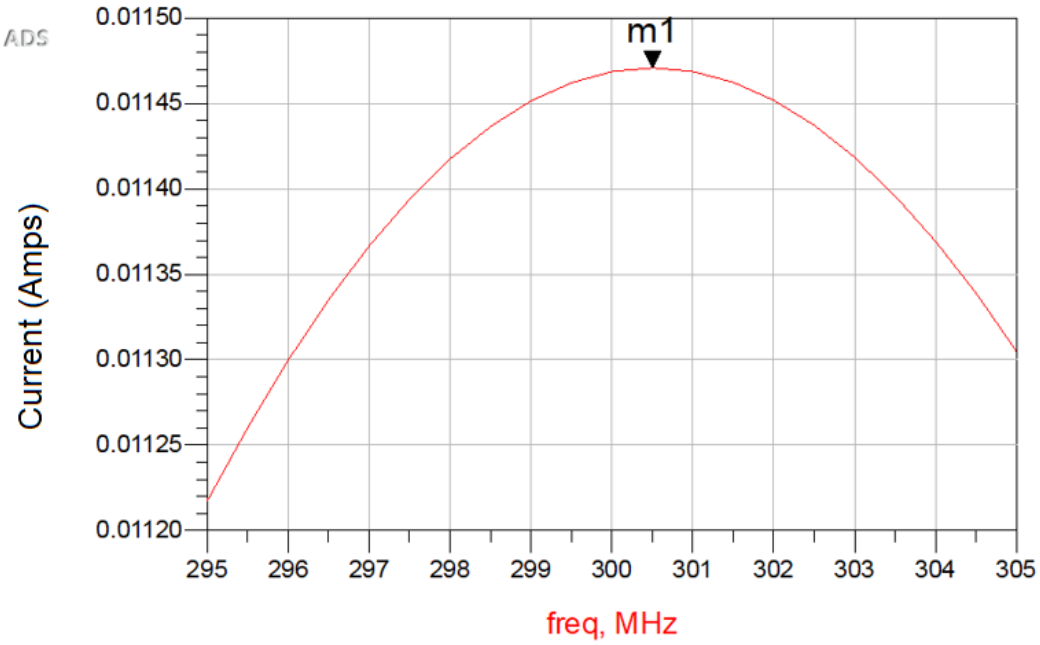

Figure 31: 2 elements tuning of interrogating antenna current simulation.

When comparing the results presented in Figure 31 to the results in Figure 27, the results indicate an improvement with matching of 0.88 %. The results in Figure 31 show that by using a second tuning element, the real component of the interrogating antenna can be matched to 50 ohms. Since the series impedance of interrogating antenna #4 is 38 ohms, matching only produced a less than 1% improvement in the current. So, a single tuning element would be practical.

All other interrogating antenna designs were simulated at 300.5 MHz. All simulation results for the matched case are available in Appendix D. Tuning elements used for the simulations were produced using ADS's optimization tool with the same range for potential component values. The final values required to match the interrogating antenna to the 50 Ω characteristic impedance of the VNA are presented in Table 3.

Table 3: Capacitance values, current through antenna and power to VNA at 300.5 MHz (Matched Case)

Antenna:	Interrogating 1	Interrogating 2	Interrogating 3	Interrogating 4
Antenna Impedance (300.5 MHz)	24+j324 Ω	32+j331 Ω	36+j349 Ω	38+j439 Ω
Series Capacitance (2 Element)	1.133 pF	1.22 pF	1.29 pF	1.05 pF
Parallel Capacitance (2 Element)	501.3 fF	395 fF	229 fF	154.4 fF
Current (Through Antenna)	11.475 mA	11.8 mA	12.5 mA	14.5 mA
Power (Delivered to VNA)	8.65 mW	9.65 mW	12.2 mW	21.6 mW
% Improvement in Current	0.66%	1.55%	4.17%	7.41%
% Improvement in Power	34.11%	42.75%	64.31%	136.71%

Contents of Table 3 regarding improvement in current and power are made with reference to Table 2. The results indicate that among all four designs, the improvement due to use of two elements for matching is less than 10% regarding current. For power however, the results indicate significant improvement. The results also indicate that the values for the parallel capacitance when matching are in the fento-farad range. This is not practical for implementation. Attempts at making parallel capacitances in the fento-farad range would be on the order of parasitic capacitance.

HFSS was also used to simulate the improvement in magnetic field magnitude which occurs when tuning the interrogating antenna. Tuning structures were connected in the HFSS environment using platinum wires with 1 mil thickness. The tuning structures can be bonded to form a capacitance or an inductance depending upon how the structures are connected. Capacitive equivalent impedance of the tuning structures is achieved by connecting segments of electrodes as finger pairs like an IDT. Inductive tuning is achieved by connecting each line of structures together, and then connecting each

segment in series with the next. Figure 32 indicates the two different ways that the tuning elements can be bonded to form capacitance or inductance.

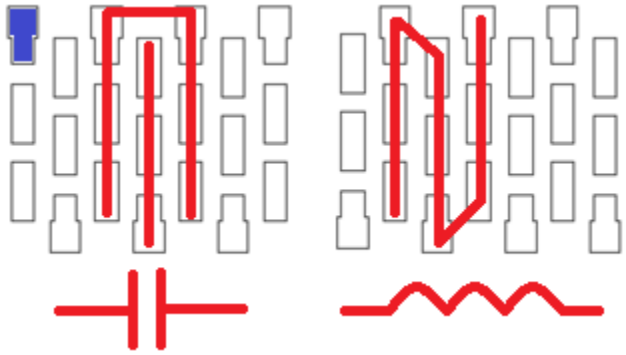

(a) (b)

Figure 32: (a) Tuning elements bonded capacitively to form a single equivalent capacitance pair (b) tuning elements tuned inductively to form a single equivalent inductive pair.

In Figure 32 (a), the first pair of elements contains three elements, where an element is a single line of three tuning segments. A single segment is presented in Figure 32 (a) in blue.

Figure 33 presents the configuration of tuning structures to form a series capacitance in the HFSS environment.

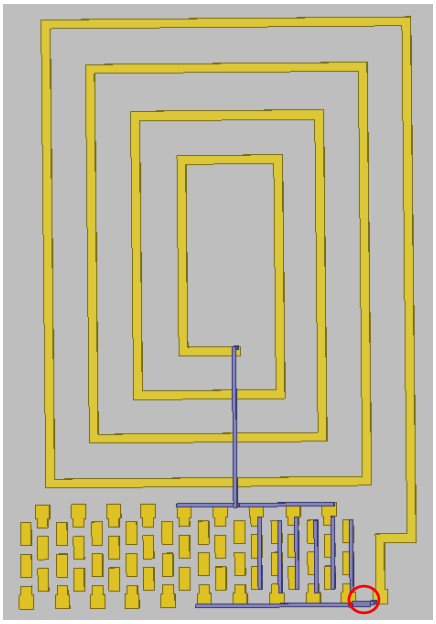

Figure 33: Tuned interrogating antenna in HFSS environment.

The equivalent impedance of the series capacitance tuning required to tune each interrogating antenna in HFSS was not calculated. The correct number of the tuning structures required to achieve a final tuned result was determined when the reflection coefficient crossed the real axis of the Smith chart at the operation frequency. All HFSS simulation results were conducted at an operation frequency of 334 MHz. The red circle highlights the location of the simulation port in

Figure 33. A close up of a port is shown in Figure 18 (b) for visual reference. A 2D plane connects between the 1 mil platinum connections and represents the port where the antenna is excited in the HFSS environment. To identify which combination of tuning and optimized antenna design produces the largest magnetic field, each interrogating antenna was simulated for both the non-tuned and tuned cases. The magnetic field was simulated in a radiation boundary that was set to be 100 mm by 100 mm by 100 mm. Magnetic field magnitude is quantified on 2D planes which can be declared within the radiation boundary with dimensions of 100 mm by 100 mm. Multiple 2D planes were spaced 1 mm apart to maximize resolution in the magnetic field magnitude on the top plane. The top plane was positioned 24 mm above the substrate of the interrogating antenna. The simulation parameter set was a Far Field analysis. Simulation results were compared between Perfect H-Field analysis, Perfect E-Field analysis, and Far Field analysis. Far Field was selected because change in the radiation boundary does not influence magnetic field magnitude simulation results. The simulation environment for the interrogating antenna is presented in Figure 34.

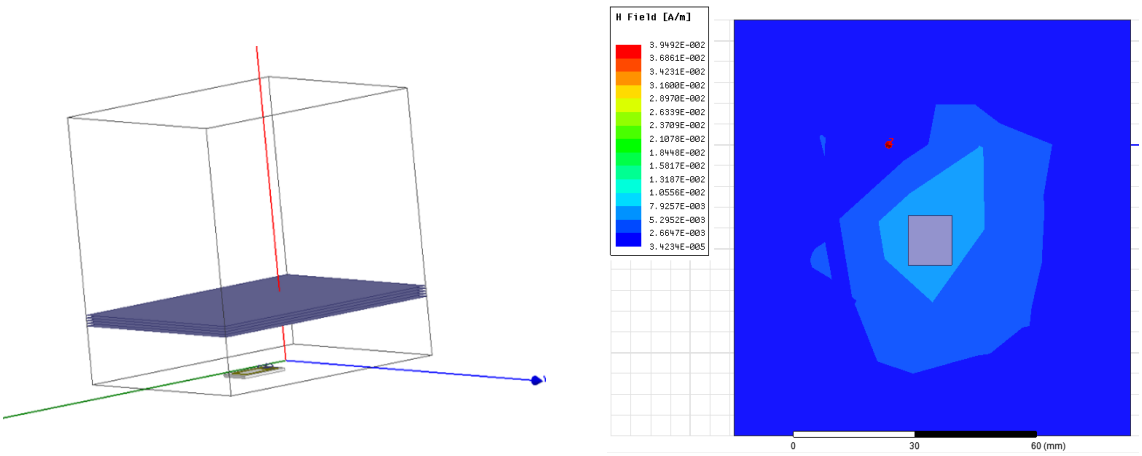

(a) (b)

Figure 34: (a) Far field radiation boundary, H field planes and antenna, (b) Top view of simulation results

In Figure 34 (a), the Z direction is denoted as the red line, while the Y direction is the green line and the blue line is the x direction. The antenna is positioned in the center of the radiation boundary, with the bottom of the substrate on the same plane as the XY plane. In Figure 34 (b) the top view of the simulation result is presented. The grey rectangle in Figure 34 (b) is a 10.5 mm by 10.5 mm plane used to average the magnetic field magnitude within an area equal to the area of the sensing antenna. The simulation results were evaluated at 334 MHz. All simulated results in HFSS for the interrogating antenna are available for reference in Appendix B. Magnetic field magnitude simulation results are presented in Figure 35. To understand the correlation between each design, and the graph in Figure 35, a table of design parameters is presented in

Table 4.

Table 4: Antenna Design Parameters

Interrogating Antenna	Original or Modified	# Loops	Line Width Spacing	Tune or Not Tuned
1	Original	2	1	Not Tuned
2	Original	2	1	Tuned
3	Modified	3	3	Not Tuned
4	Modified	3	3	Tuned
5	Modified	3	4	Not Tuned
6	Modified	3	4	Tuned
7	Modified	4	4	Not Tuned
8	Modified	4	4	Tuned

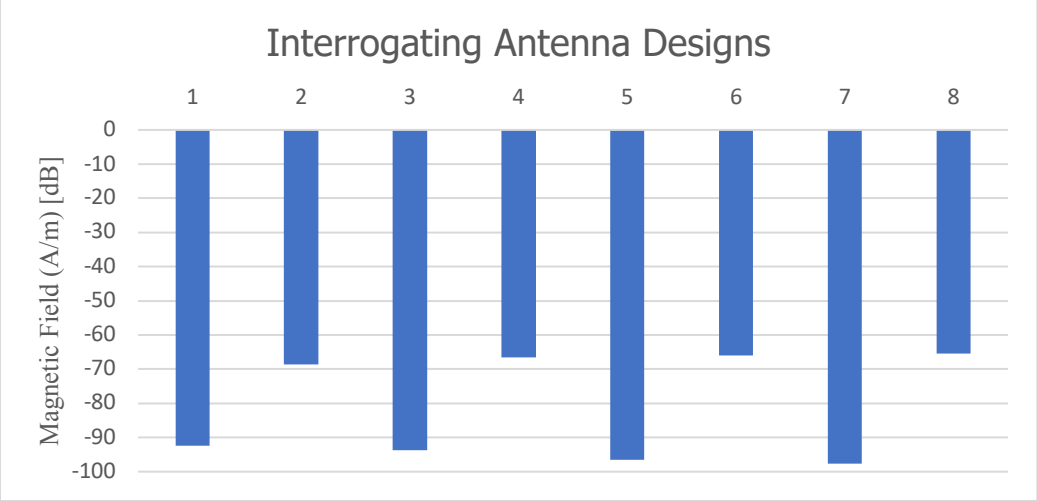

Figure 35: HFSS magnetic field simulation results.

The results indicate that the interrogating antenna magnetic field shows by 25-30 dB when tuning with a series capacitance. Maximizing the number of loops to four with Interrogating 4 resulting in a 3.2 dB improvement in comparison to the original 2 loop design. These results indicated that tuning the interrogating antenna has a significant impact in maximizing the wireless communication distance, and that the indicated interrogating antenna 4 is the optimum interrogating antenna design for the size and frequency considered.

Sensing Antenna Design

For the case of the sensing antenna, the goal was to introduce tuning capability to the design because previous sensing antenna designs did not. To further improve the design, additional loops were also added to the antenna when increasing the footprint to add tuning structures to the antenna design. The original antenna design consisted of a 2-loop structure indicated in Figure 36.

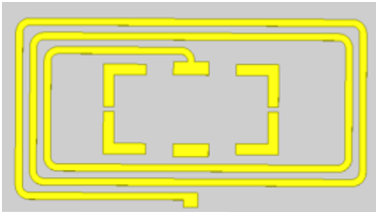

Figure 36: 2 loop antenna design for sensing antenna.

To include tuning elements on the device it required that the footprint of the new sensing antenna be increased from a 5x10.5 mm footprint to a 10.5x10.5 mm. Because the footprint was increased a single loop was added to the sensing antenna. Simulations were conducted using HFSS to ensure that adding an additional loop to the which did not lead to the antenna becoming self-resonant near the frequency of interest (approximately 300 MHz). The same criteria were applied to the new sensing antenna to ensure the impedance at 300 MHz did not exceed 10% of the impedance at the point of resonance. HFSS simulation results for self-resonance of the sensing antenna are available for reference in Appendix A. Simulation results for the sensing antenna are shown in Figure 37.

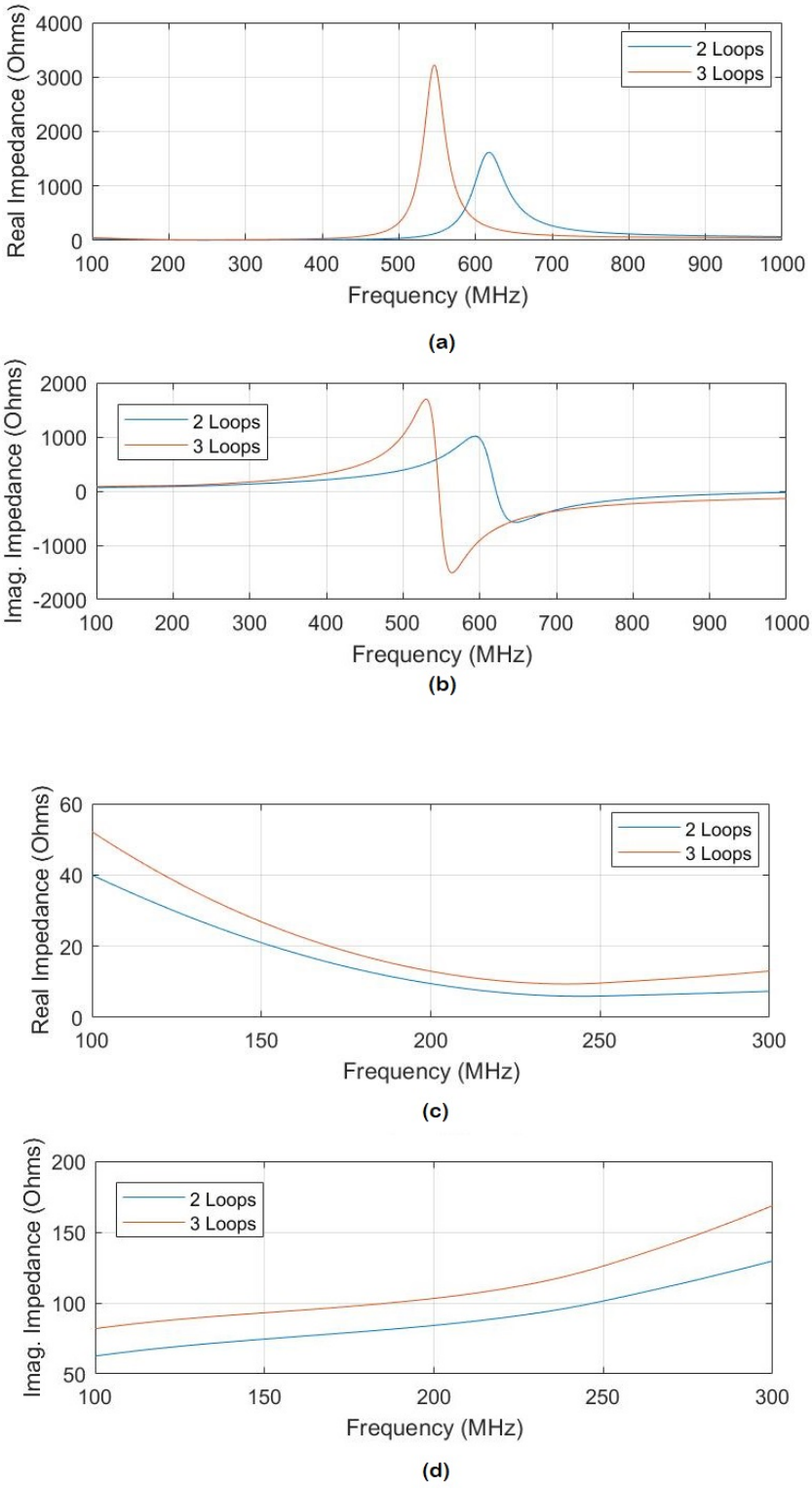

Figure 37: Plot of impedance comparing 2 loop and 3 loop sensing antennas, (a) real impedance, (b) imaginary impedance at resonance, (c) real impedance, (d) imaginary impedance before resonance.

The final design to be implemented is presented in Figure 38 shows a comparison between the new and original designs.

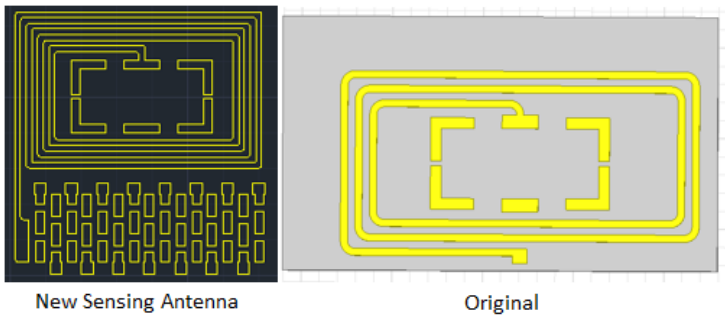

Figure 38: New sensing antenna design vs original sensing antenna design.

The new tuning elements added to the sensing antenna are identical in size as the tuning elements present on the interrogating antenna. The tuning structures on the sensing antenna function the same and can be connected as a capacitance or as an inductance.

Sensing Antenna Impedance Transformation

Impedance transformation required to match the sensing antenna and SAW device requires understanding of the circuit model for the SAW device connected to the sensing antenna. Because transmission of power for the wireless link using magnetic field coupling is two-way communication, when the sensing antenna receives a signal, the SAW is the load and when the SAW sends the signal back, the antenna is the load. There are two different circuit models which represent the two modes of operation, presented in Figure 39.

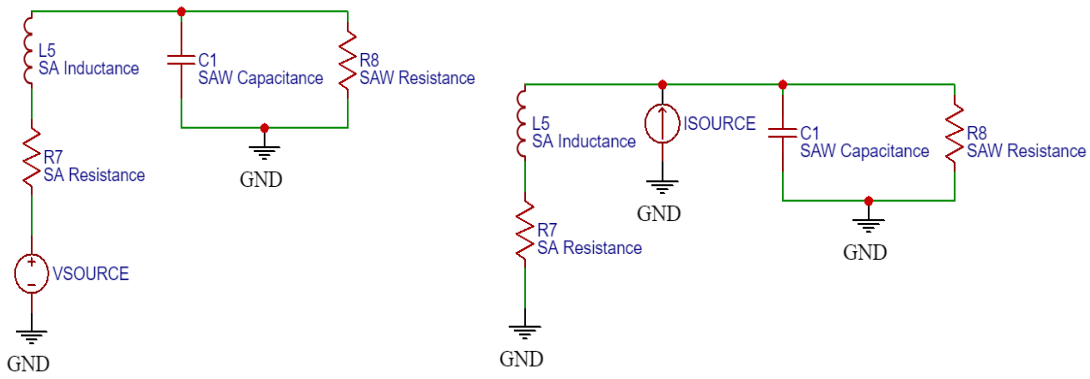

(a) (b)

Figure 39: (a) Sensing antenna and SAW schematic with SA source, (b) sensing antenna and SAW schematic with SAW source.

Sensing antenna impedance was measured using a network analyzer. SAW admittance was calculated by measuring a SAW device which operates at 300.5 MHz. The SAW impedance was modeled using the same methods described in Chapter I. The SAW admittance and impedance used for ADS simulation is presented in Figure 40.

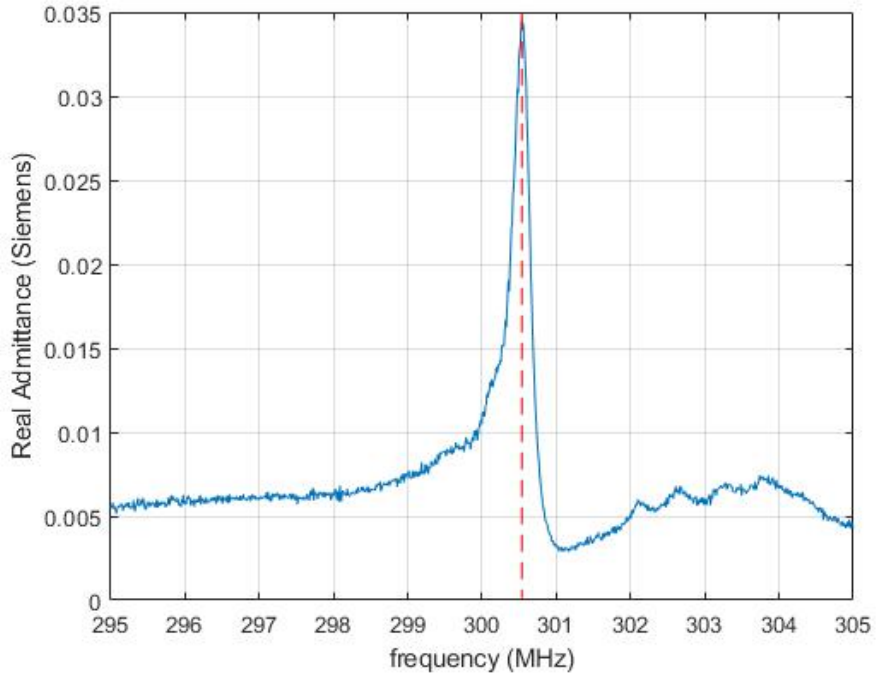
Real Admittance (Siemens)
0.035
0.03
0.025
0.02
0.015
0.01
0.005
0
295
296
297
298
299
300
301
302
303
304
305
frequency (MHz)

(a)

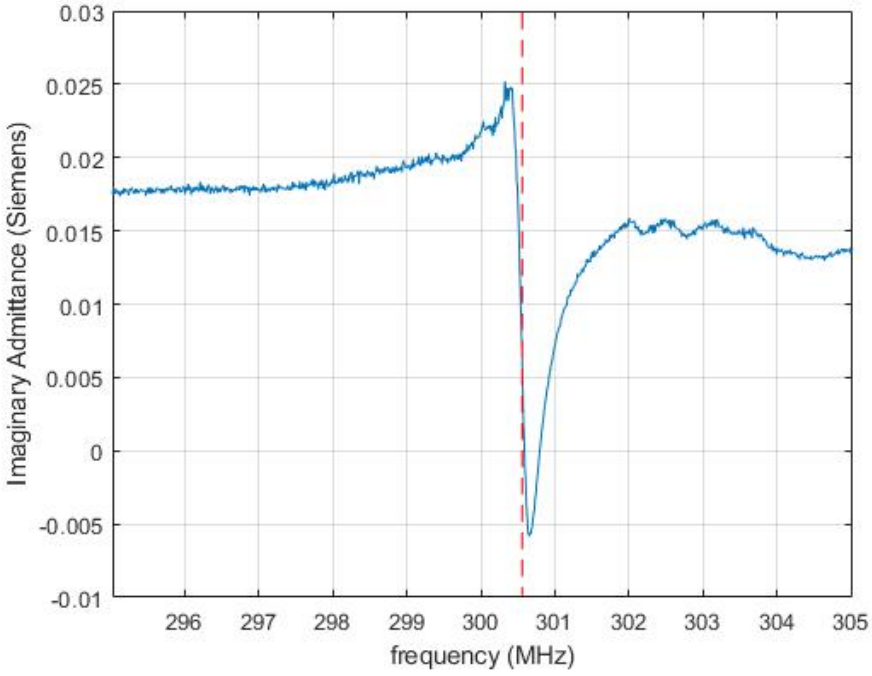
Imaginary Admittance (Siemens)
0.03
0.025
0.02
0.015
0.01
0.005
0
-0.005
-0.01
296
297
298
299
300
301
302
303
304
305
frequency (MHz)

(b)

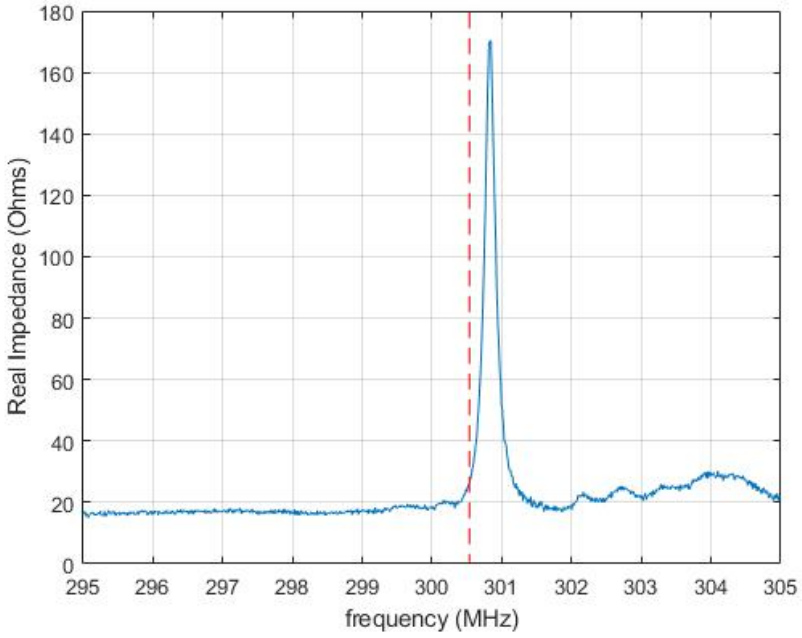

(c)

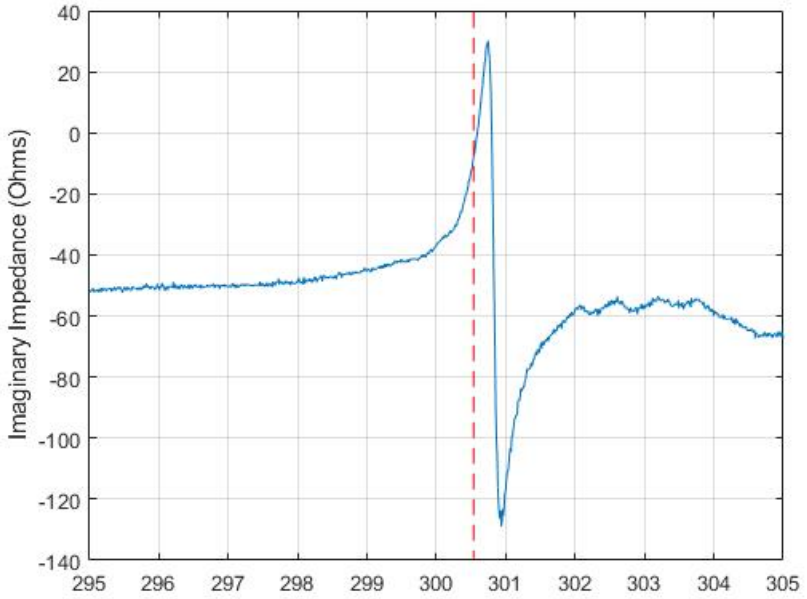

(d)

Figure 40: (a) Real SAW admittance, (b) imaginary SAW admittance, (c) real SAW impedance, (d) imaginary SAW impedance used for ADS simulation of sensing antenna.

The series impedance taken from the plot presented in Figure 40 was 25.9487-j9.3988 ohms. This impedance was taken at 300.5 MHz, which is the frequency at which the conductance of the SAW was at a peak amplitude. The impedance for the new sensing antenna was 10.34 – j249.6 ohms. AC analysis was conducted for the SAW device and the sensing antenna with respect to three different networks. The first matching network considered was a T circuit, which has three tuning elements. The second matching network considered was the L circuit tuning network also considered for the interrogating antenna and the last was a single tuning element. The location where tuning and matching networks will be placed in the circuit is shown in Figure 41.

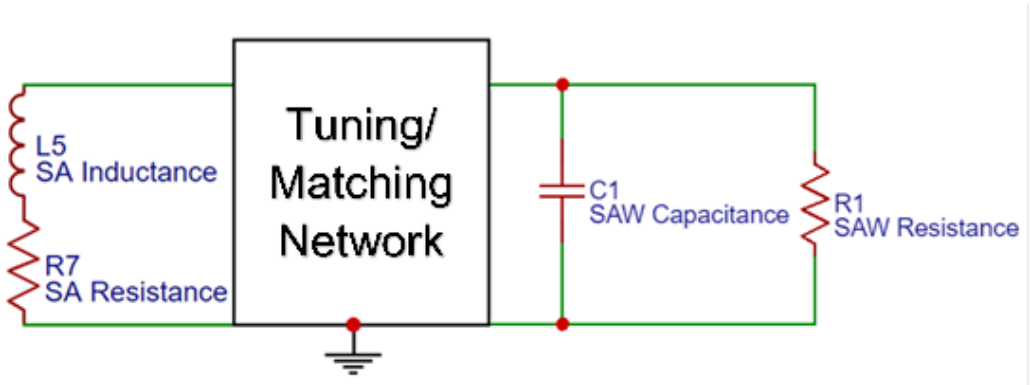

Figure 41: Circuit model and tuning/matching network connected in the circuit.

The first matching network considered is the T circuit. There are a total of 6 different T circuit configurations which can be considered to match the sensing antenna to the SAW. The different configurations are presented in Figure 42. Note that the values that are presented in Figure 42 are not the values required to match. The values for components used in each configuration were optimized using ADS optimization tools. Optimization goals were set in the ADS environment such that the current through the sensing antenna was a maximum when the SAW was the source, while goals were set to maximize power delivered to the real part of the SAW when the sensing antenna was the source. Current

was calculated in the ADS environment as the magnitude of the voltage across the series resistance of the sensing antenna, divided by the sensing antenna's series resistance. Power was calculated as the absolute value of the voltage across the parallel equivalent resistance of the SAW multiplied by the parallel equivalent resistance of the SAW. The range for potential capacitance values was used from 0.1 to 30 pF, while the range for potential inductances was 0.1 nH to 5 nH. These ranges of component values were chosen to set bounds on implementable values which could be used to tune inductively or capacitively using tuning structures on the sensing antenna.

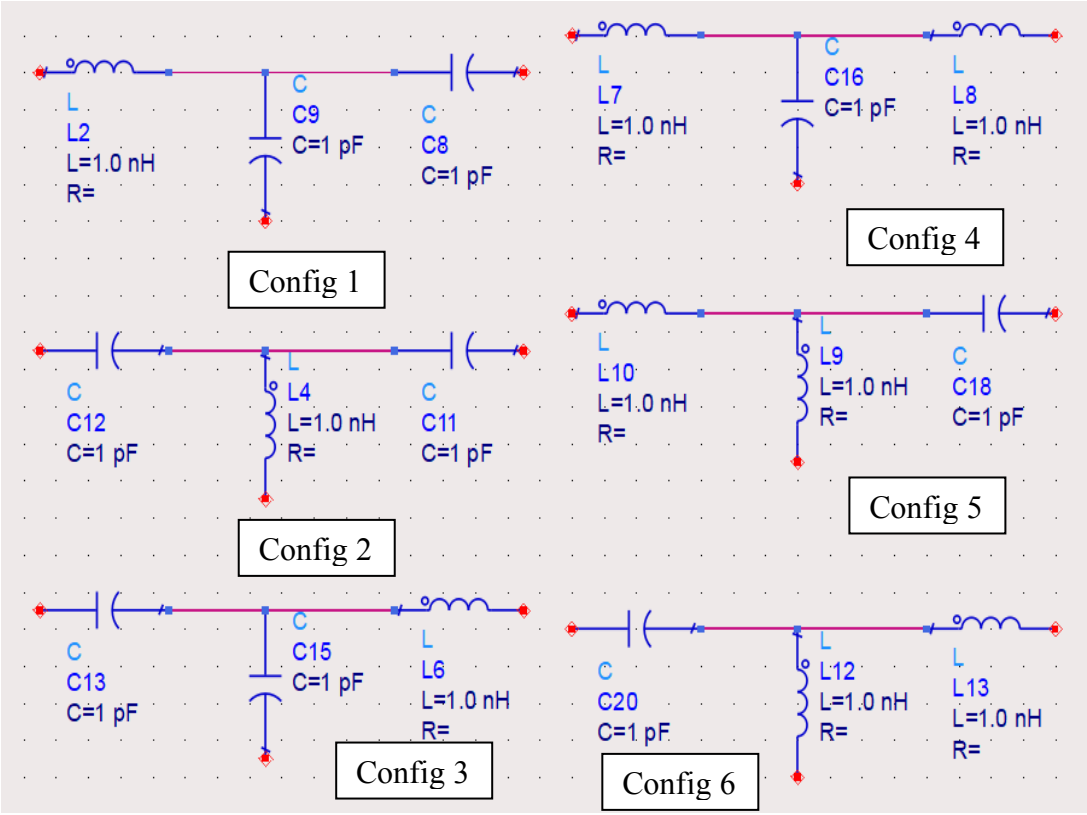

Figure 42: T circuit configurations for sensing antenna and SAW tuning.

The different T circuit configurations in Figure 42 were simulated in the ADS environment and each circuit was optimized to achieve optimum result. An example schematic with final optimized values were the SAW is acting as the source is presented in Figure 43.

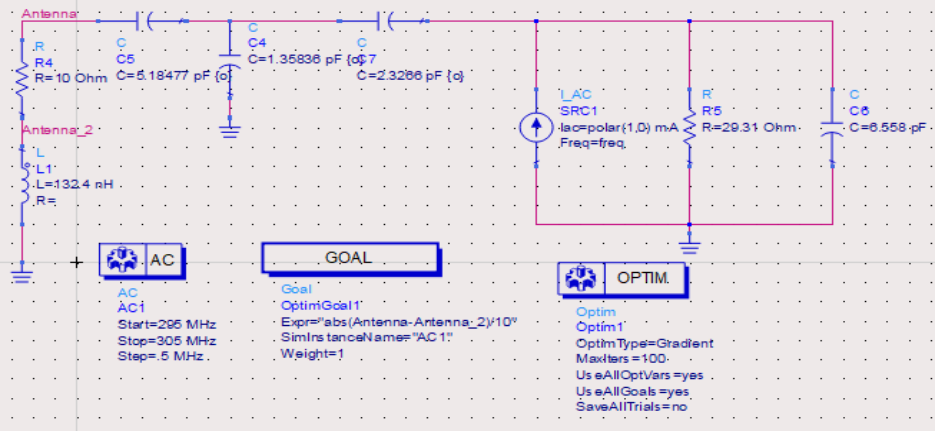

Figure 43: T circuit matching network used to match sensing antenna to SAW with SAW as source.

The results of simulation of current through the sensing antenna and power delivered to the parallel resistance of the SAW are presented in Table 5. All simulation results for the sensing antenna are available in Appendix E.

Table 5: Comparison of T circuit configuration with current and power.

	Conf. 1	Conf. 2	Conf. 3	Conf. 4	Conf. 4	Conf. 6
Current	856 µA	115 µA	856 µA	113 µA	316 µA	740 µA
Power	25 mW	667 µW	25 mW	435 mW	324 µW	20 mW

The results in Table 5 indicate that the two best cases were configuration 1 and configuration 3. For both cases, the results indicate that the SAW device and the sensing antenna were matched. This was determined by using a 50-ohm simulation element in replacement of the sensing antenna and simulating the S_{11}. Simulation of the S_{11} with respect to 50 ohms simulated the input impedance looking into the tuning network and the SAW. The simulation results are presented in Figure 44.

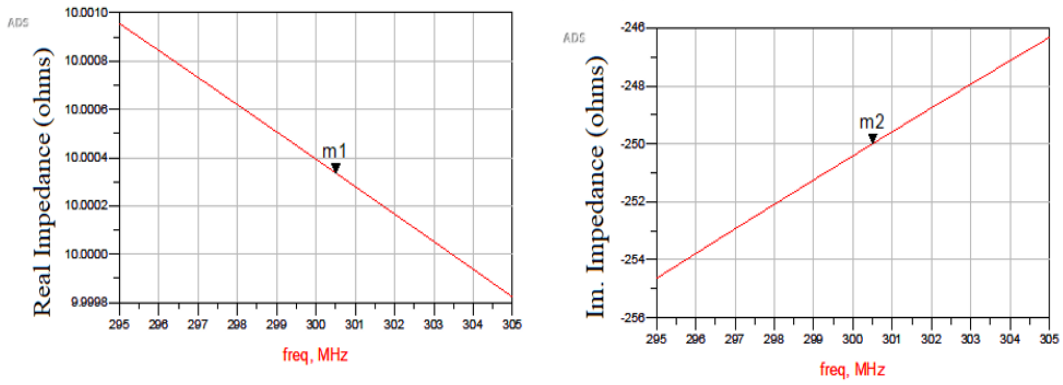

(a) (b)

Figure 44: (a) Real part of impedance calculated from S_{11} simulated result, (b) imaginary part of impedance calculated from S_{11} simulated result for matching using T circuit.

The results indicate that the equivalent impedance is 10 – j249.9 ohms, meaning that the impedance of the SAW was matched to the impedance of the antenna. Thus, configuration 1 and 3 were the two configurations which matched the circuit. The final component values are presented in Figure 45.

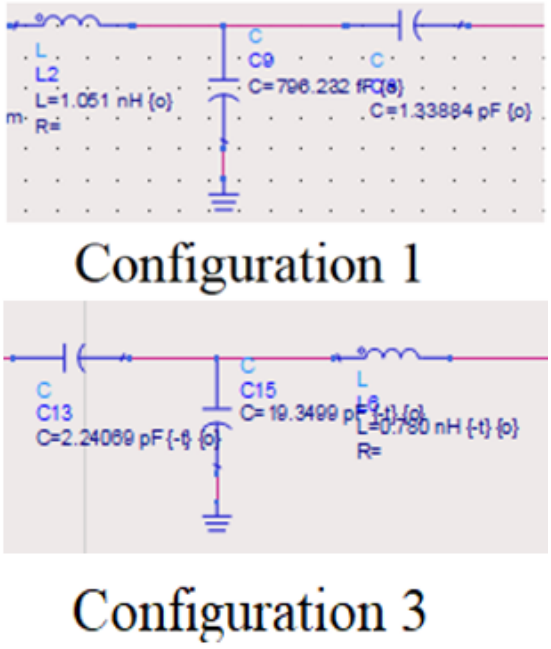

Figure 45: Comparison of matched T circuit configurations.

While the results indicate a T circuit can match, capacitances below 1 pF are not implementable. Simulations were conducted to further restrict the range of values used in

ADS optimization to capacitance above 1 pF and inductance above 1 nH, and matched conditions were not achievable. All simulation results for the sensing antenna matching are available for reference in Appendix E. The next case considered was matching using two elements. Both configurations of the L circuit were considered, presented in Figure 46.

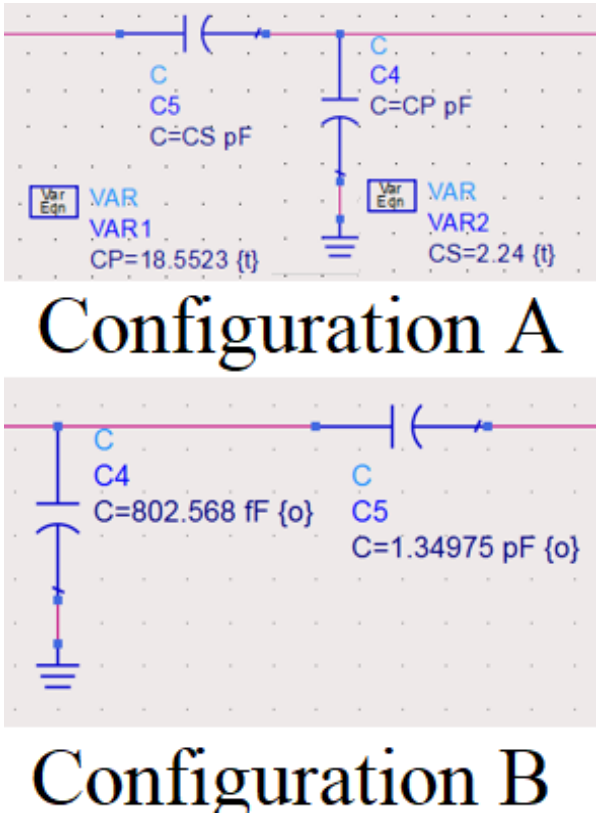

Figure 46: L circuit tuning networks between sensing antenna and SAW.

Capacitance is used for both components in for L circuit matching. Capacitance must be used because use of an inductance moves the reflection coefficient to forbidden regions when the system is normalized to the source impedance (either the SAW impedance or the sensing antenna impedance depending on the system model considered). Both circuits, with their respective values produced a matched condition equivalent to the results from configuration 1 and 3 of the T circuit. Configuration A provides a feasible

circuit for implementation, with a 2.2 pF series capacitance and an 18.55 pF parallel capacitance required to match.

Following this result, tuning via the use of a single capacitive element was considered. A single tuning element was optimized in the circuit using the optimization tool and a 0.1 pF to 30 pF range to result in a capacitance of 2.2 pF. The power delivered to the SAW and current through the sensing antenna were simulated. The simulation results are available for reference in Appendix F. The results proved that the same power delivered to the SAW and current through the sensing antenna were achieved using the T matching network and L matching network under the matched condition. The comparison between the matched and tuned simulated power and current for the best 1 element tuning and L circuit matching are presented in Table 6.

Table 6: Comparison of improvement between 1 element and 2 elements

	1 Element	L Circuit	% Improvement Tuning vs Matched	% Improvement Tuning vs Original
Current	770 μA	860 μA	11.69 %	31.2%
Power	20.2 mW	25 mW	23.76 %	49%

The results indicate that the use of a single element causes approximately 10% decrease in current through the real part of the antenna and approximately 20% decrease in power delivered to the real part of the SAW.

Magnetic field simulations were also conducted using HFSS to compare the original sensing antenna to the new sensing antenna design. The new sensing antenna magnetic field magnitude was simulated with tuning of a single capacitive element in series by the

same methods used for the interrogating antenna. The port impedance was changed to an equivalent impedance of 25.9487-j9.3988 Ω to simulate a characteristic impedance of a SAW. Note that this simulation does not accurately represent the magnetic field produced by a SAW device. The magnetic field cannot be simulated to represent the two-way communication of the interrogating antenna connected to the VNA and sensing antenna connected to the SAW sensor. A figure of the plane representing the gradient of magnetic field with respect to distance is presented in Figure 47.

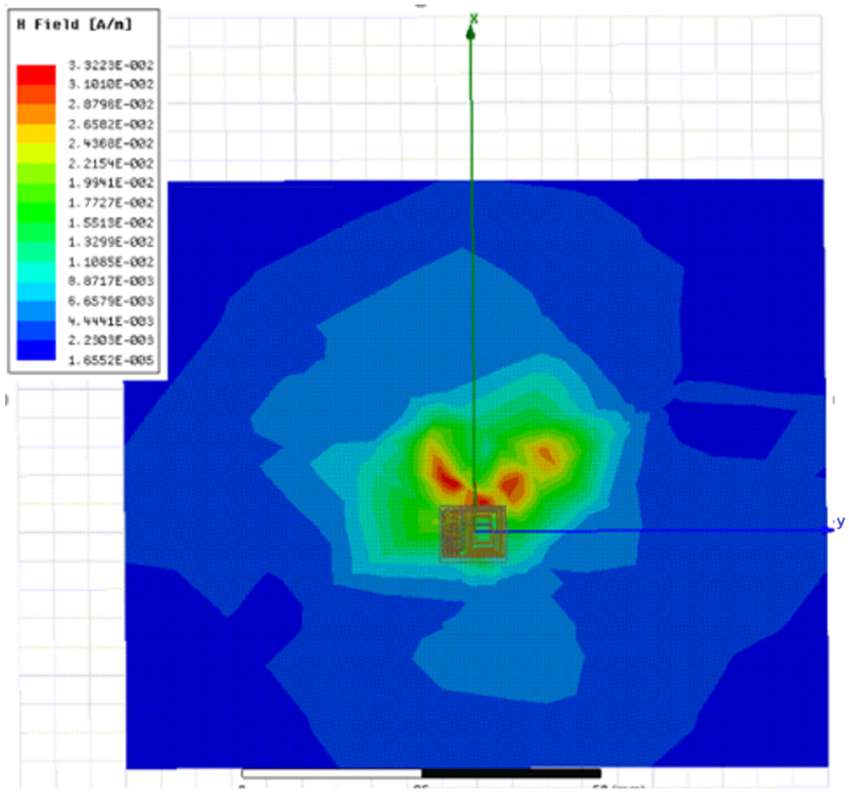

Figure 47: Magnetic field simulation of sensing antenna.

Presented in Figure 47 is an image of the HFFS environment with the magnetic field magnitude simulated. The image presents a view of the sensing antenna from the bottom, looking in the positive Z direction. The x direction is indicated in the image while the Y direction is to the right. This perspective indicates that magnetic field magnitudes are

highest on planes closest to the antenna but diminish as distance increases between planes and the antenna within the radiation boundary. The magnetic field was simulated in a radiation boundary that was set to be 100 mm by 100 mm by 100 mm. Magnetic field magnitude is quantified on 2D planes with dimension of 100 mm by 100 mm which are declared within the radiation boundary. Multiple 2D planes were spaced 1 mm apart to maximize resolution in the magnetic field magnitude on the top plane. The average magnetic field magnitude was calculated on the top plane which was 15 mm above the antenna substrate. The magnitude of the magnetic field was compared between the tuned case of the new sensing antenna and the case where the new sensing antenna was not tuned. When making this comparison, the simulation results indicated 20 dB improvement when comparing the averaged magnetic field magnitudes.

Antenna Fabrication

The new circuit designs for both the sensing and interrogating antennas were implemented in AutoCAD. The devices are fabricated using a thick film fabrication process, which requires that the AutoCAD files be transferred to a silk screen which was manufactured at Utz Technologies in Little Falls NJ. The silk screen process is depicted in Figure 48, where the device substrate is placed underneath the screen and gold paste is spread on top of the screen with a squeegee. The squeegee is used to transfer the pattern to the substrate by applying pressure at a constant rate such that the gold is deposited evenly upon the substrate. The complete process is indicated in Figure 48.

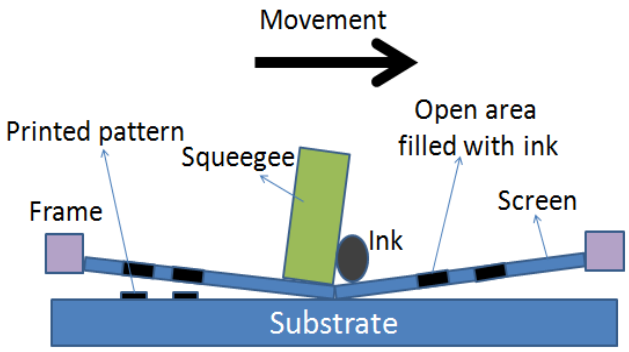

Figure 48: Screen printing process.

As depicted in Figure 48, a hand-squeegee is pressed down on the silk screen, which is covered in ink in the diagram. Figure 49 presents the silk screen fabrication setup used for deposition of the gold paste onto the alumina substrate. Figure 49 (a) presents the screen mounted on the fabrication stand for the sensing antenna, while (b) presents the screen for the interrogating antenna. The silk screen indicated in the figure is for the sensing antennas. All antennas are identical across the entire screen.

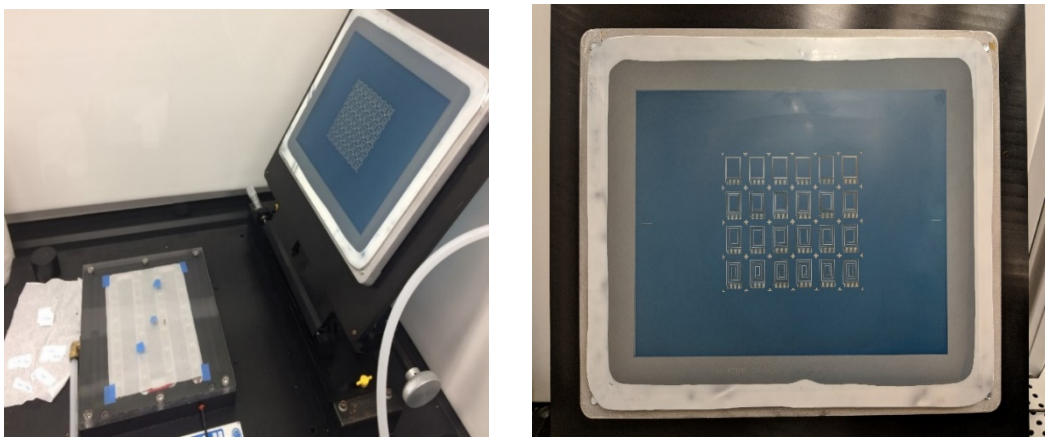

(a) (b)

Figure 49: (a) Sensing antenna screen on silk screen fabrication stand, (b) interrogating antenna silk screen.

The first row contains interrogating antenna 1 while each new design is produced in each following row.

Once the gold paste was deposited, the antennas were heated in a belt furnace for the required baking of the paste and then diced such that they could be tested. A top view of the antennas prior to their connection to coaxial lines is presented in Figure 50. Note that the figure does not include the prior state-of-the-art interrogating antenna. That antenna has the same design as Interrogating 1. The only difference is the tuning segments per element. The prior state-of-the-art tuning used two segments while the new antennas use three segments to increase tuning flexibility.

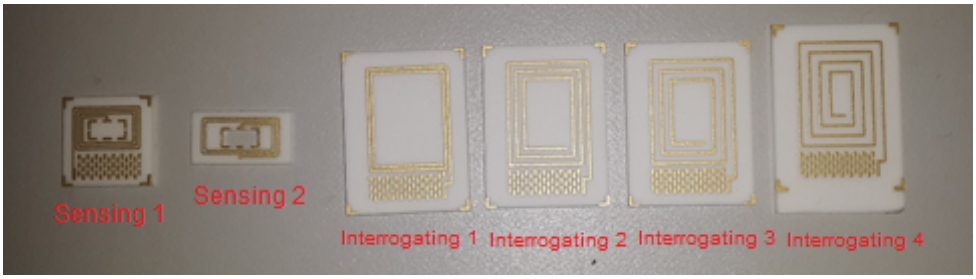

Figure 50: Image of fabricated antennas

Figure 50 shows the room temperature test fixtures used to mount the antennas and connect them to standard room temperature coaxial cables for antenna impedance measurement and tuning. Figure 51 shows each of the fixtures for impedance measurement of the sensing and interrogating antennas.

Figure 51: Fabricated antennas and their mounting fixtures.

Note that mounting fixtures connecting to the coaxial lines were made using plastic which was drilled and shaped to form a mechanically stable base for each antenna. Holes were drilled through the plastic bases where the coaxial line was fed through and epoxy was applied to the back of the base so that the coaxial line did not move after bonding.

CHAPTER III

RESULTS

After fabricating and mounting the antennas, they were ready for test and measurement. The first measurement that was conducted was the measurement of the impedance for the new tuning structures. Both new sensing antenna and interrogating antenna designs use the same design for the tuning structures. The impedance was measured for the structures bonded to form capacitance or inductance. This provided insight into the limits of available tuning capabilities. Following characterization of the tuning structures, transmission measurements between the sensing antenna and interrogating antenna were conducted. Transmission measurements tested three main variables: (i) improvement in signal strength using the new interrogating antenna designs; (ii) improvements by tuning interrogating antennas; and (iii) improvements by tuning the new sensing antennas.

Tuning Structure Impedance Measurement

To achieve capacitance or inductance behavior the structures were bonded differently. The first case considered is the characterization of capacitive tuning elements. The sensing antenna wafer was used for the characterization of the tuning elements. The bonded tuning elements in a capacitive manner are presented in Figure 52. Note that during the process of taking images of the tuning structures, the bond connection made between elements on the top of the structures was broken. The bond connection was not broken during measurement. All the elements were connected in parallel and measured together.

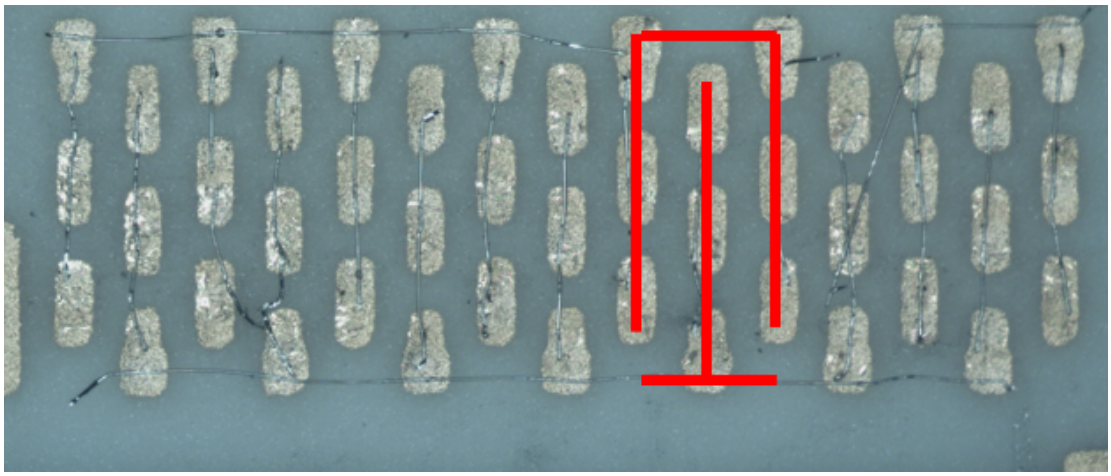

Figure 52: Capacitive bonding of tuning elements.

The total capacitance calculated by measuring the S_{11} at 300.5 MHz. The total capacitance was calculated as 7.8 pF. The calculated capacitance does not consider the bond wires which are used to access the structure shown in Figure 52. These wires connect between the structures in Figure 52 and the coaxial line which is used to measure the S_{11} with a VNA. The bond wires used to access the structures were measured as lengths of 13 mm and 6 mm respectively. The approximation for their impedance was made as 1 nH per mm. By adding ~13 nH and ~6 nH to the measured capacitance, the following equation can be used to calculate the approximate impedance of a single pair of capacitive tuning elements.

$$C_{eq} = \frac{1}{7*\omega(Z_{measured\_C}+Z_{LP})} \tag{22}$$

As indicated in (22), $Z_{measured\_C}$ is the total impedance measured for all 7 pairs of structures in parallel. The impedance of the parallel inductance from the bond wires used to access the structures is denoted as Z_{LP}. The value of the impedance for a single pair of tuning elements after using (9) was 0.73 pF. The same analysis was conducted with respect to the inductive tuning of the tuning elements with the configuration presented in Figure 53.

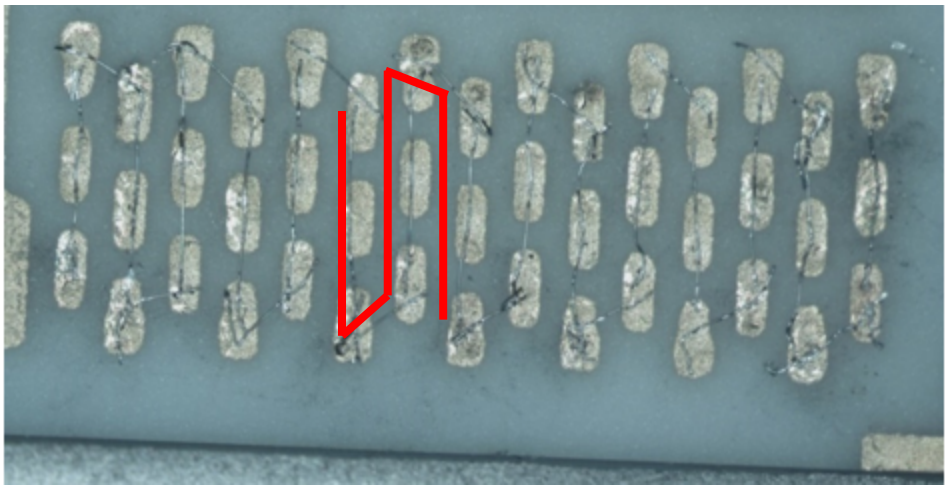

Figure 53: Tuning elements bonded for inductive tuning.

The total impedance of all inductive elements bonded in series was measured and was used to determine the impedance of a single pair of inductive elements by considering the parasitic effects of the bond wire connections to the coaxial lines. The equation used to calculate the equivalent capacitance is presented in (23).

$$L_{eq} = \frac{(Z_{measured\_L} - Z_{LP})}{j\omega * 7} \tag{23}$$

After using equation (23) the resulting equivalent inductance of a single pair of tuning elements is 3.5 nH. These results provide indication of reasonable values for inductance and capacitance which could be achieved during implementation and measurement.

Wireless Transmission Measurements

The initial test conducted was to identify the improvement of transmission distance by comparing each new interrogating antenna design without tuning. This comparison indicates potential improvement before tuning of the interrogating antenna to be correlated with simulation results for indication of the best interrogating antenna design. The measurement setup is presented in Figure 54.

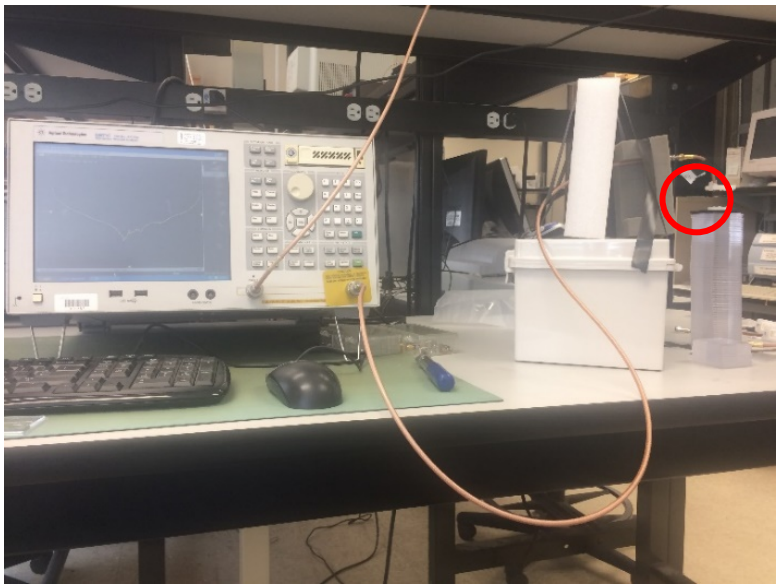

Figure 54: Measurement setup for wireless sensor interrogation.

The red circle in Figure 54 highlights the sensing and interrogating antennas under test. Chip tray covers with height of 2.5 mm were used as spacers to allow repeatable placement of the sensing antenna with respect to the interrogating antenna. The sensing antenna in Figure 54 is laid on top of the chip trays, with the interrogating antenna connected to the VNA. All coaxial lines used during the measurement were ambient temperature lines. The SAW sensor used for transmission measurement operates at a resonant frequency of 310.2 MHz. To ensure the measured S_{11} peak after time gating was in the center of the frequency span, the VNA was set to a frequency span of 300 MHz to 320 MHz. Time gating was used to measure the S_{11} of the SAW. The time gating was started at 300 nanoseconds and stopped at 5 microseconds. The time gating parameters were chosen because they were appropriate for measurement of S_{11} from past work. Time gating is used to eliminate electromagnetic signal reflections in time and using window functions enables the detection of the acoustic signal which is delayed due to propagation velocity five orders of magnitude lower than the electromagnetic wave's velocity of propagation.

The first measurement conducted was the measurement of each new interrogating antenna using the original sensing antenna. The interrogating antennas were not tuned to only measure changes in the S_{11} with respect to change in inductance associated with new designs. The previous interrogating antenna was used for baseline measurements in conjunction with the previously used sensing antenna. 15 mm was the chosen distance between the sensing and interrogating antenna because 15 mm was the maximum distance at which a detectable signal above the noise floor could be measured across all interrogating antenna designs. The results of this measurement are presented in Figure 55. The results show a 6-dB improvement in the time gated $|S_{11}|$ when using interrogating antenna four.

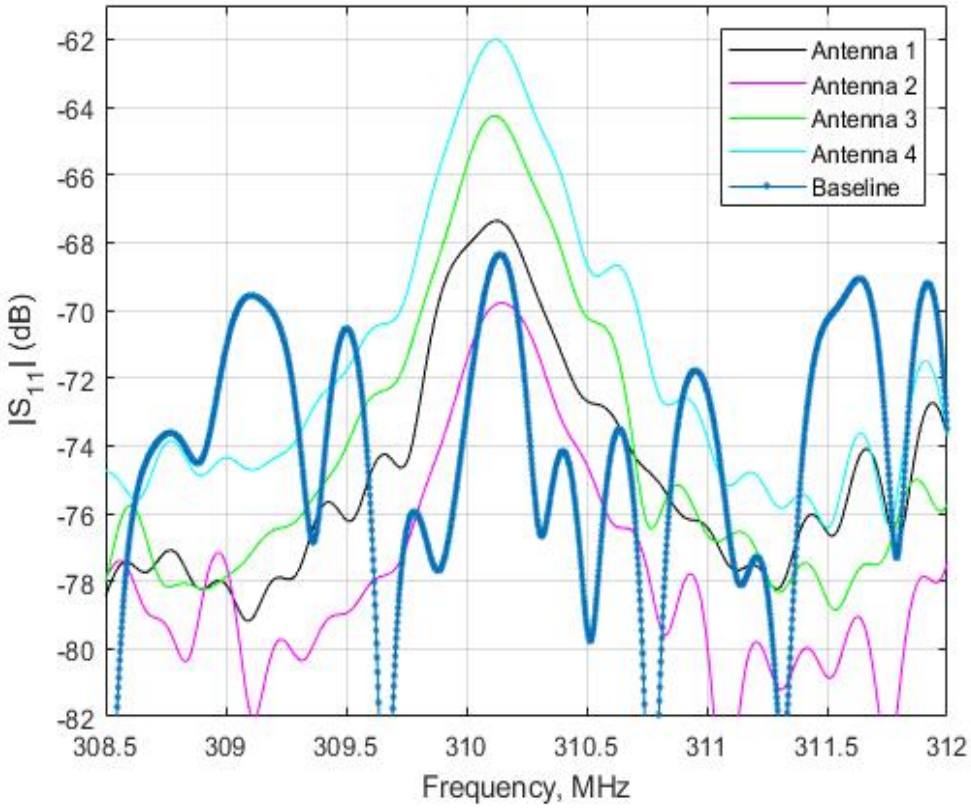

Figure 55: $|S_{11}|$ measurement comparing different interrogating antenna designs.

To compare the improvement when tuning the interrogating antenna, the original interrogating and sensing antenna was used for the $|S_{11}|$ measurement. The measurement was taken with a fixed distance of 15 mm between the sensing and interrogating antenna. Two measurements were taken, one with the original interrogating antenna tuned such that the reactive component of the interrogating antenna impedance was near zero, and the other measurement were the original interrogating antenna was not tuned. The results are presented in Figure 56.

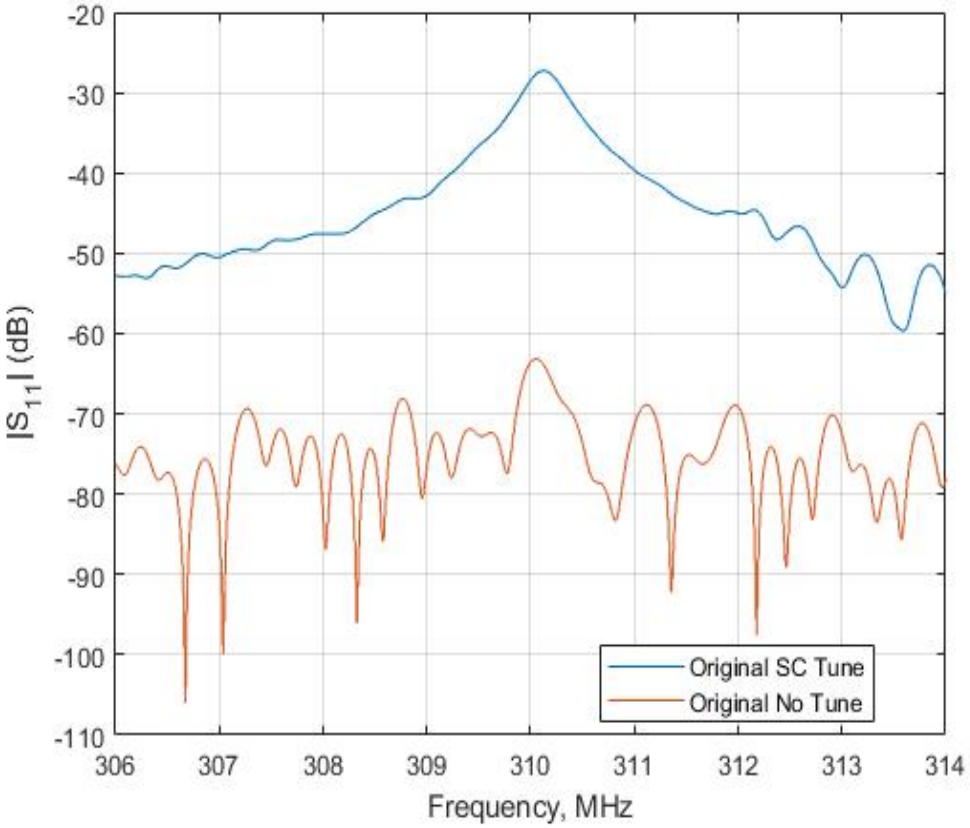

Figure 56: $|S_{11}|$ measurement comparing interrogating antenna tuning vs no tuning.

The results presented indicate that there is a 35.9 dB improvement in the signal strength between the reactive components of the interrogating antenna impedance is removed, compared to the same interrogating antenna without tuning. The same measurement was performed with interrogating antenna 4 and a maximum transmission distance between

the sensing and interrogating antenna was achieved at 26 mm using the same wireless link. These results indicate that the most significant parameter to improve the near-field magnetic field coupling with respect to the interrogating antenna is to remove the reactive component of the antenna impedance.

The final set of measurements conducted was with respect to variation of tuning used on the sensing antenna. A SAW device operating at 323 MHz was used to compare the improvement of the S_{11} time gated response with respect to variation in the tuning network used between the SAW and the sensing antenna. The chosen method for tuning was to use a single pair of capacitive tuning elements in series with the SAW and the sensing antenna. While this does not match the SAW to the sensing antenna, it does however compensate for the sensing antenna's dominant reactive component which mismatches the SAW from the sensing antenna. The impedance was measured for the SAW device used presented in Figure 58.

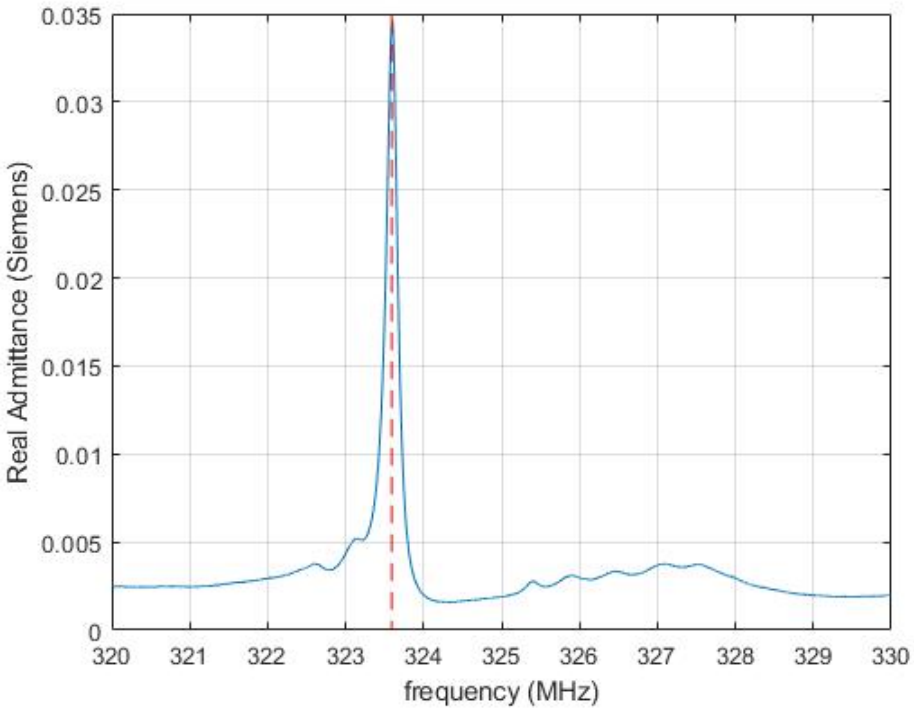
Real Admittance (Siemens)
0.035
0.03
0.025
0.02
0.015
0.01
0.005
0
320
321
322
323
324
325
326
327
328
329
330
frequency (MHz)

(a)

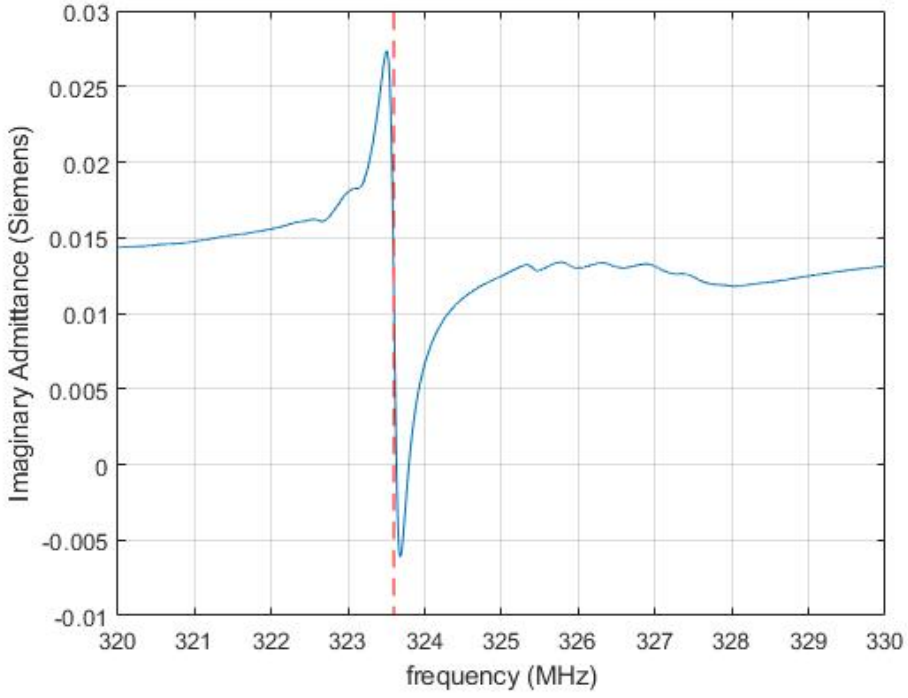
Imaginary Admittance (Siemens)
0.03
0.025
0.02
0.015
0.01
0.005
0
-0.005
-0.01
320
321
322
323
324
325
326
327
328
329
330
frequency (MHz)

(b)

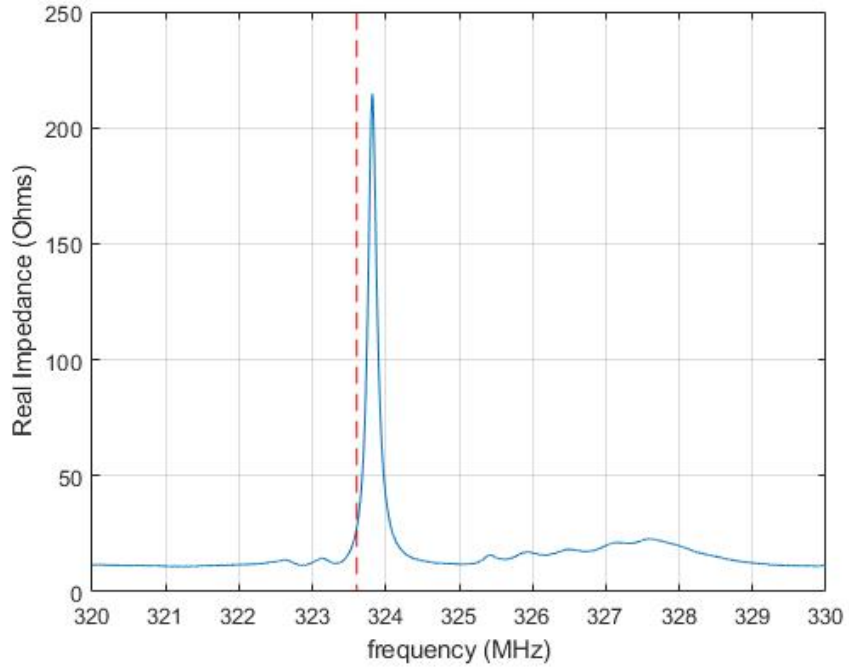

(c)

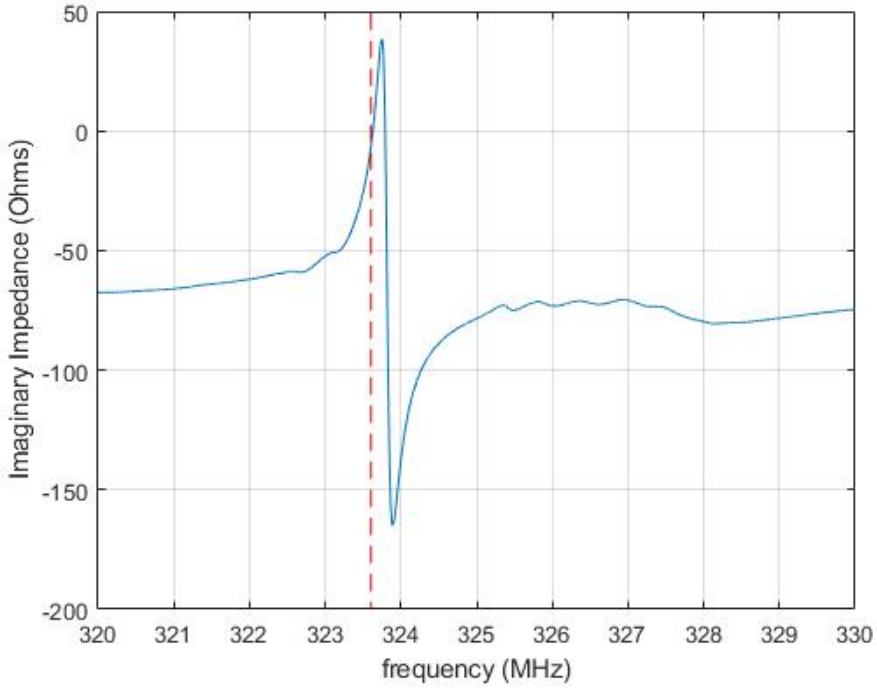

(d)

Figure 57: (a) Measured real admittance of SAW, (b) measured imaginary admittance of SAW, (c) measured real impedance of SAW, (d) measured imaginary impedance of SAW used for sensing antenna 2 measurement.

The resulting impedance at the operation point is 25.7 – j8.15 ohms. After simulation in ADS, the results indicated that the necessary series capacitance- that was required would be on the order of 1.88 pF. Upon testing, it was identified that a measurable signal was not present until 3 elements (or a single pair of tuning elements) were bonded. Previous characterization of the impedance structures indicated a single pair of structures (3 elements) is approximately 2.5 pF. Additional tuning elements were added to the series capacitive structure until the signal began to decrease in strength. The time gated S_{11} measurement comparing the improvement of the response with respect to the baseline. Baseline in Figure 58 represents the new sensing antenna without a series capacitance. This was achieved by replacing the series capacitance element with a conductor, which when implemented was a 1 mil platinum bond wire.

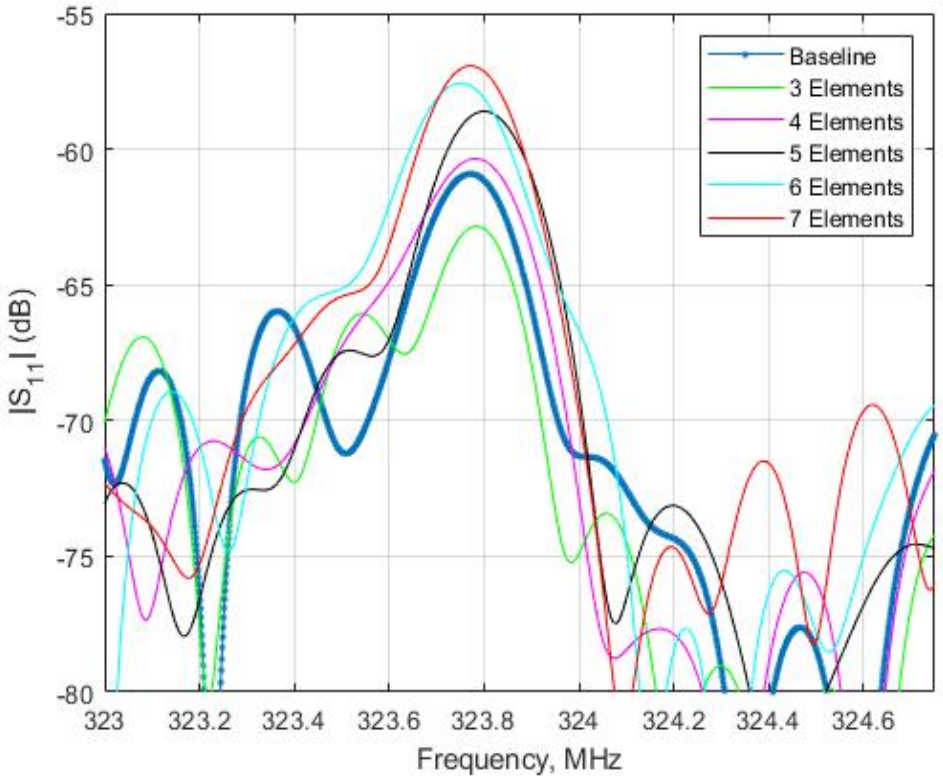

Figure 58: Time gated S_{11} measurement as series capacitance was varied.

Note that the results were measured with respect to a fixed height such that changes in distance did not impact the measurement. The proximity of the sensing antenna with respect to the interrogating antenna was 15 mm. To best see the correlation of the results a plot representing the number of tuning elements which were bonded with respect to the peak amplitude of the signal was produced. These results are presented in Figure 59.

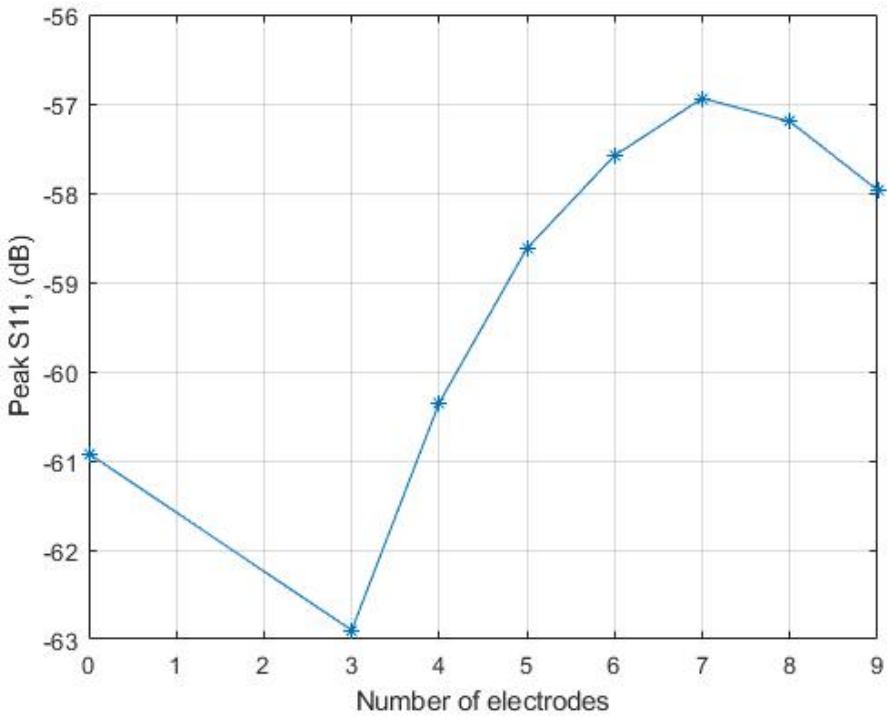

Figure 59: Peak amplitude of S_{11} with respect to number of electrodes used.

The results indicate that the use of series capacitance improved the signal strength by 4 dB.

CHAPTER IV

DISCUSSION

The results indicate that the proposed investigations for optimization of the interrogating antenna design for a fixed footprint and tuning for the sensing and interrogating antenna by a total improvement of 45.9 dB . The results for the case of the sensing antenna indicate that by using the optimum value for series capacitance between the SAW and sensing antenna, the signal improved by 4 dB between the baseline measurement of the new sensing antenna with no series capacitive tuning. When considering optimization of the design for the interrogating antenna, interrogating antenna 4 provides the best selection for interrogating antenna design. The improvement measured comparing between each interrogating antenna designed resulted in 6 dB improvement without tuning. Simulated results indicate tuning improves magnetic field magnitude by 36 dB while matching increases power by 136%, and current by 7.4% compared to the tuned case. The most significant improvement was measured when comparing the tuning of the previous state-of-the-art interrogating antenna tuned with a series capacitance and not tuned, which provide a 36 dB improvement in measured peak $|S_{11}|$.

The characterization of the impedance for the sensing and interrogating antenna indicates that the series resistance of the antennas cannot be neglected. The characterization of the impedance also indicated that the loss in the Inconel lines used for high temperature

wireless communication is 4 dB/m. High temperature lines are not appropriate for use to characterize the impedance of antenna designs.

It was known previously however that tuning of the interrogating antenna improves the signal strength of the wireless link without quantification. Results have proven that the method of "short circuit tuning" was not correct, but rather that the reactive component of the interrogating antenna's impedance is compensated by tuning via use of a series capacitance. This provides the desired improvement in signal strength. While the tuning of the interrogating antenna was a continuation of previous research, the total improvement measured with new interrogating antenna designs and tuning of the sensing antenna using a series capacitance improved signal measurement by a total of 10 dB. A total 46 dB improvement in signal strength and maximum 26 mm transmission distance were achieved will be made available to MAL members, as well as Environetix (a spinoff SAW company which works in collaboration with the University of Maine).

CHAPTER V

RECOMMENDATIONS FOR FUTURE WORK

There are numerous areas where additional research could be conducted about the proposed wireless link. The first of investigation would be to perform the transmission experiments with a high temperature system. The measurements that were conducted used lines that were functional at room temperatures, but not functional up to 1000 °C. Reproduction of the results with the use of Inconel cables and an Inconel fixture to hold the interrogating antenna would indicate how the change in the coaxial cable setup fixtures influences the system measurement.

Following this investigation, the wireless link could also be measured at high temperatures. Two comparisons could be conducted. The first would be to consider the comparison of how the signal strength changes with respect to change in temperature, the second being how the sensing and interrogating antenna impedance changes with temperature. By determining whether the change in temperature significantly changes the impedance, and if so, how this effects the signal strength, it would indicate the feasibility of the system improvements at high temperature.

The simulation results for the interrogating and sensing antenna both indicate that by matching, the maximum current flows through the antenna and maximum power is delivered to the SAW or VNA respectively. For the case of the interrogating antenna, the

impedances for matching were difficult to implement, while ADS results indicated that the sensing antenna could be matched with respect to the SAW. Matching would require more tuning elements than which are present on the new sensing antenna design developed. By expanding the available tuning elements available on the sensing antenna, a larger number of tuning elements could be used to match the SAW device to the sensing antenna.

The final area in which future work could be conducted would be to increase the size of the interrogating and sensing antenna. By applying the same design principles for maximizing the inductance while avoiding self-resonance, it would be useful to determine how the increase in antenna footprint correlates with increase in time gated S_{11}. Quantification of the maximum footprint for both the sensing and interrogating antenna and development of new designs for these constraints would indicate the absolute limitations for transmission distance.

REFERENCES

[1] “RF Wireless World,” modulation index in AM and FM | What is modulation index. [Online]. Available: http://www.rfwireless-world.com/Articles/ceramic-coaxial-resonator-vs-dielectric-resonator-vs-crystal-resonator-vs-ceramic-resonator-vs-SAW-resonator-vs-YIG-resonator.html. [Accessed: 07-Mar-2019].

[2] Priya, R & Venkatesan, Thirumal & M Pandya, Haresh. (2016). A Comparison of Surface Acoustic Wave (SAW) Delay Line Modelling Techniques for Sensor Applications. Journal of Environmental Nanotechnology. 5. 42-47. 10.13074/jent.2016.06.162193.

[3] F. T. Ulaby and U. Ravaioli, Fundamentals of applied electromagnetics. Harlow: Pearson, 2015.

[4] P. R. Franchi, “US Patent 4998112,” 05-Mar-1991.

[5] “How To Create Standing Waves,” How to create standing waves. [Online]. Available: http://calgarynext.com/scotland/how-to-create-standing-waves.php.[Accessed: 04-Apr-2019].

[6] Environetix Internal Documentation, 2018.

[7] D. M. Pozar, Microwave engineering. New Delhi: Wiley India, 2017.

APPENDICES

APPENDIX A: HFSS SELF RESONANCE SIMULATION RESULTS

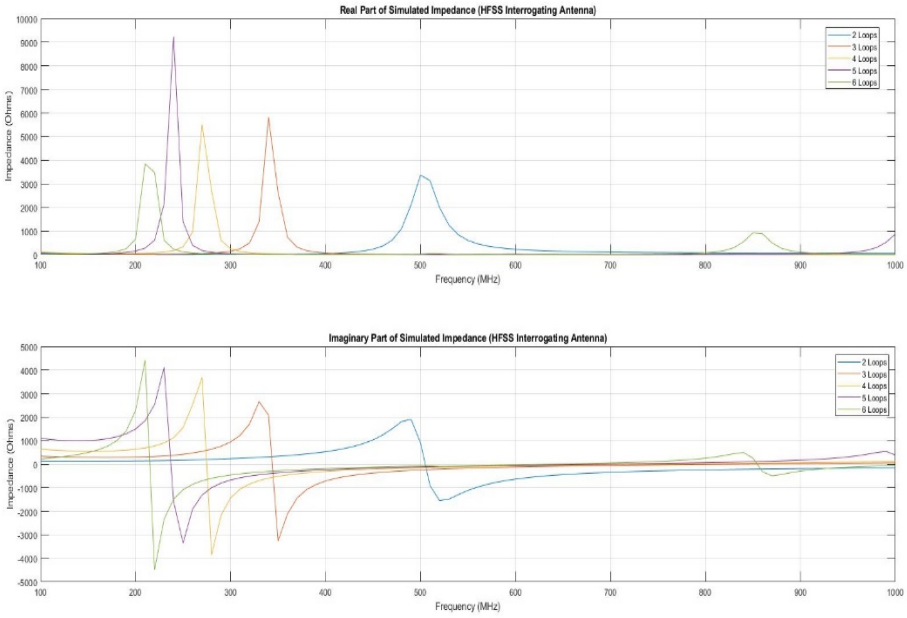

Figure 60: Interrogating antenna resonance curves (2 Loops).

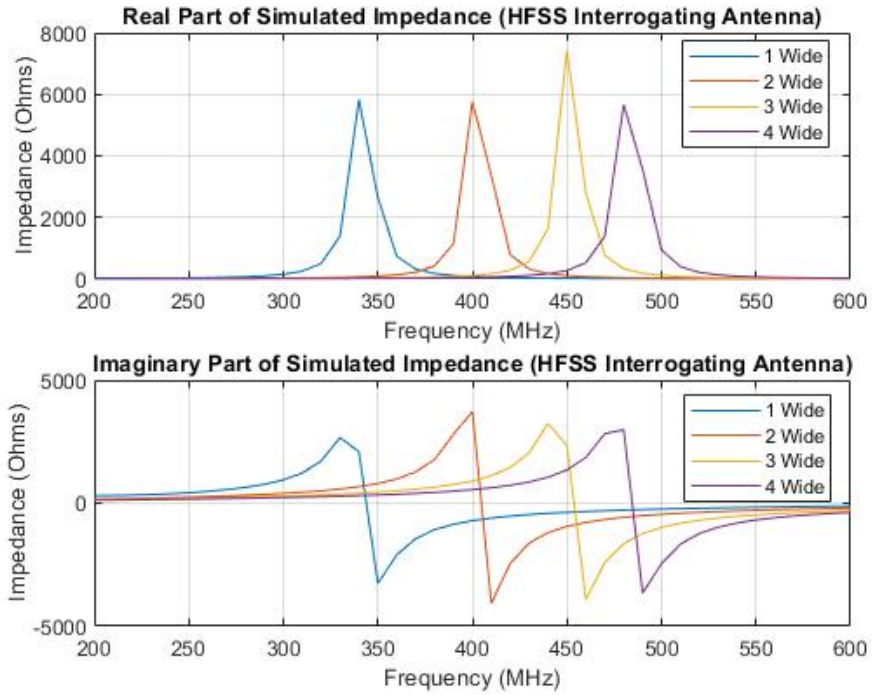

Figure 61: Interrogating antenna resonance curves (3 Loops).

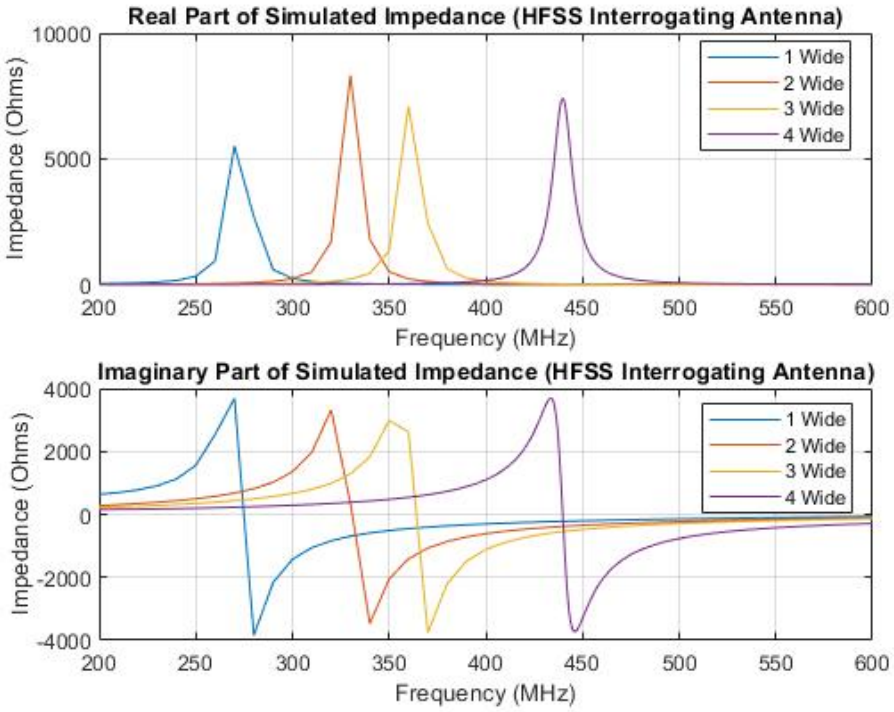

Figure 62: Interrogating antenna resonance curves (4 Loops).

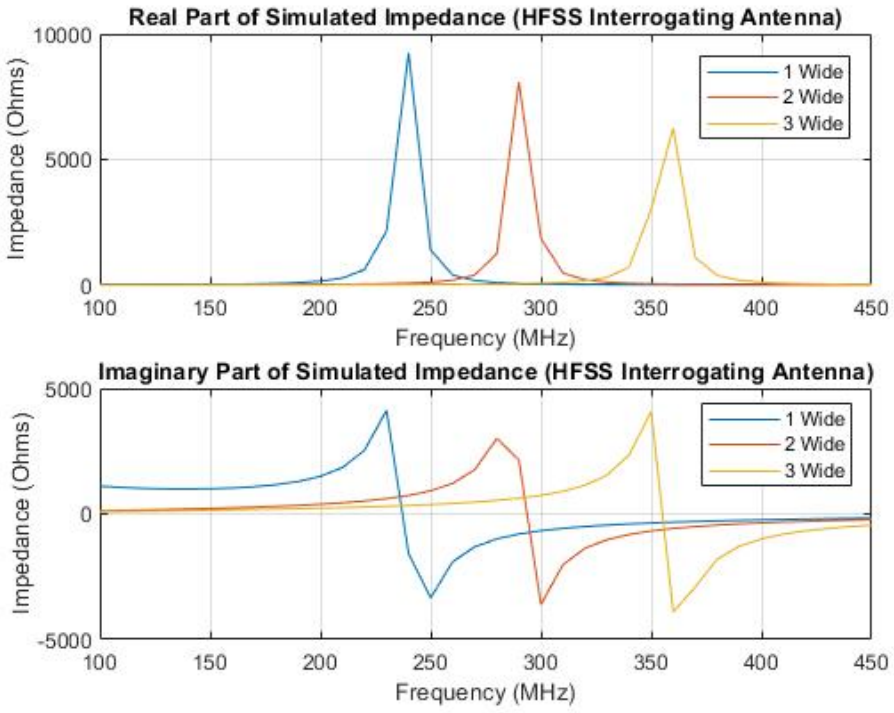

Figure 63: Interrogating antenna resonance curves (5 Loops).

Table 7: Interrogating antenna resonance frequencies and admittances @ 334 MHz

Interrogating Antenna		
2 Loops (Spacings)	Resonance Frequency	Admittance (siemens)
1 W	500 MHz	.000186-j.003165
3 Loops (Spacings)	Resonance Frequency	Admittance (siemens)
1 W	340 MHz	.0001521-j.000005453
2 W	400 MHz	.0001419-j.001478
3 W	450 MHz	.0001608-j.002447
4 W	480 MHz	.000193-j.003236
4 Loops (Spacings)	Resonance Frequency	Admittance (siemens)
1 W	270 MHz	.0001196 + j.001687
2 W	330 MHz	.0001179+j.0002268
3 W	360 MHz	.0001291-j.0005144
4 W	440 MHz	.0001799-j.002491
5 Loops (Spacings)	Resonance Frequency	Admittance (siemens)
1 W	240 MHz	.0001193 +j.002504
2 W	290 MHz	.0001092+j.001215
3 W	360 MHz	.0001131-j.00034891

Table 8: Sensing antenna resonance frequencies and admittance @ 334 MHz

Sensing Antenna (Loops)	Resonance Frequency	Admittance (siemens)
2 Loops	617 MHz	.0003613 - j.006444
3 Loops	546 MHz	.0003793 - j.004704

APPENDIX B: HFSS TUNING AND MAGNETIC FIELD MAGNITUDE SIMULATION RESULTS

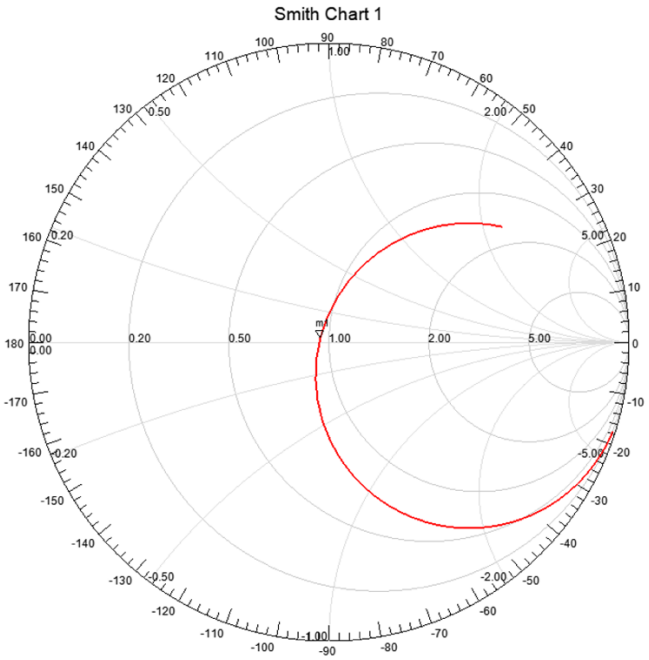

Figure 64: Tuned original interrogating antenna Smith chart simulation result.

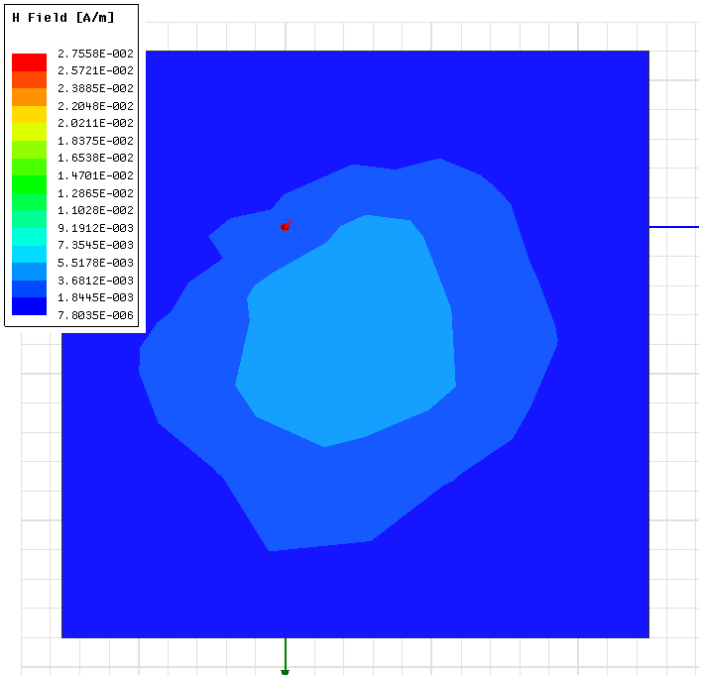

Figure 65: Tuned original interrogating antenna magnetic field magnitude simulation result.

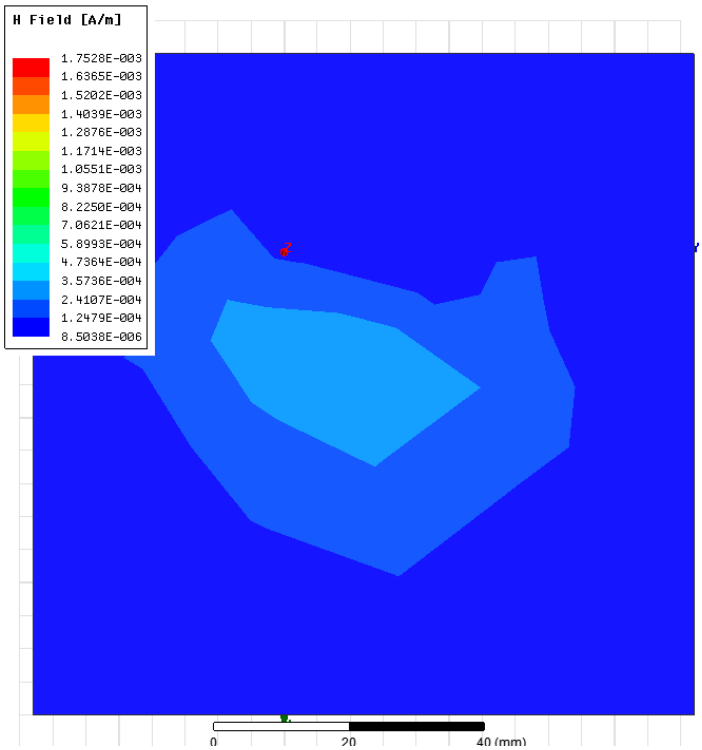

Figure 66: No tune original interrogating antenna magnetic field magnitude simulation result.

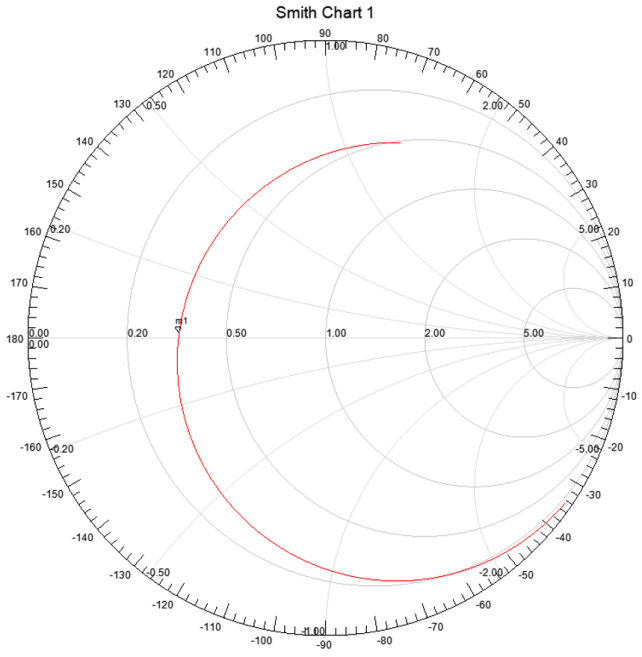

Figure 67: Tuned interrogating antenna 2 Smith chart simulation result.

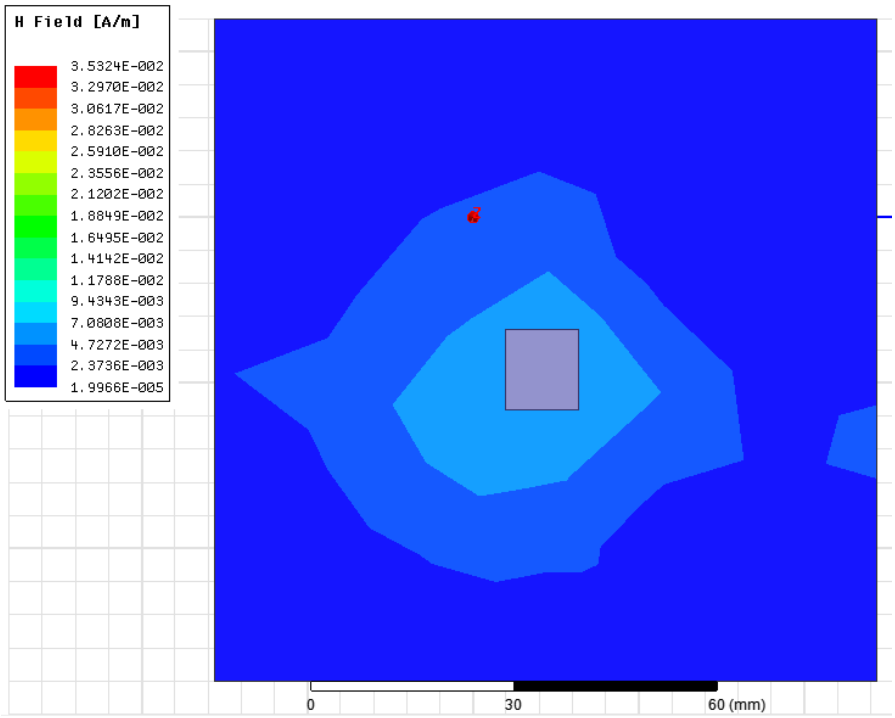

Figure 68: Tuned interrogating antenna 2 magnetic field magnitude simulation result.

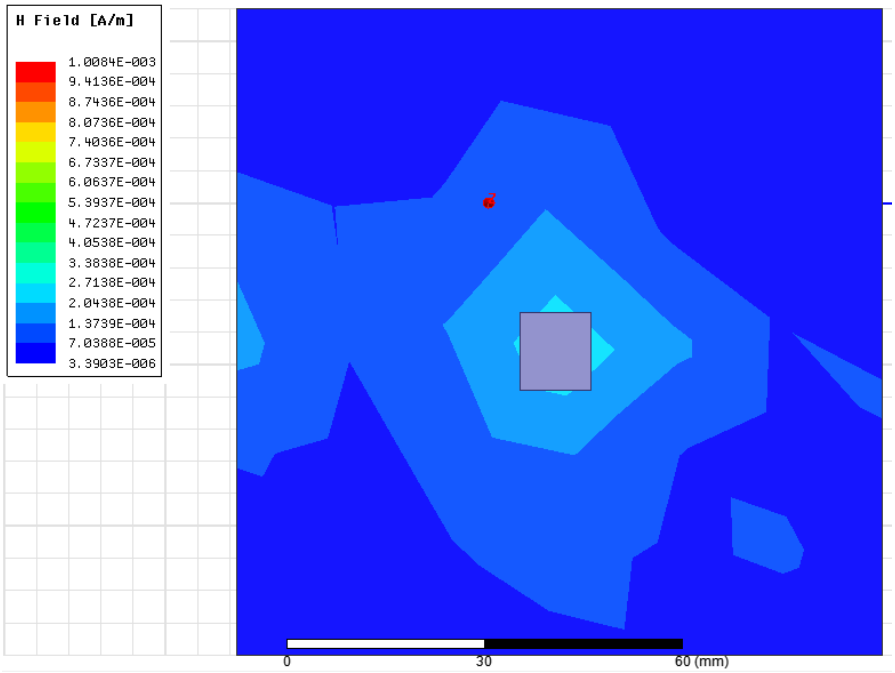

Figure 69: No tune interrogating antenna 2 magnetic field magnitude simulation result.

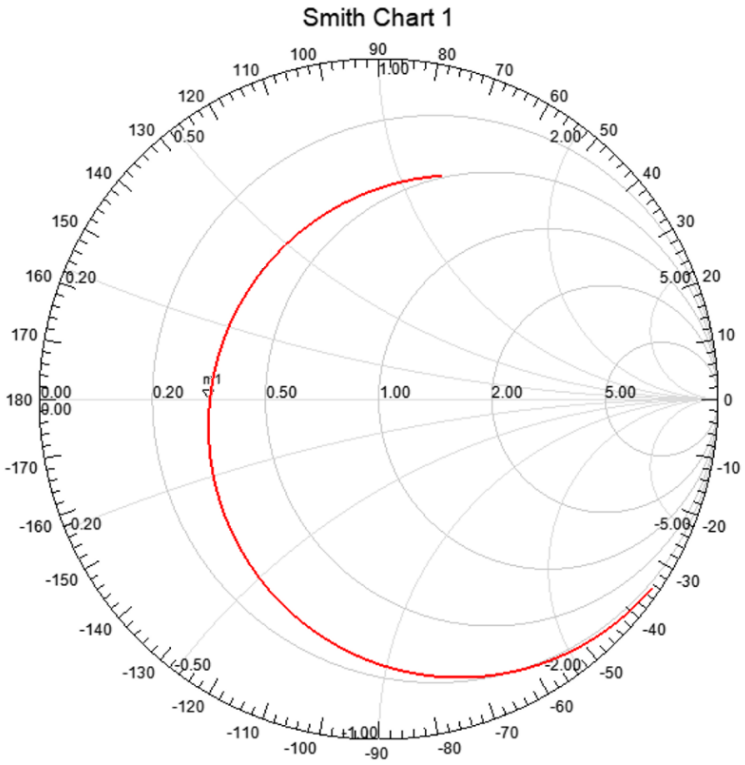

Figure 70: Tuned interrogating antenna 3 Smith chart simulation result.

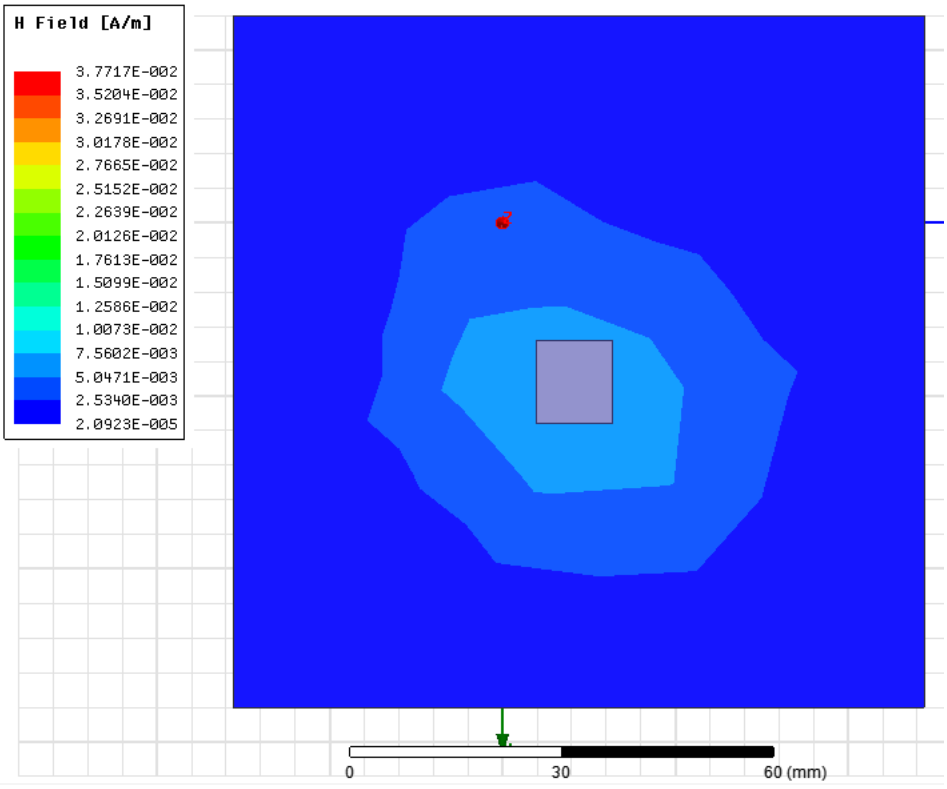

Figure 71: Tuned interrogating antenna 3 magnetic field magnitude simulation result.

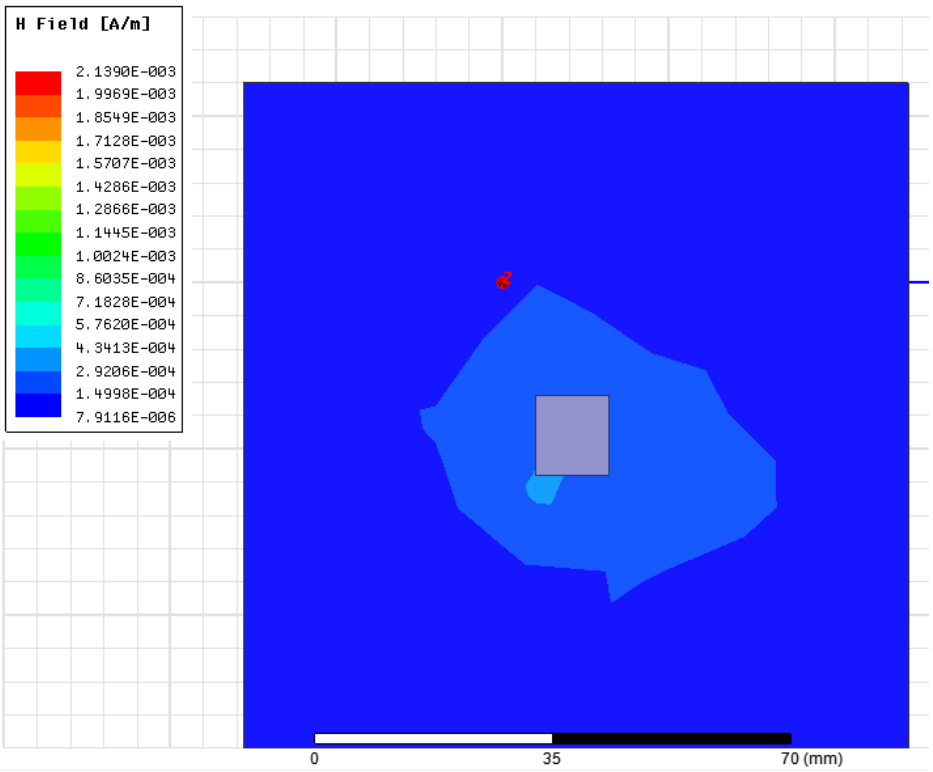

Figure 72: No tune interrogating antenna 3 magnetic field magnitude simulation result.

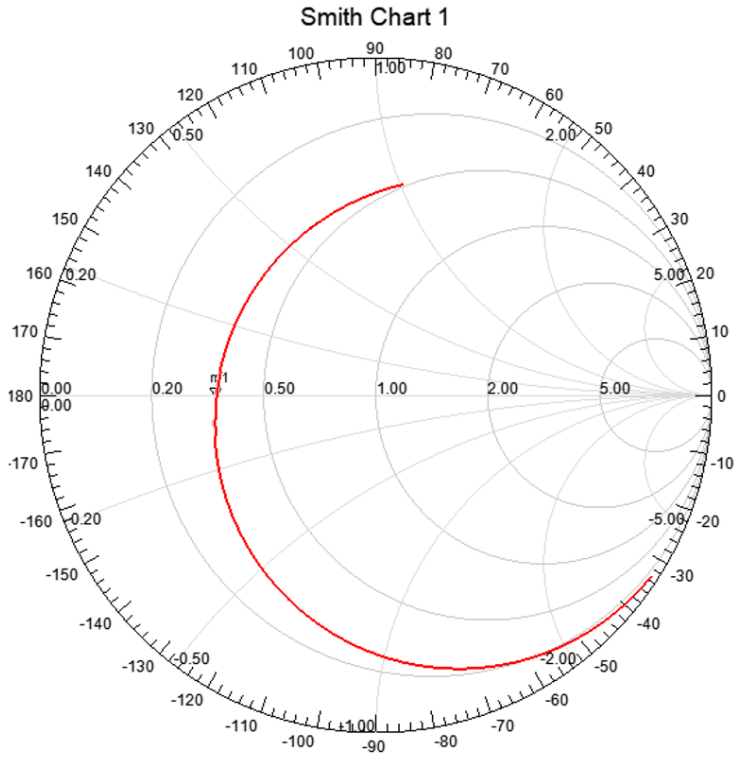

Figure 73: Tuned interrogating antenna 4 Smith chart simulation result.

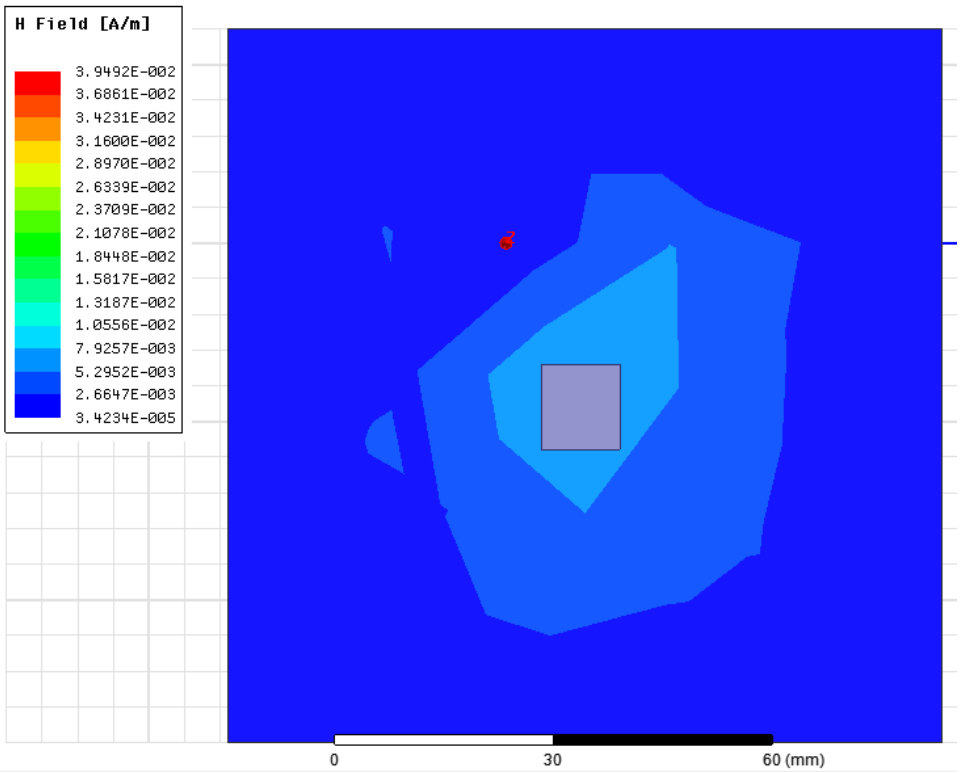

Figure 74: Tuned interrogating antenna 4 magnetic field magnitude simulation result.

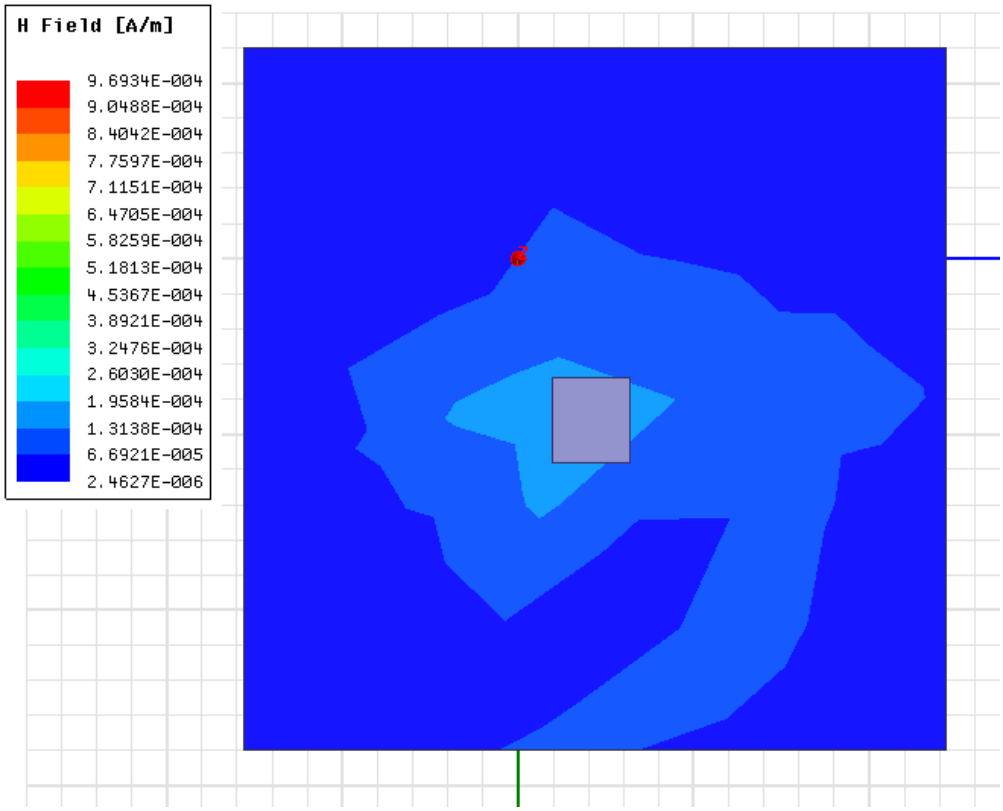

Figure 75: No tune interrogating antenna 4 antenna magnetic field magnitude simulation result.

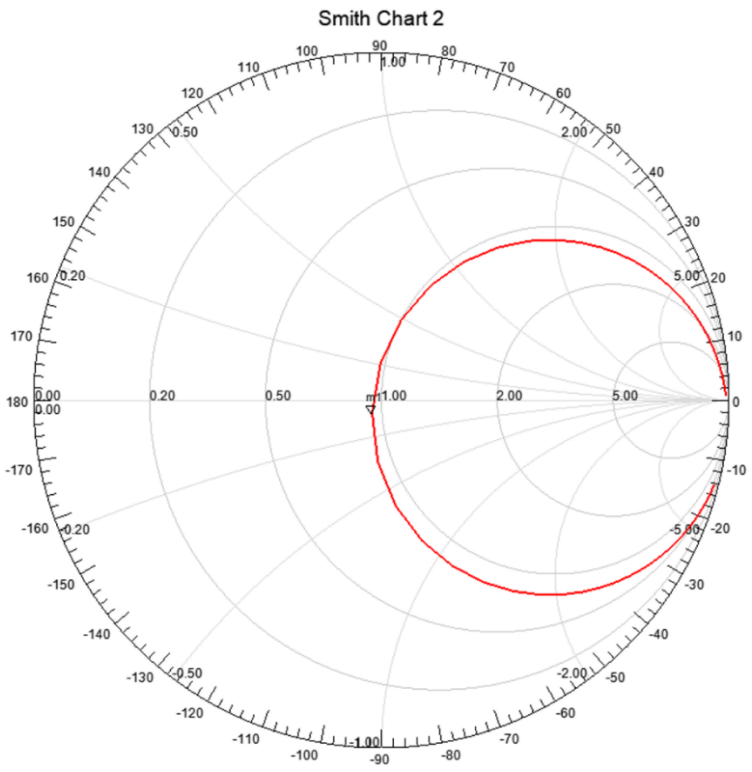

Figure 76: Tuned new sensing antenna Smith chart simulation result.

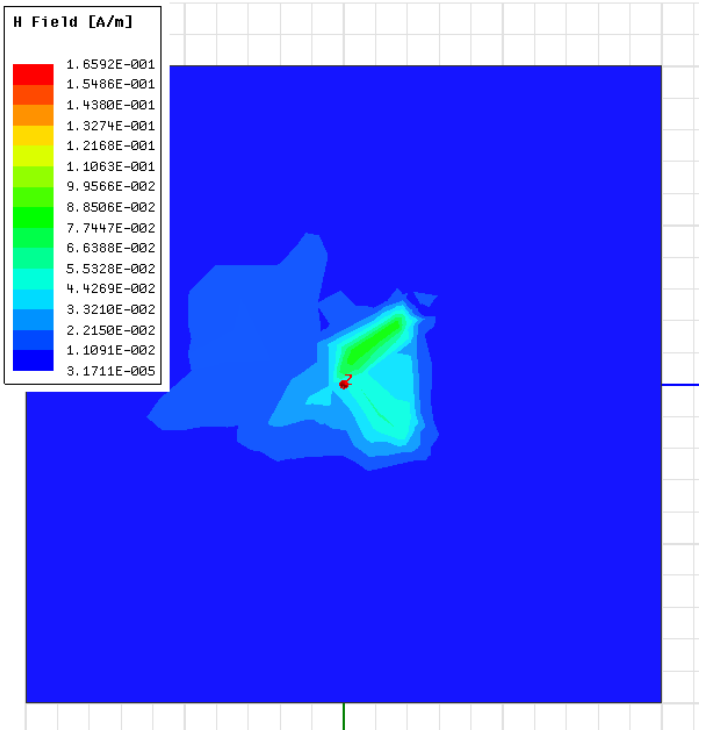

Figure 77: Tuned new sensing antenna magnetic field magnitude simulation result.

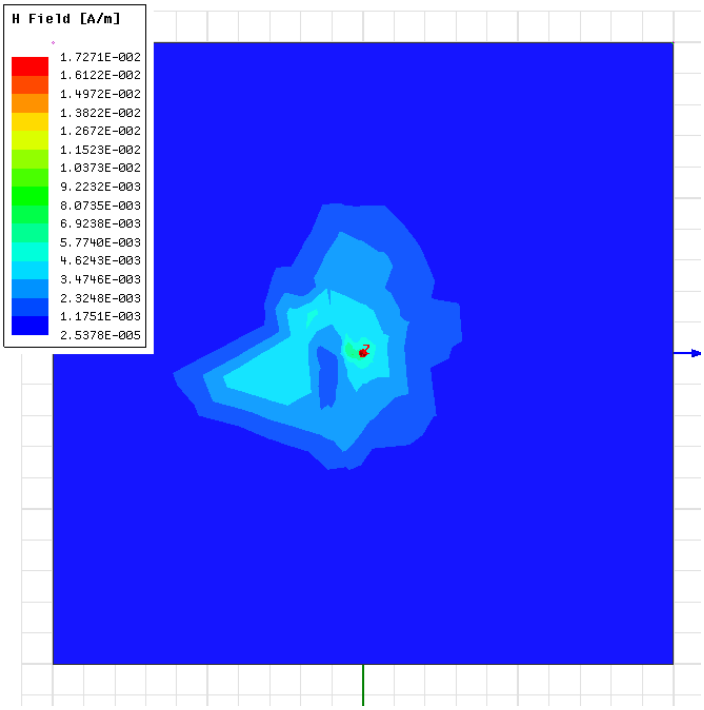

Figure 78: No tune new sensing antenna magnetic field magnitude simulation result.

APPENDIX C: ADS SERIES CAPACITANCE TUNING INTERROGATING ANTENNA SIMULATION RESULTS

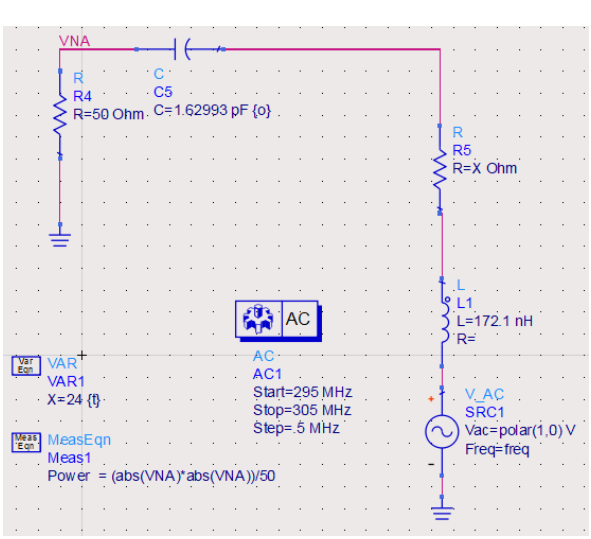

(a)

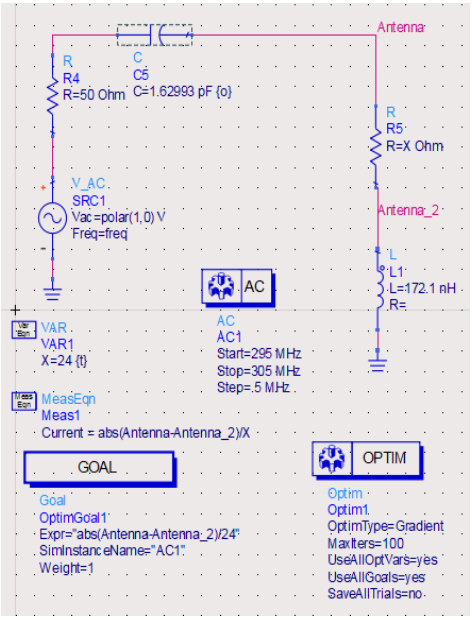

(b)

Figure 79: (a) Original interrogating antenna series capacitance tuning schematic (VNA source), (b) original interrogating antenna series capacitance tuning schematic (IA source).

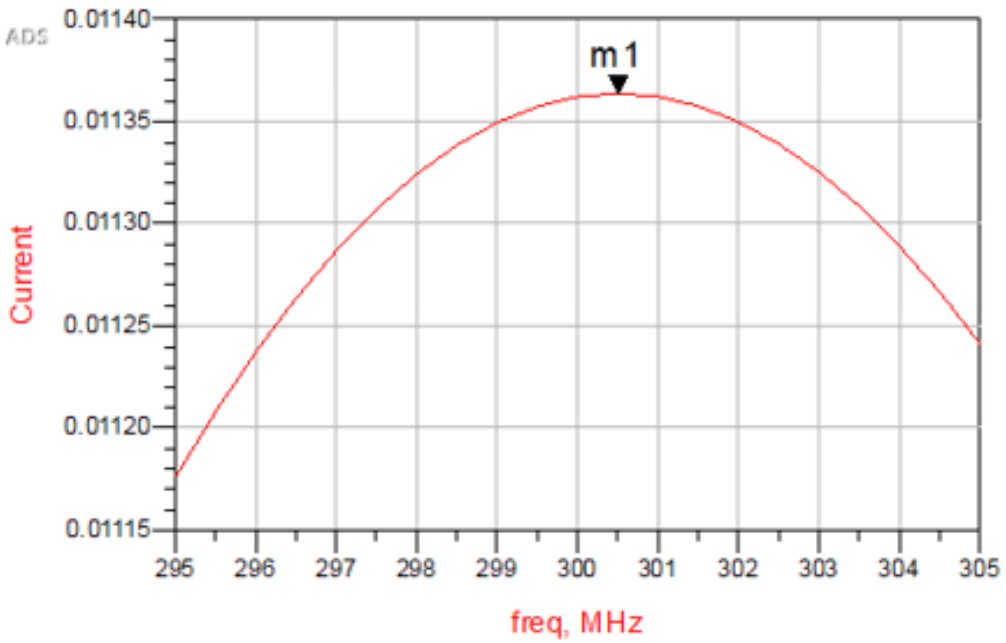

Figure 80: Original interrogating antenna series capacitance tuning (current simulation, VNA source).

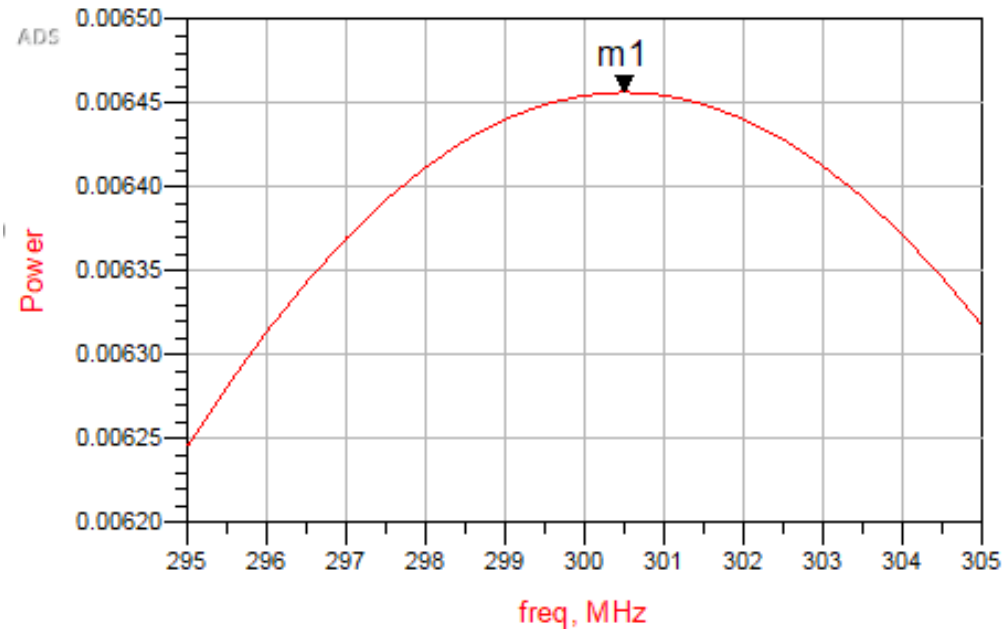

Figure 81: Original interrogating antenna series capacitance tuning (power simulation, IA source).

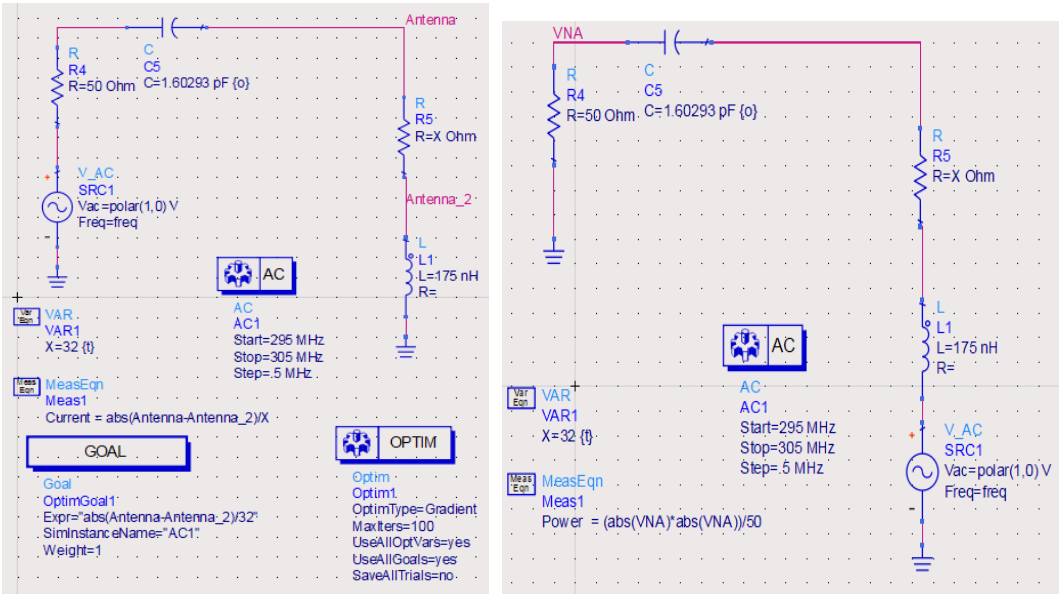

(a) (b)

Figure 82: (a) Interrogating antenna 2 series capacitance tuning schematic (VNA source), (b) interrogating antenna 2 series capacitance tuning schematic (IA Source).

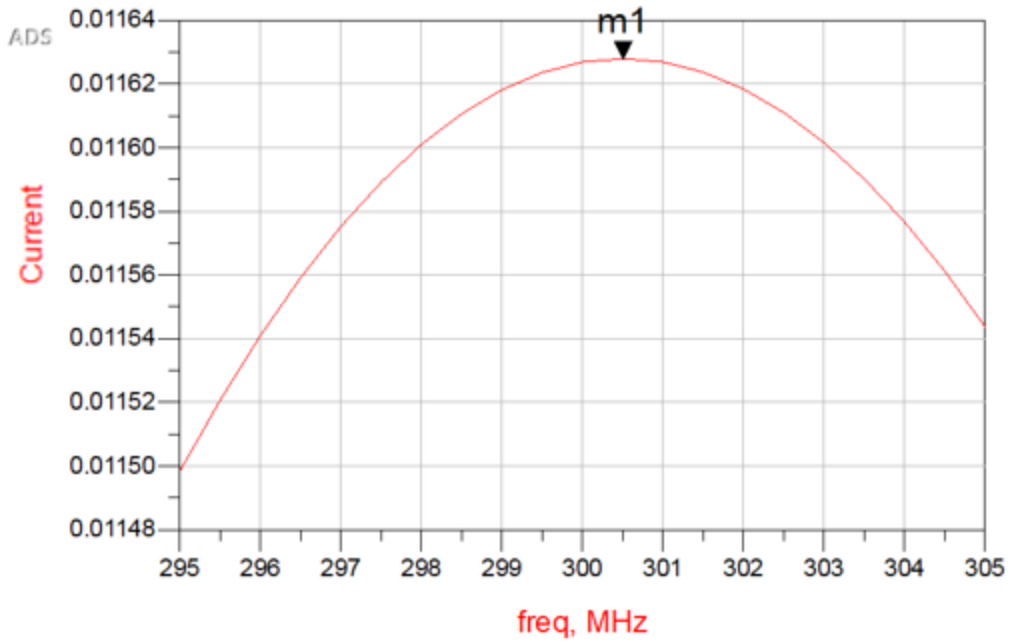

Figure 83: Interrogating antenna 2 series capacitance tuning (current simulation, VNA source).

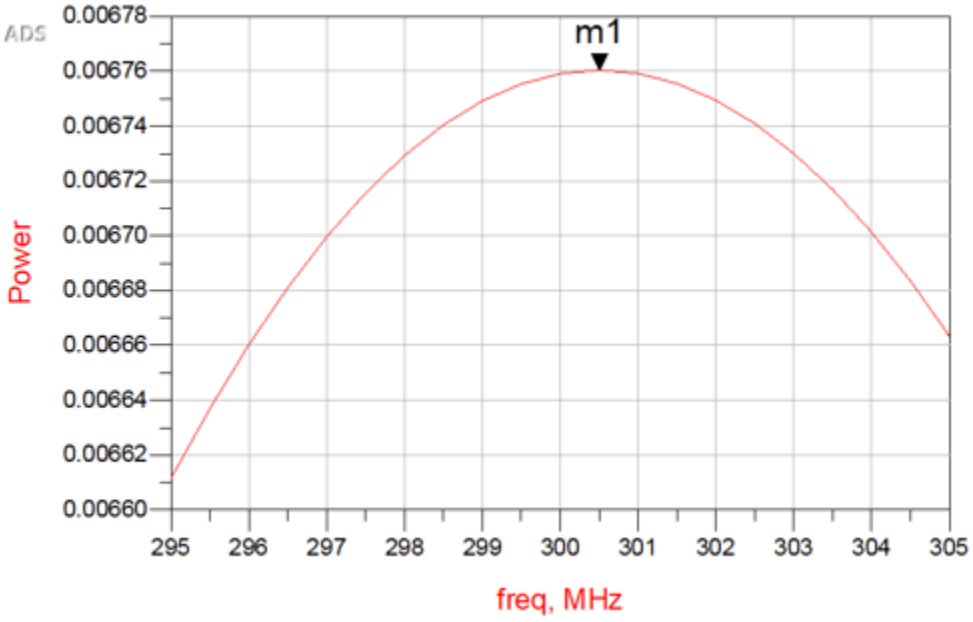

Figure 84: Interrogating antenna 2 series capacitance tuning (power simulation, IA source).

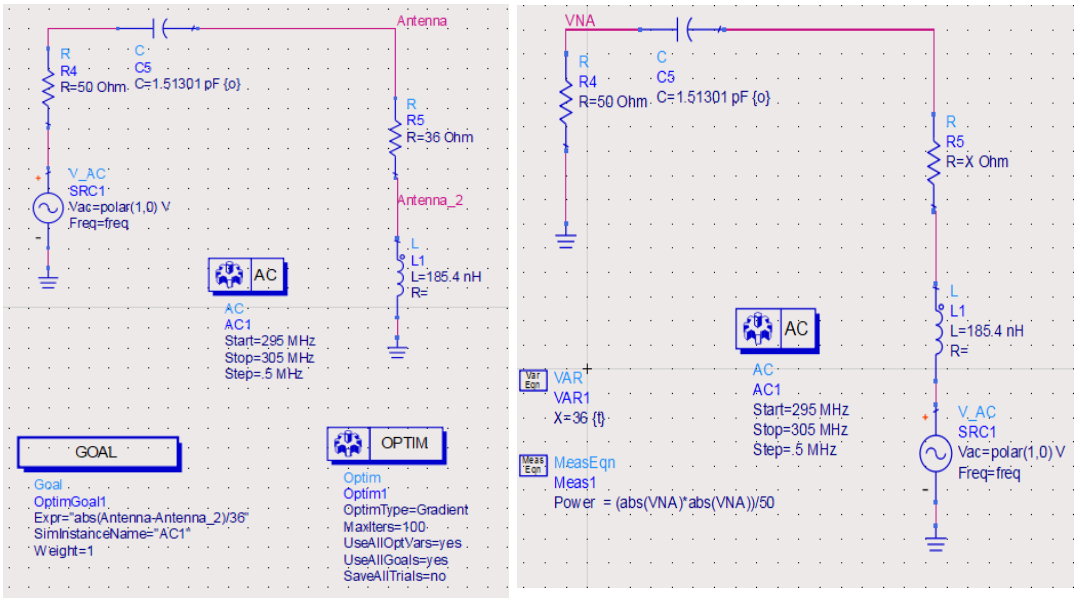

(a)
(b)

Figure 85: (a) Interrogating antenna 3 series capacitance tuning schematic (VNA source), (b) Interrogating antenna 3 series capacitance tuning schematic (IA source).

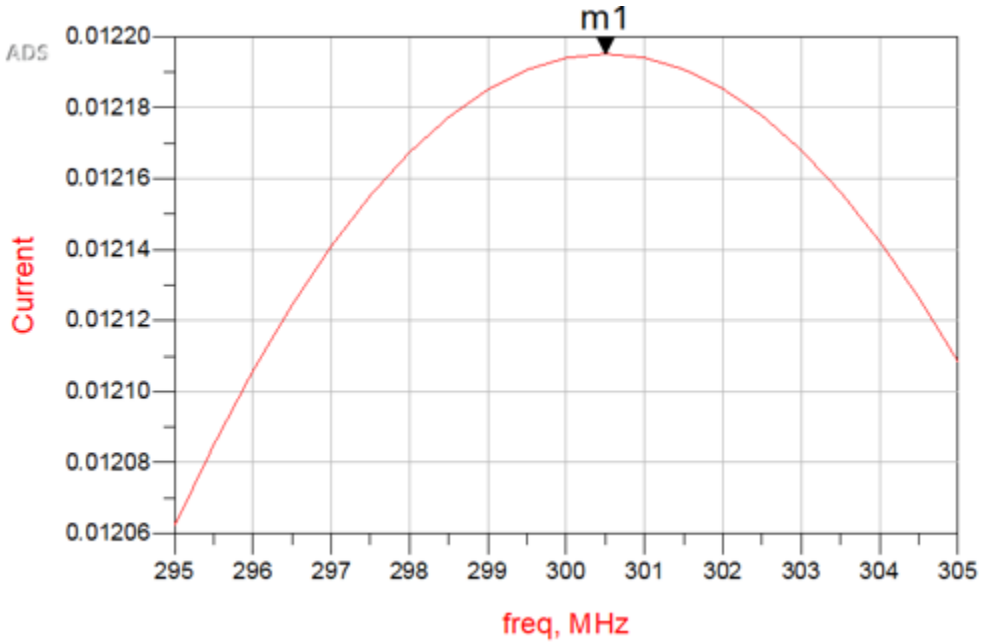

Figure 86: Interrogating antenna 3 series capacitance tuning (current simulation, VNA source).

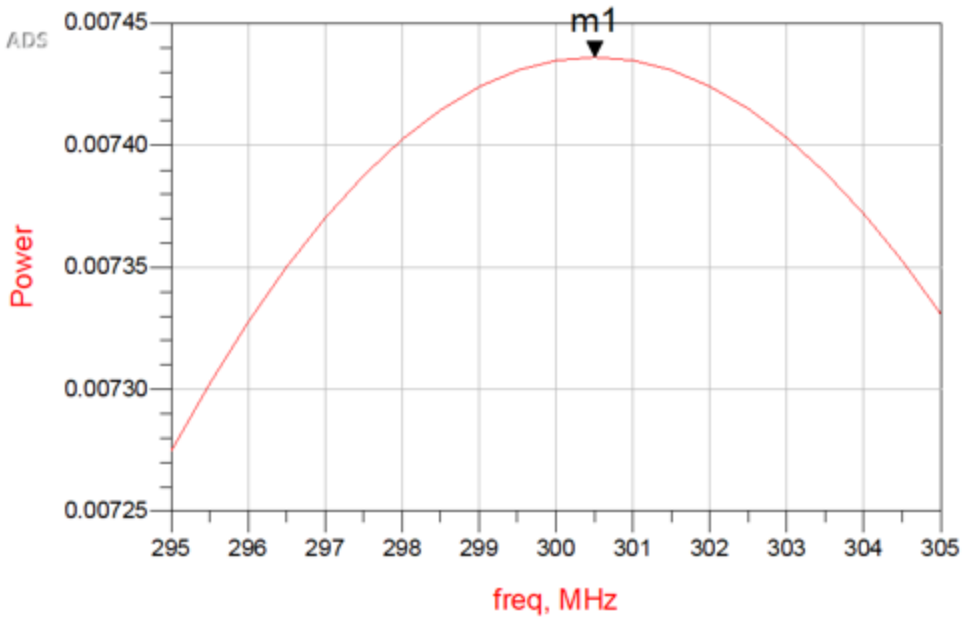

Figure 87: Interrogating antenna 3 series capacitance tuning (power simulation, IA source).

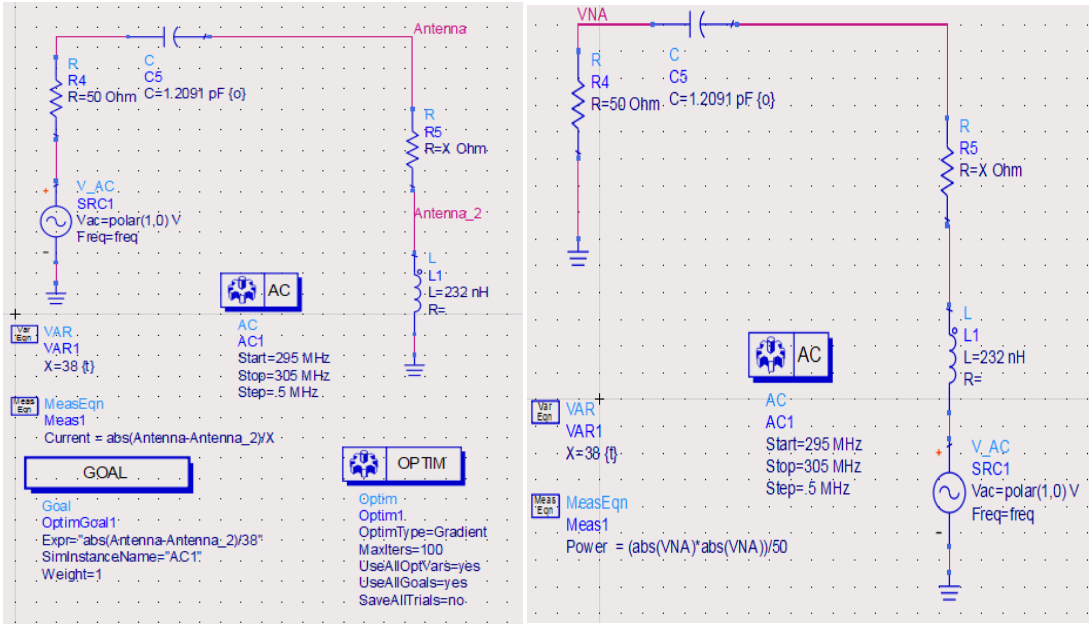

(a) (b)

Figure 88: (a) Interrogating antenna 4 series capacitance tuning schematic (VNA Source), (b) interrogating antenna 4 series capacitance tuning schematic (IA Source).

Figure 89: Interrogating antenna 4 series capacitance tuning (current simulation, VNA source).

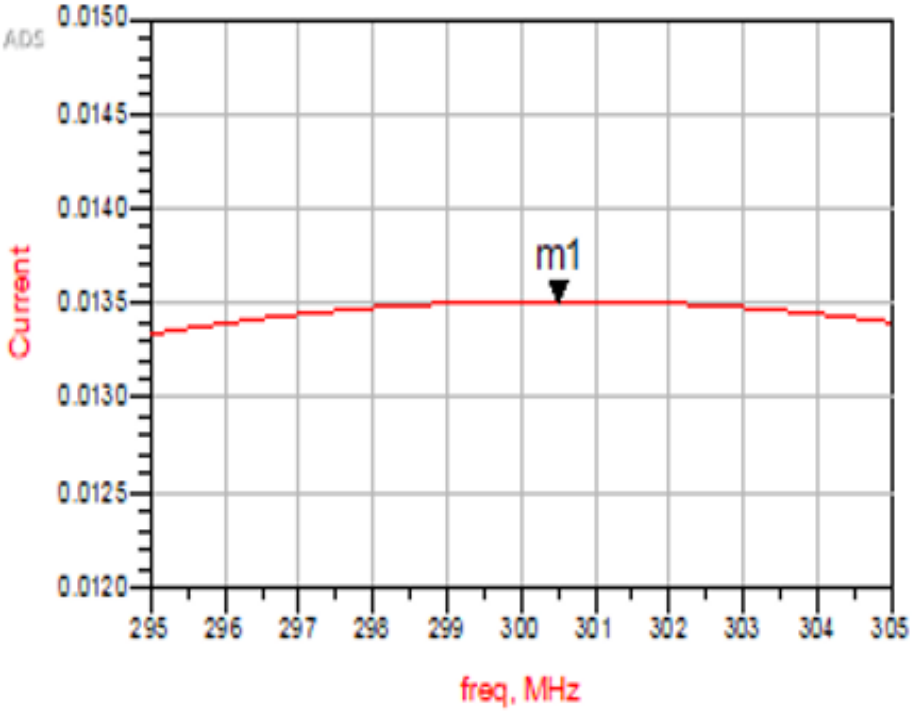

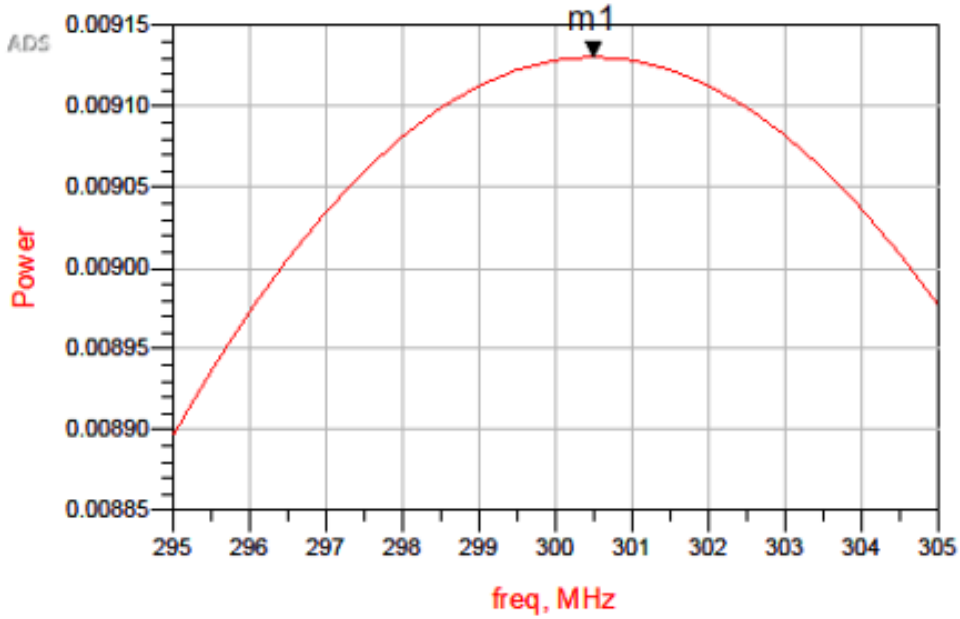

Figure 90: Interrogating antenna 4 series capacitance tuning (power simulation, IA source).

APPENDIX D: ADS MATCHING INTERROGATING ANTENNA SIMULATION RESULTS

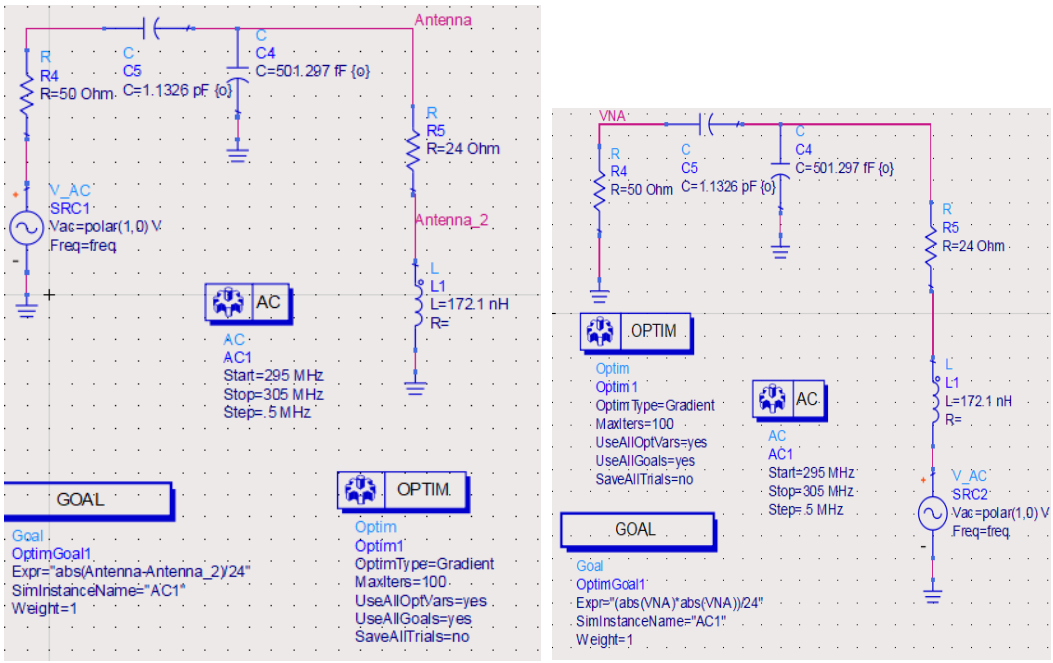

(a) (b)

Figure 91: (a) Original interrogating antenna matched schematic (VNA source), (b) original interrogating antenna matched schematic (IA source).

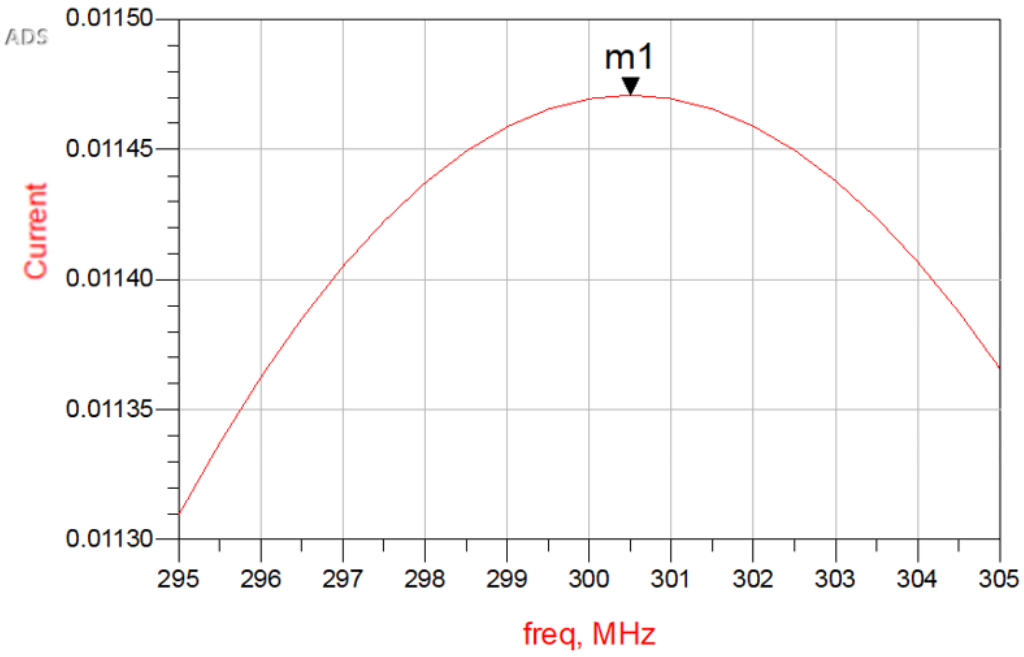

Figure 92: Original interrogating antenna matched (current simulation, VNA source).

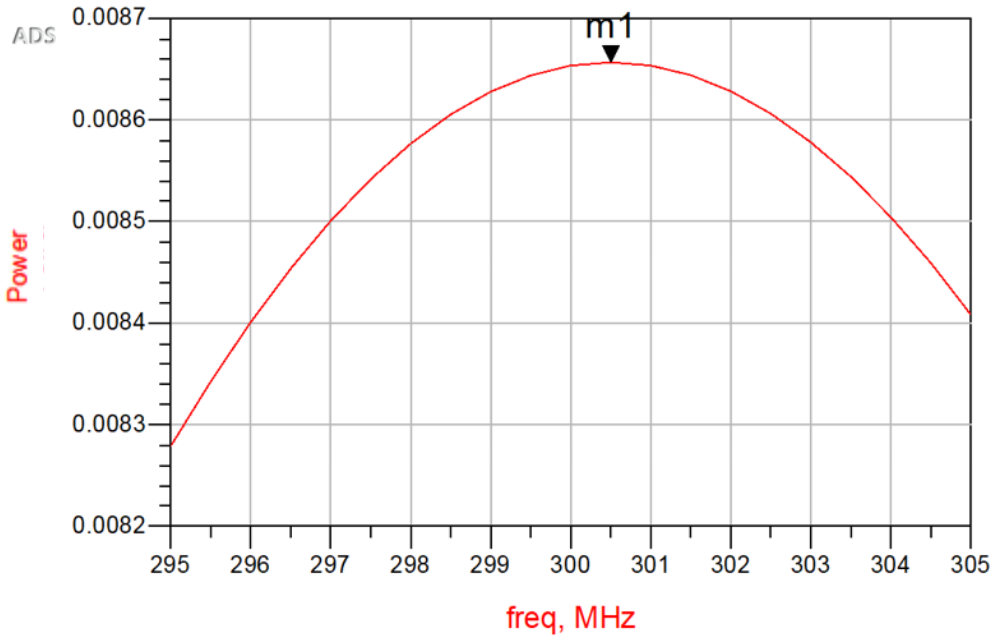

Figure 93: Original interrogating antenna matched (power simulation, IA source).

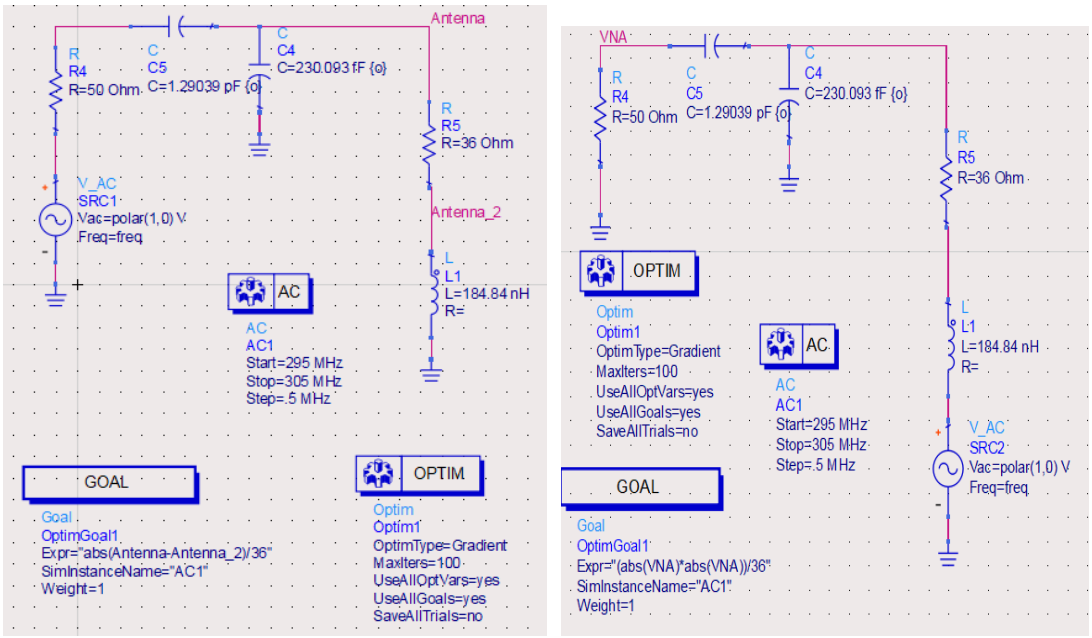

(a) (b)

Figure 94: (a) Interrogating antenna 2 antenna matched schematic (VNA source), (b) interrogating antenna 2 antenna matched schematic (IA source).

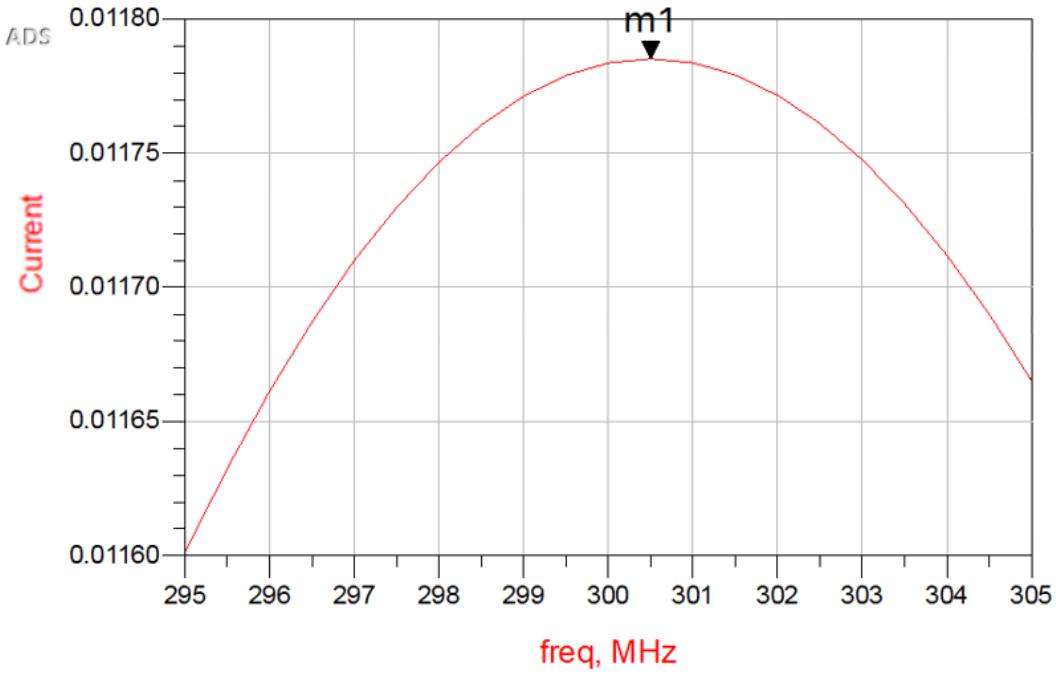

Figure 95: Interrogating antenna 2 matched (current simulation, VNA source).

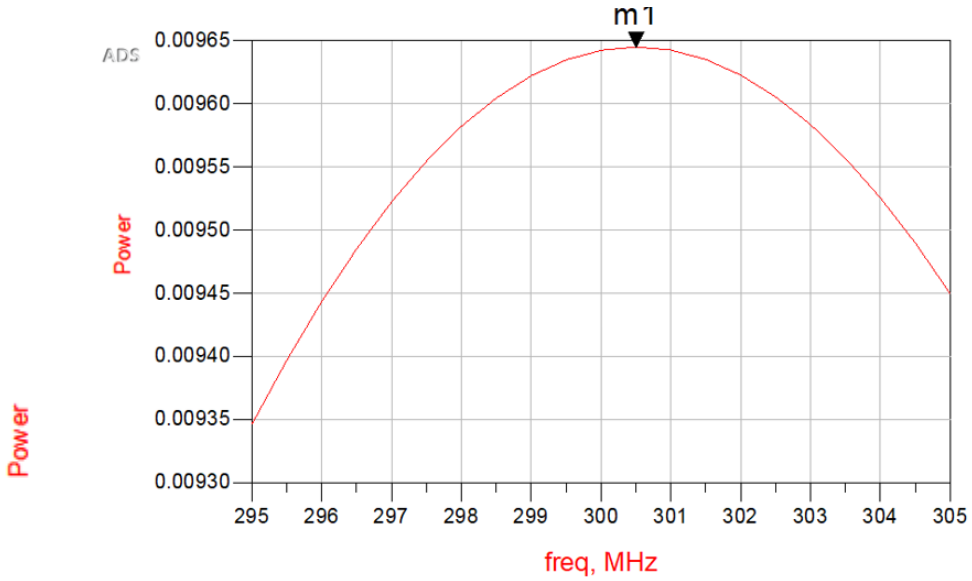

Figure 96: Interrogating antenna 2 antenna matched (power simulation, IA source).

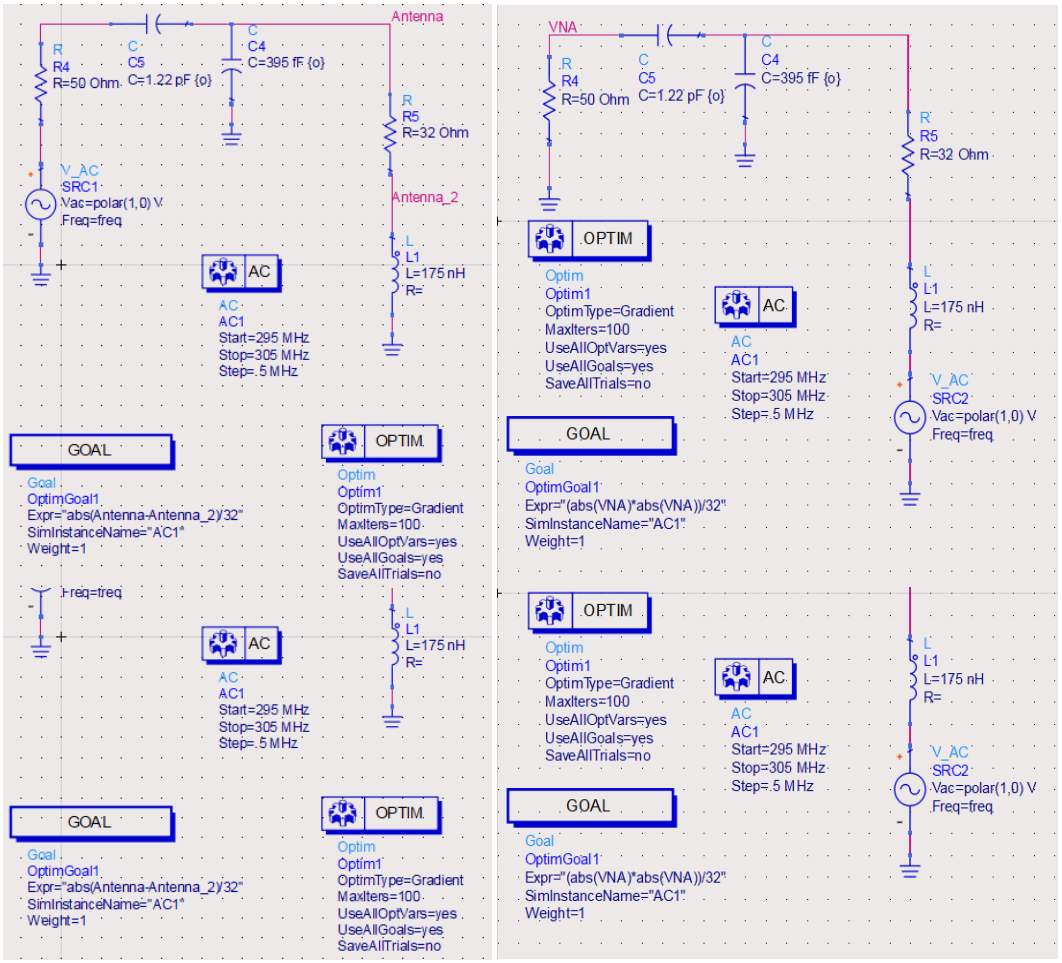

(a) (b)

Figure 97: (a) Interrogating antenna 3 matched schematic (VNA source), (b) interrogating antenna 3 antenna matched schematic (IA source).

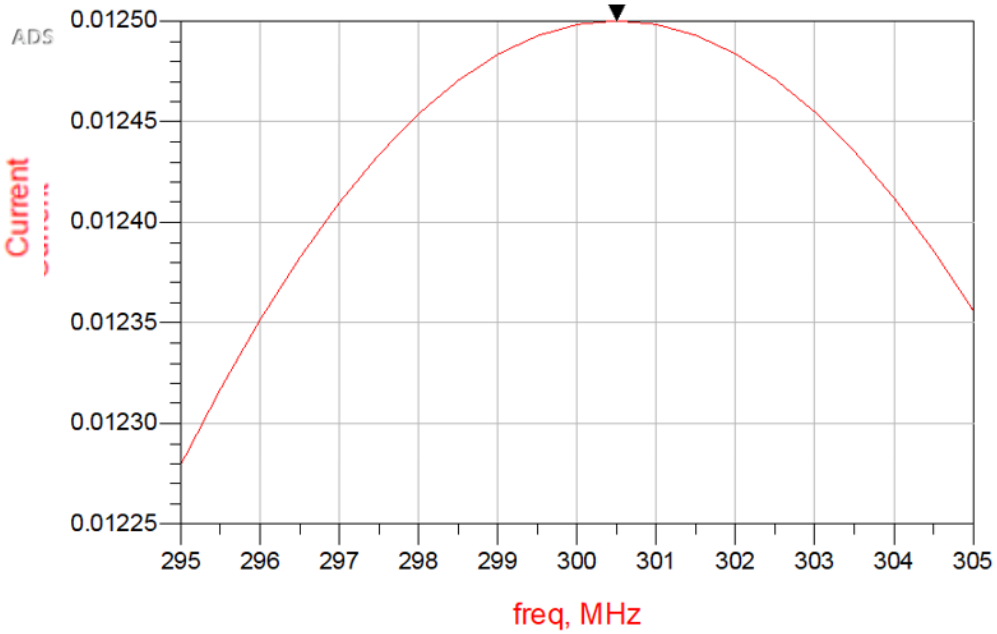

Figure 98: Interrogating antenna 3 matched (current simulation, VNA source).

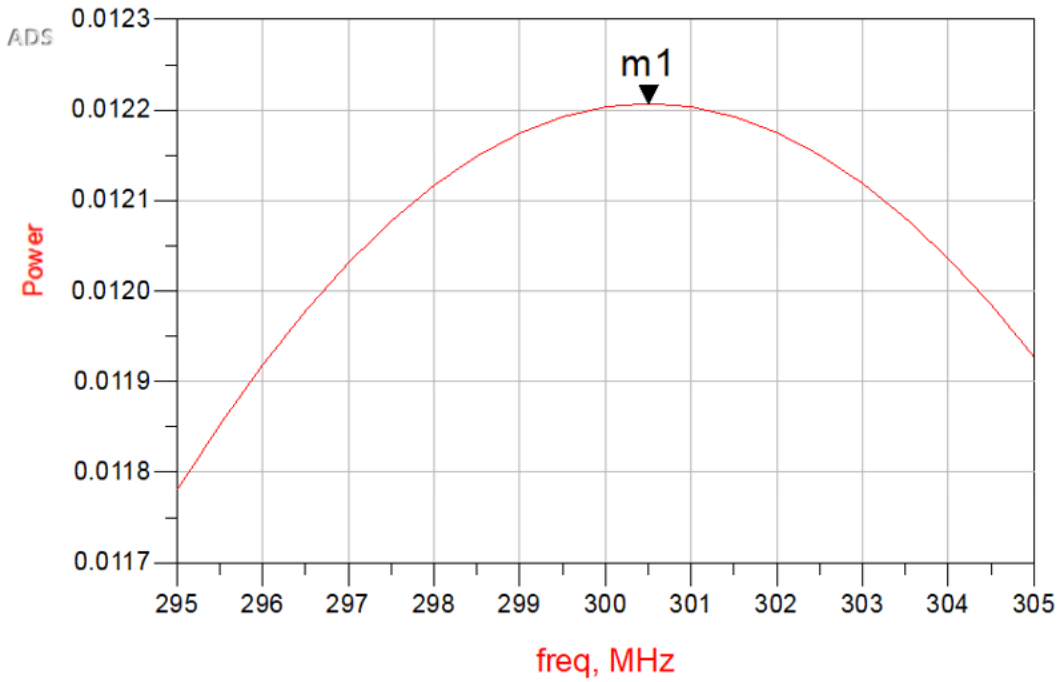

Figure 99: Interrogating antenna 3 matched (power simulation, IA source).

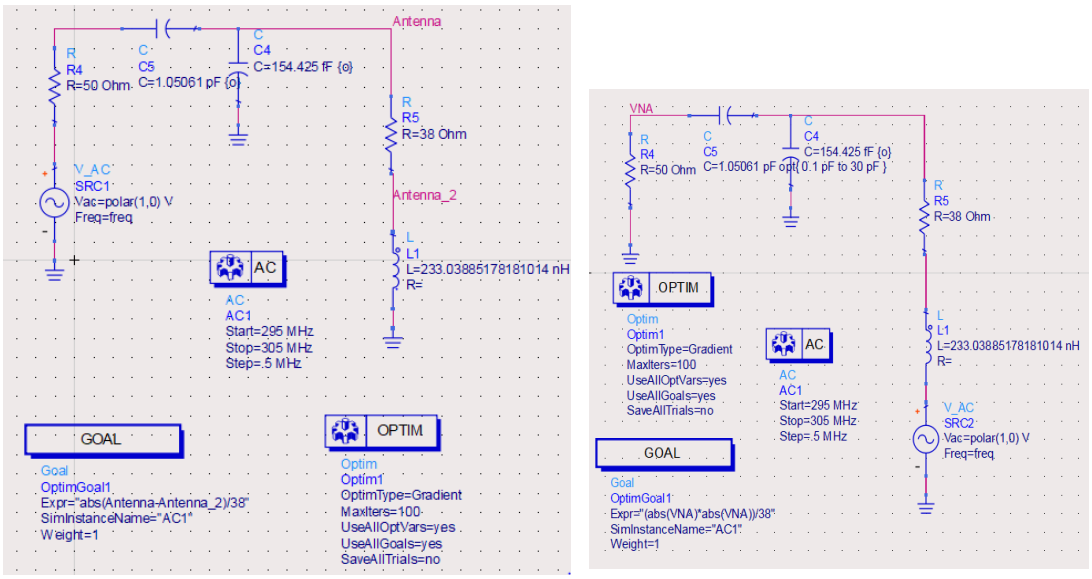

(a) (b)

Figure 100: (a) Interrogating antenna 4 matched schematic (VNA source), (b) interrogating antenna 4 matched schematic (IA source).

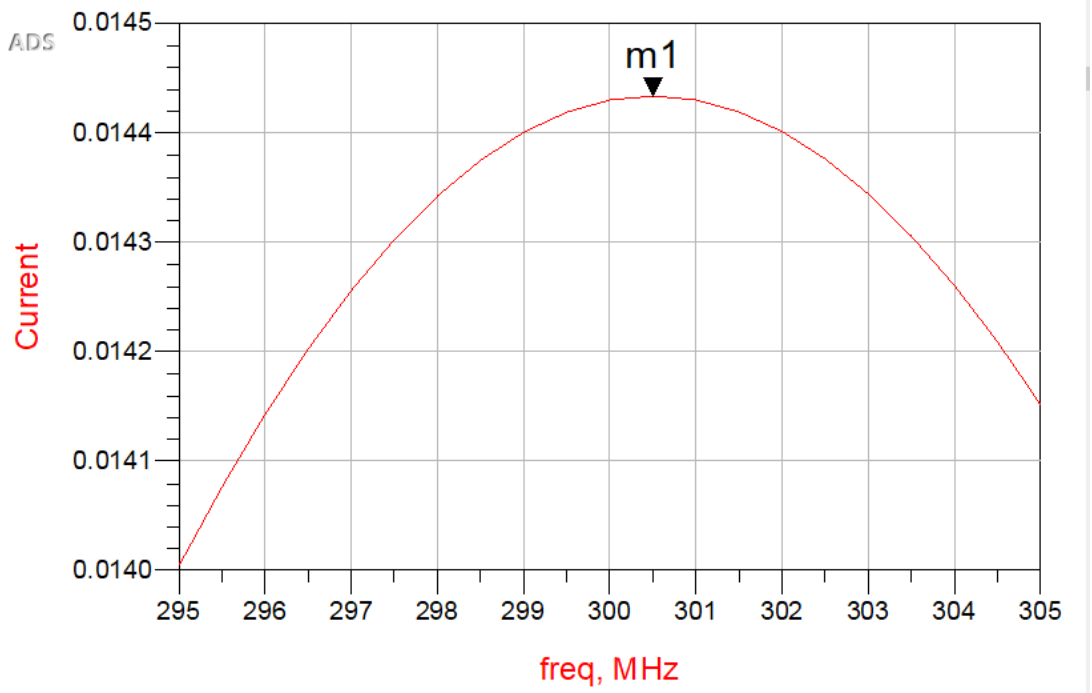

Figure 101: Interrogating antenna 4 matched (current simulation, VNA source).

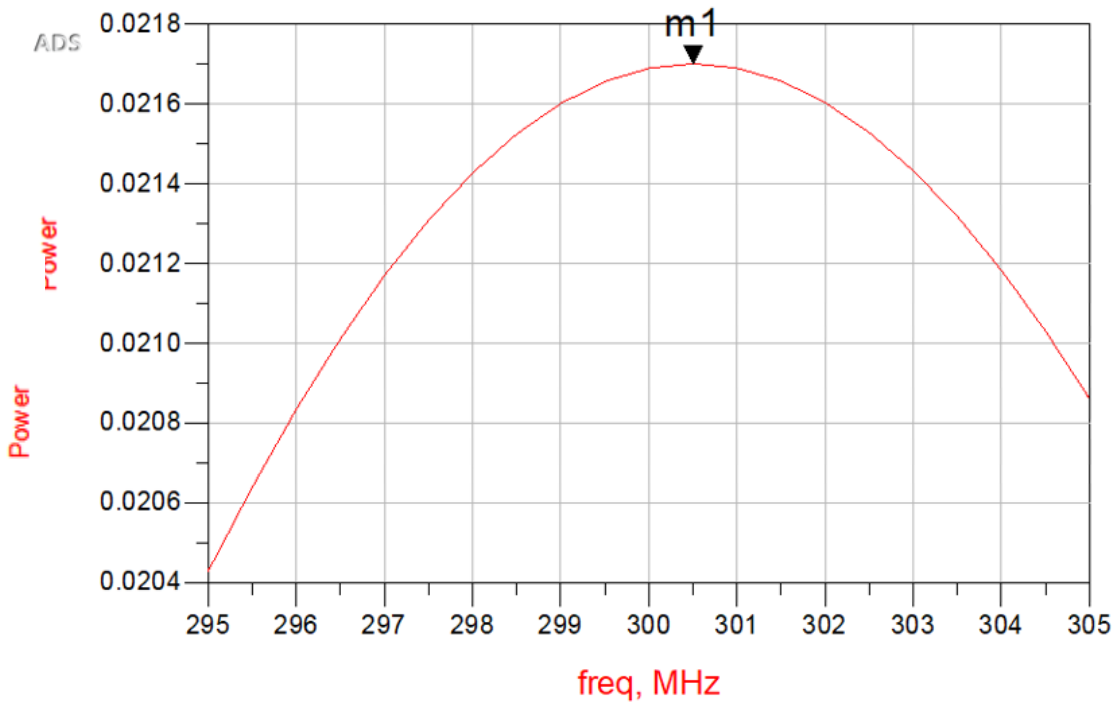

Figure 102: Interrogating antenna 4 matched (power simulation IA source).

APPENDIX E: ADS MATCHING SENSING ANTENNA SIMULATION RESULTS

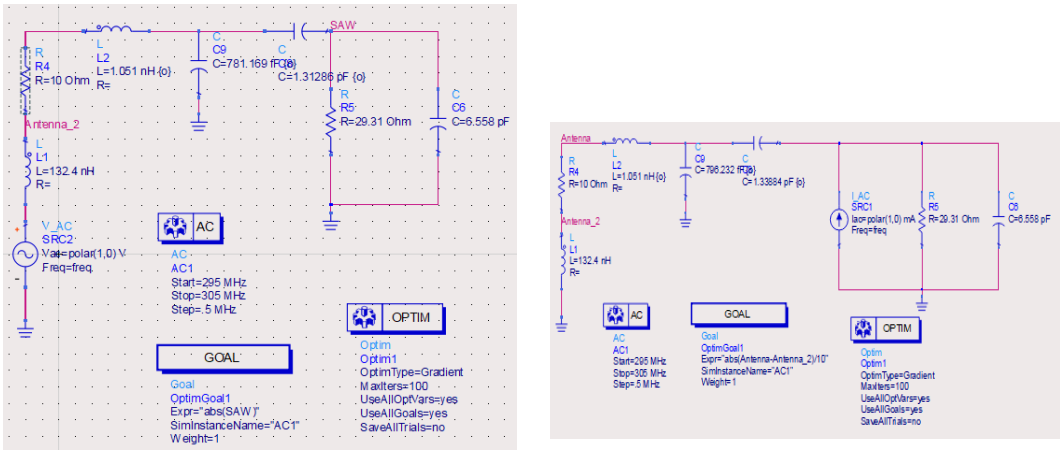

(a) (b)

Figure 103: (a) New sensing antenna T circuit configuration 1, (SA source), (b) new sensing antenna T circuit configuration 1 (SAW source).

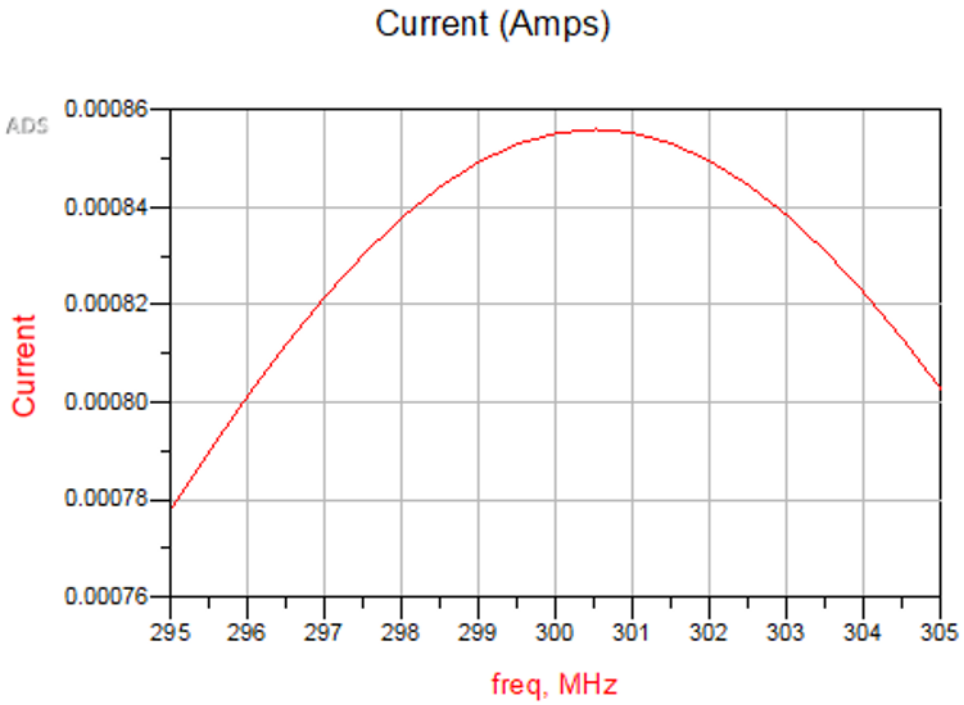

Figure 104: New sensing antenna T circuit configuration 1 (current simulation, SAW source).

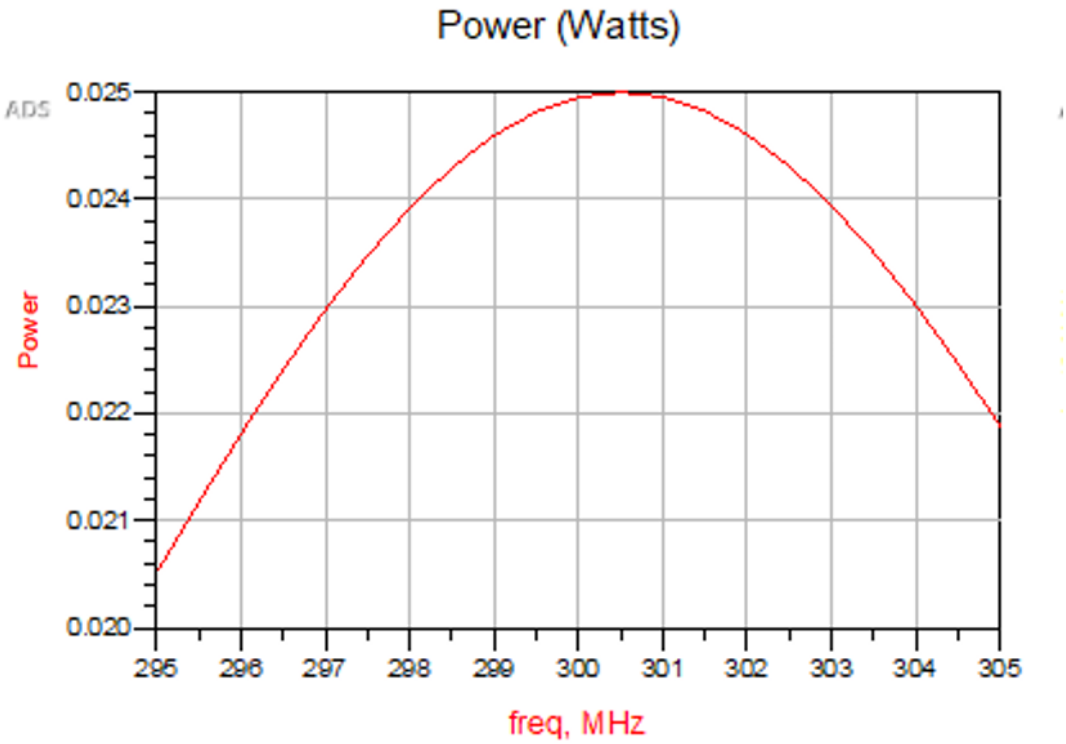

Figure 105: New sensing antenna T circuit configuration 1 (power simulation, SA source).

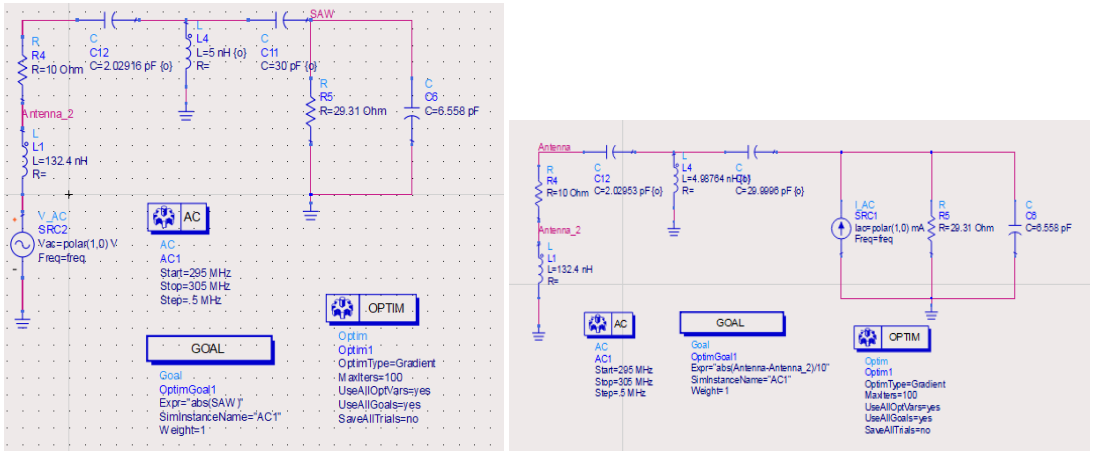

(a) (b)

Figure 106: (a) New sensing antenna T circuit configuration 2, (SA source), (b) new sensing antenna T circuit configuration 2 (SAW source).

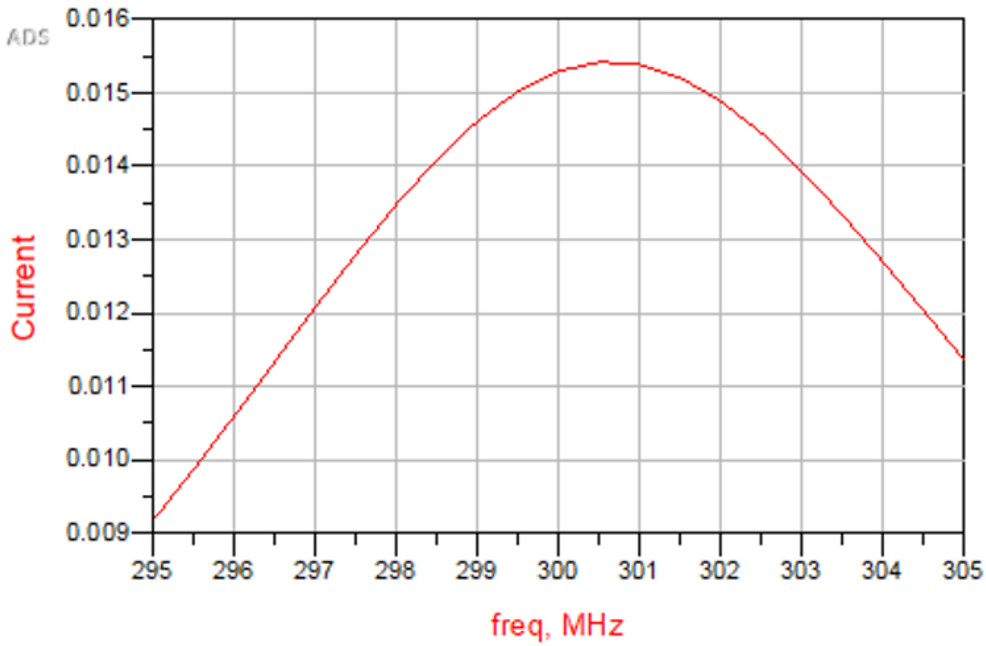

Figure 107: New sensing antenna T circuit configuration 2 (current simulation, SAW source).

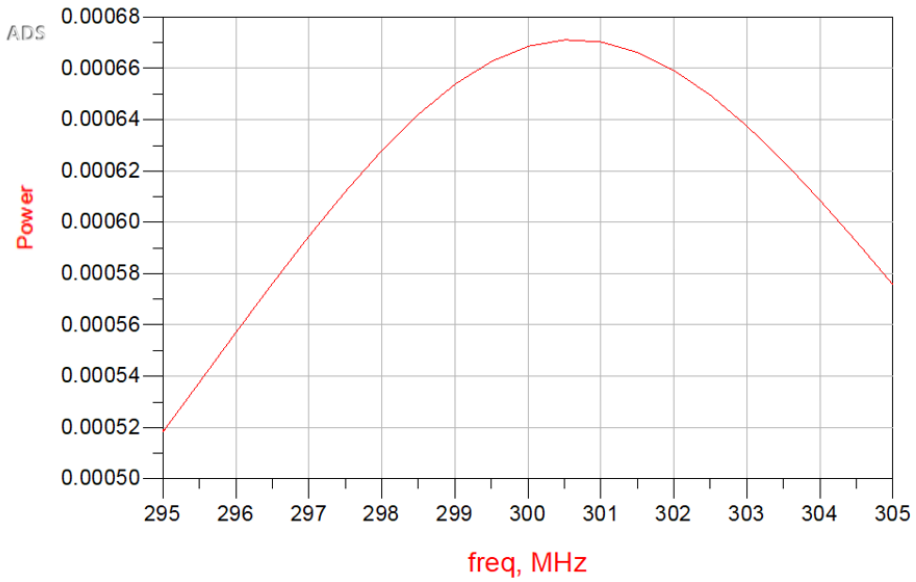

Figure 108: New sensing antenna T circuit configuration 2 (power simulation, SA source).

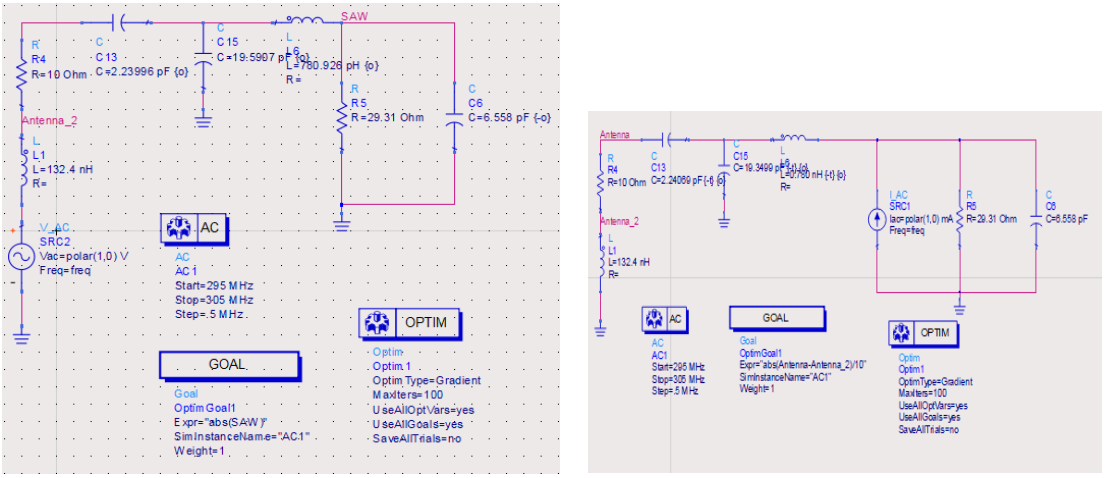

(a) (b)

Figure 109: (a) New sensing antenna T circuit configuration 3, (SA source), (b) new sensing antenna T circuit configuration 3 (SAW source).

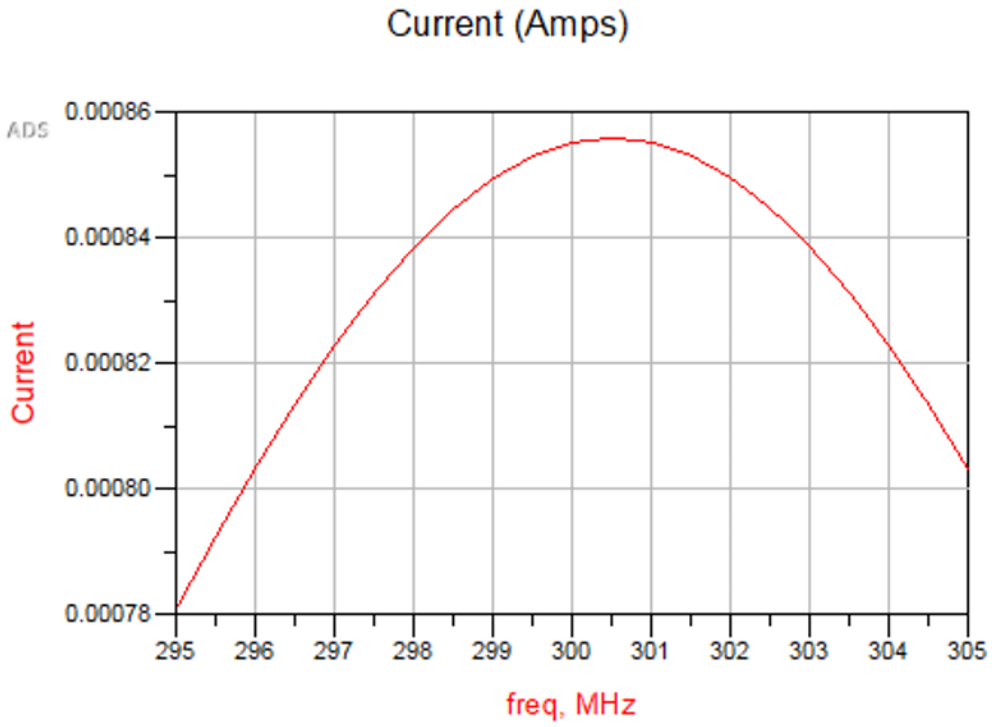

Figure 110: New sensing antenna T circuit configuration 3 (current simulation, SAW source).

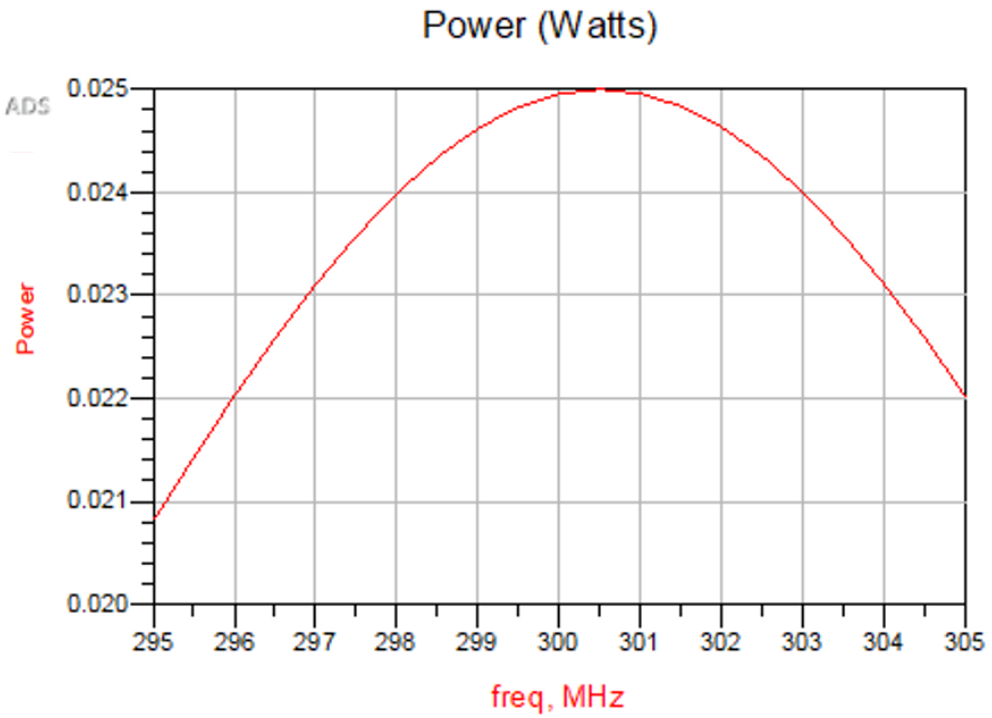

Figure 111: New sensing antenna T circuit configuration 3 (power simulation, SA source).

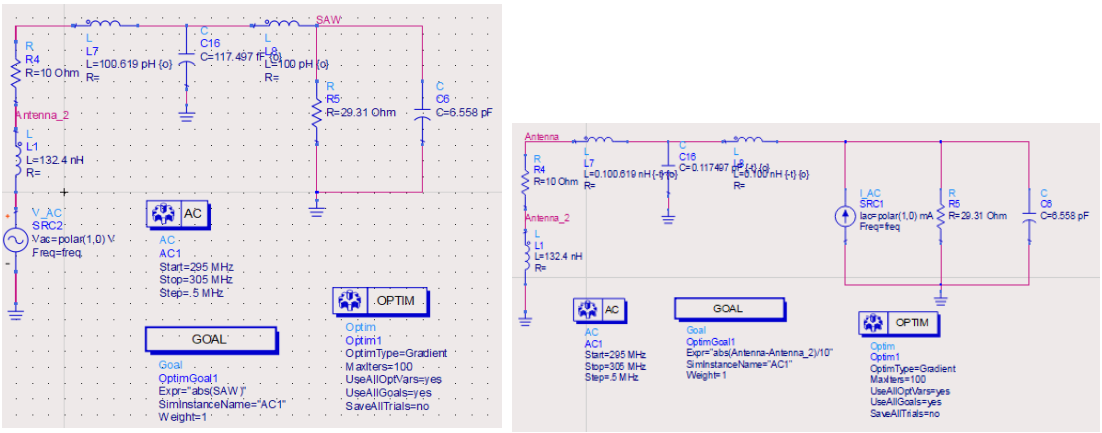

(a) (b)

Figure 112: (a) New sensing antenna T circuit configuration 4, (SA source), (b) new sensing antenna T circuit configuration 4 (SAW source).

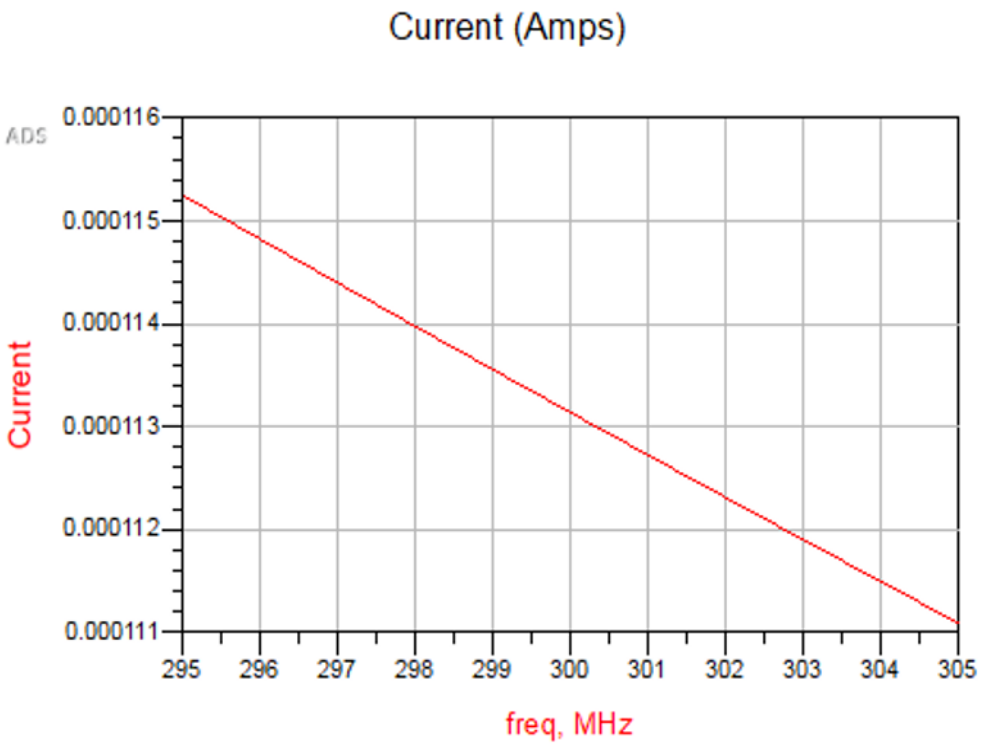

Figure 113: New sensing antenna T circuit configuration 4 (current simulation, SAW source).

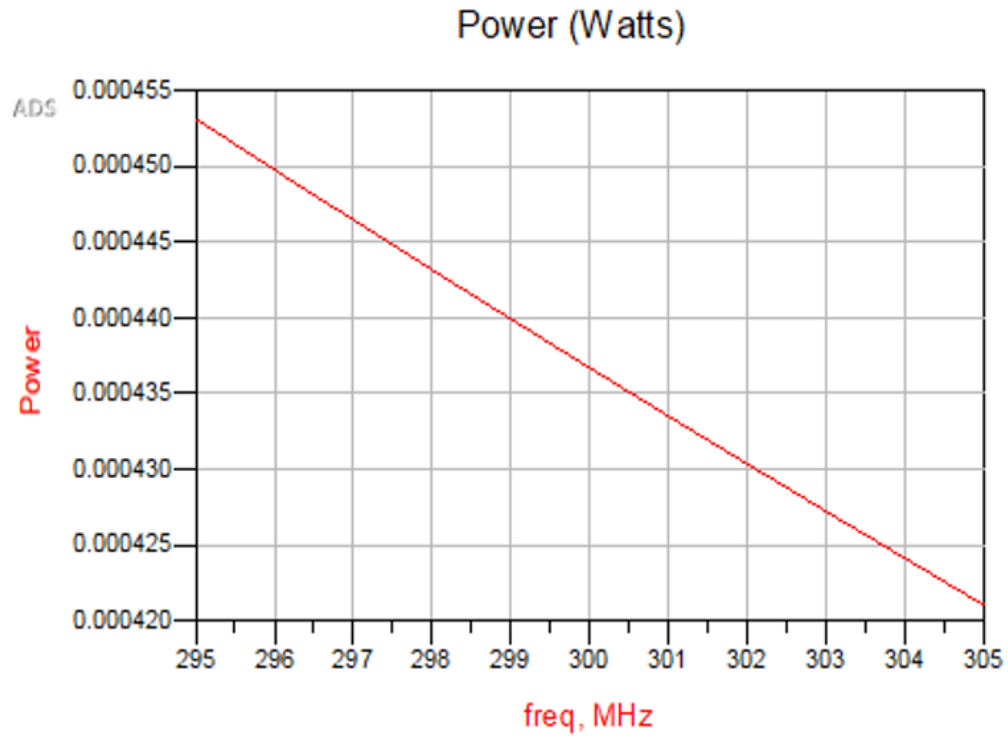

Figure 114: New sensing antenna T circuit configuration 4 (power simulation, SA source).

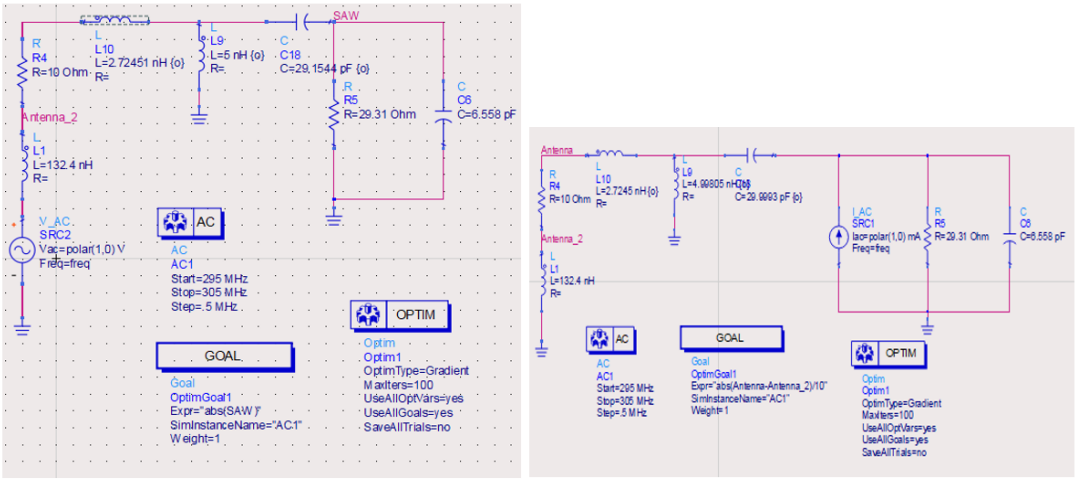

(a) (b)

Figure 115: (a) New sensing antenna T circuit configuration 5, (SA source), (b) new sensing antenna T circuit configuration 5 (SAW source).

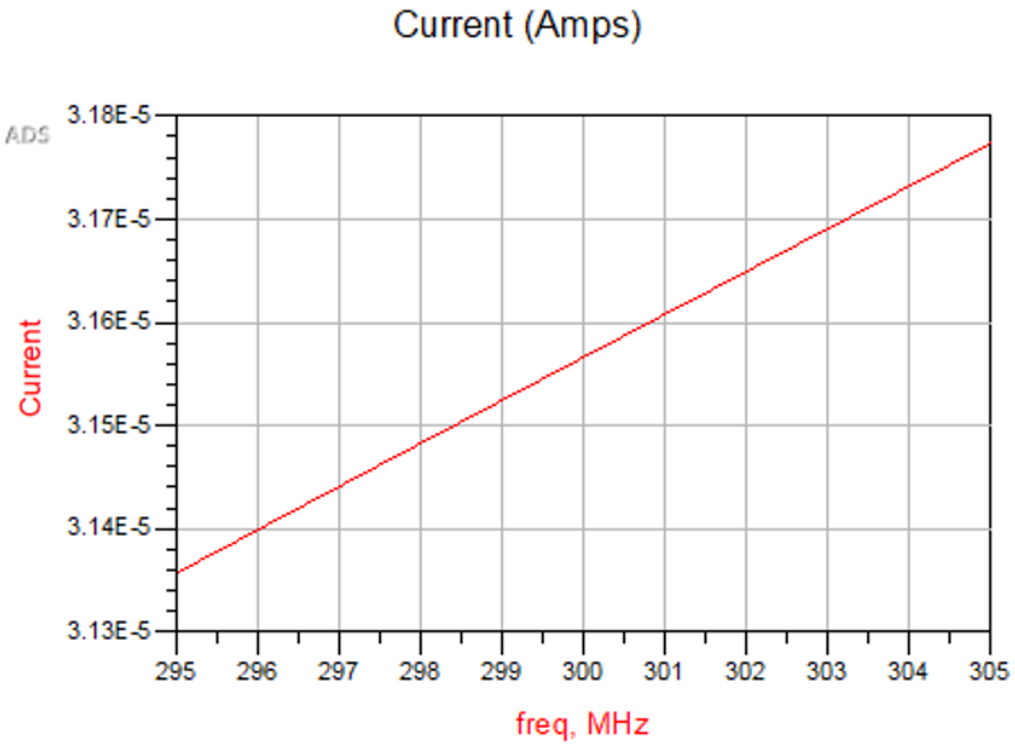

Figure 116: New sensing antenna T circuit configuration 5 (current simulation, SAW source).

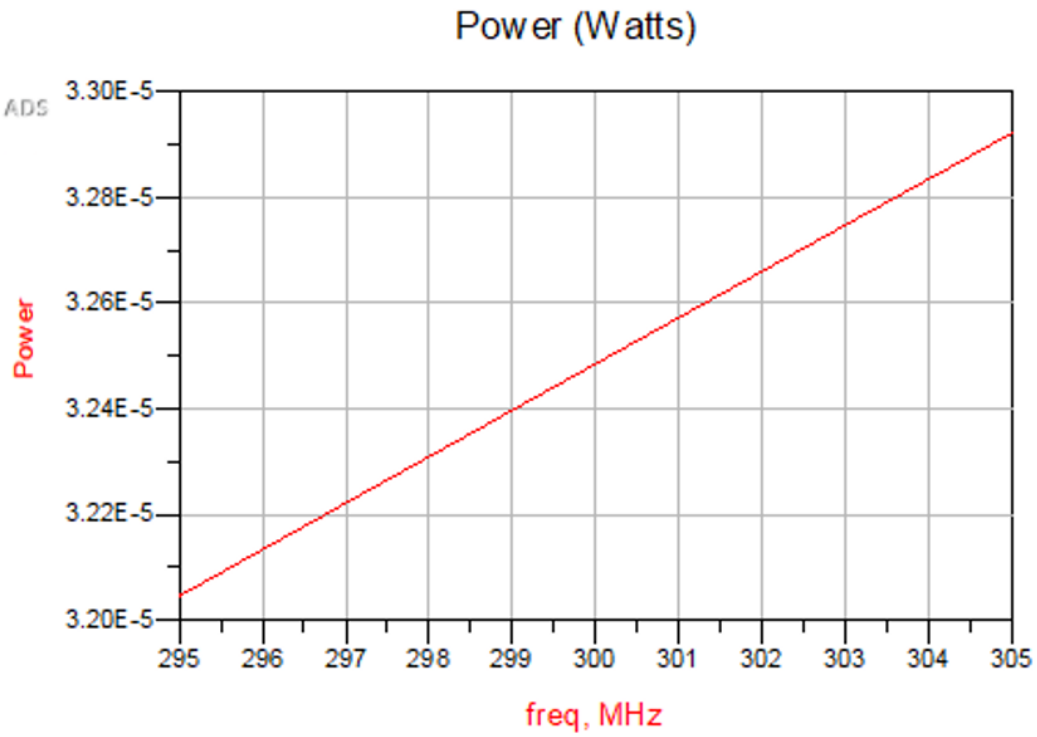

Figure 117: New sensing antenna T circuit configuration 5 (power simulation, SA source).

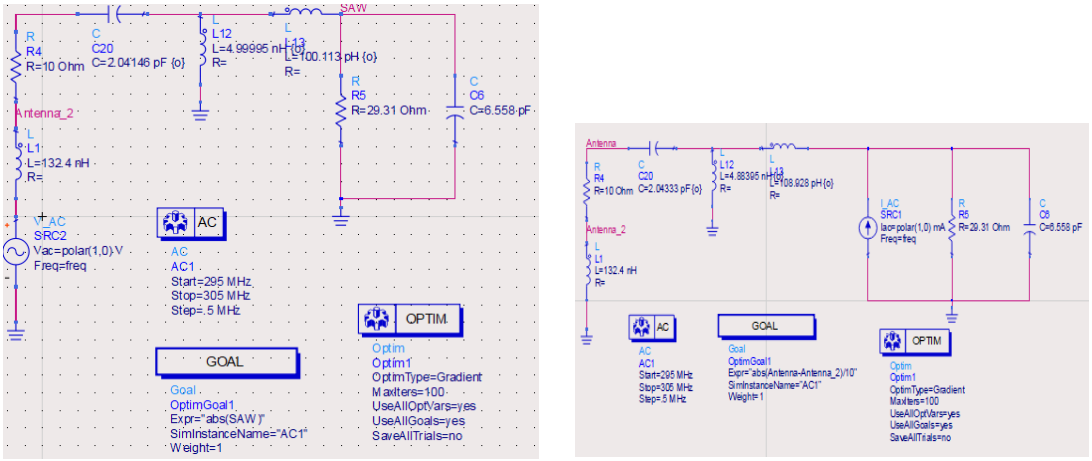

(a) (b)

Figure 118: (a) New sensing antenna T circuit configuration 6, (SA source), (b) new sensing antenna T circuit configuration 6 (SAW source).

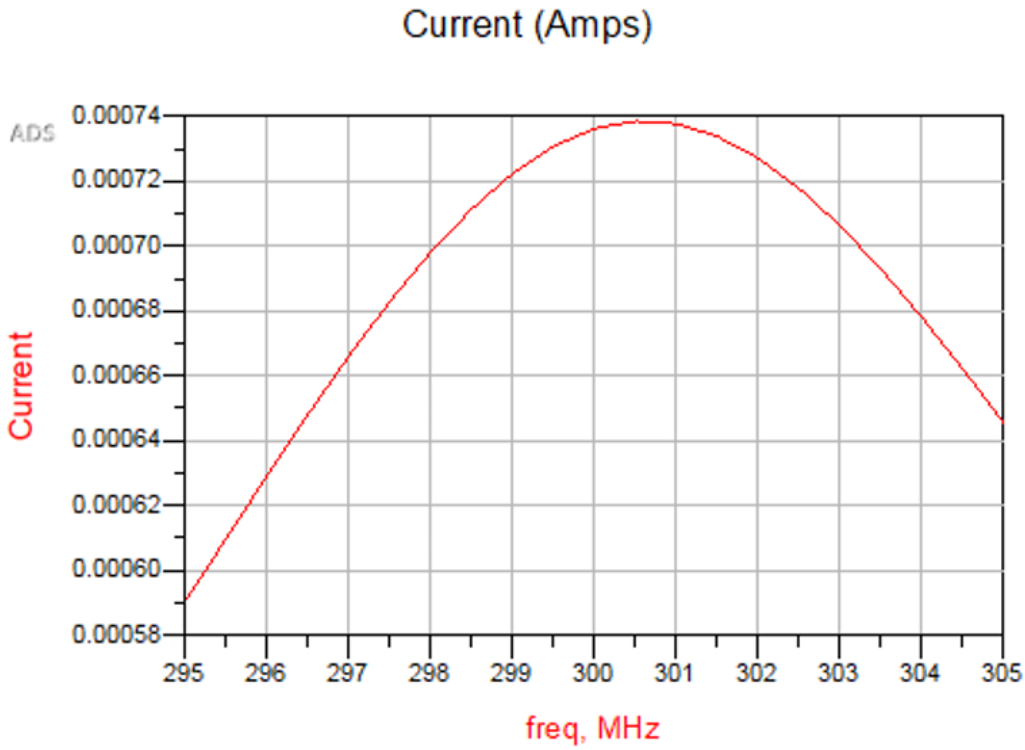

Figure 119: New sensing antenna T circuit configuration 5 current (SAW source).

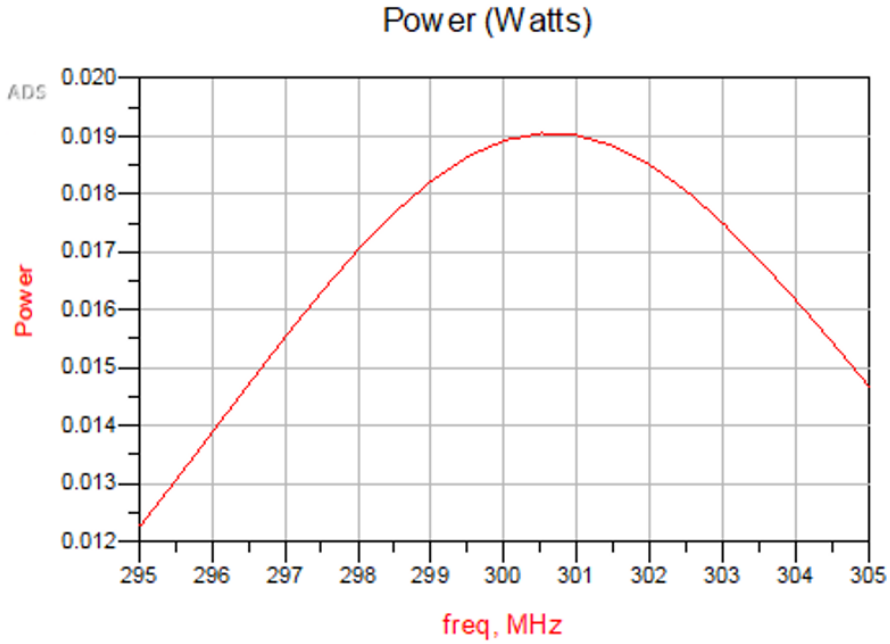

Figure 120: New sensing antenna T circuit configuration 5 (power simulation, SA source).

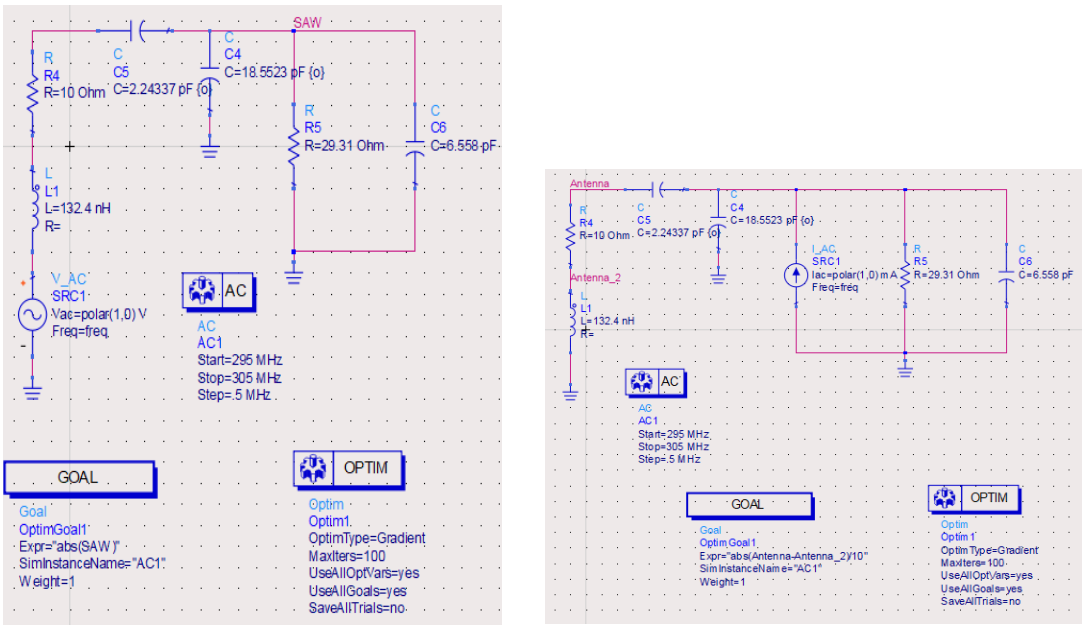

(a) (b)

Figure 121: (a) New sensing antenna L circuit configuration 1, (SA source), (b) new sensing antenna L circuit configuration 1 (SAW Source).

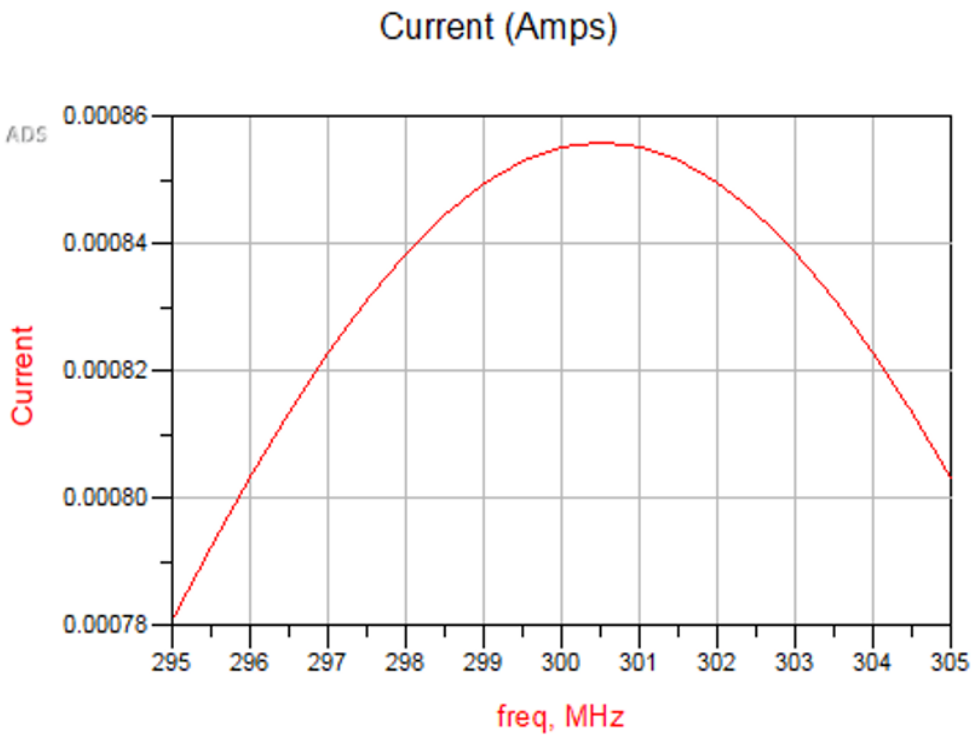

Figure 122: New sensing antenna L circuit configuration 1 (current simulation, SAW source).

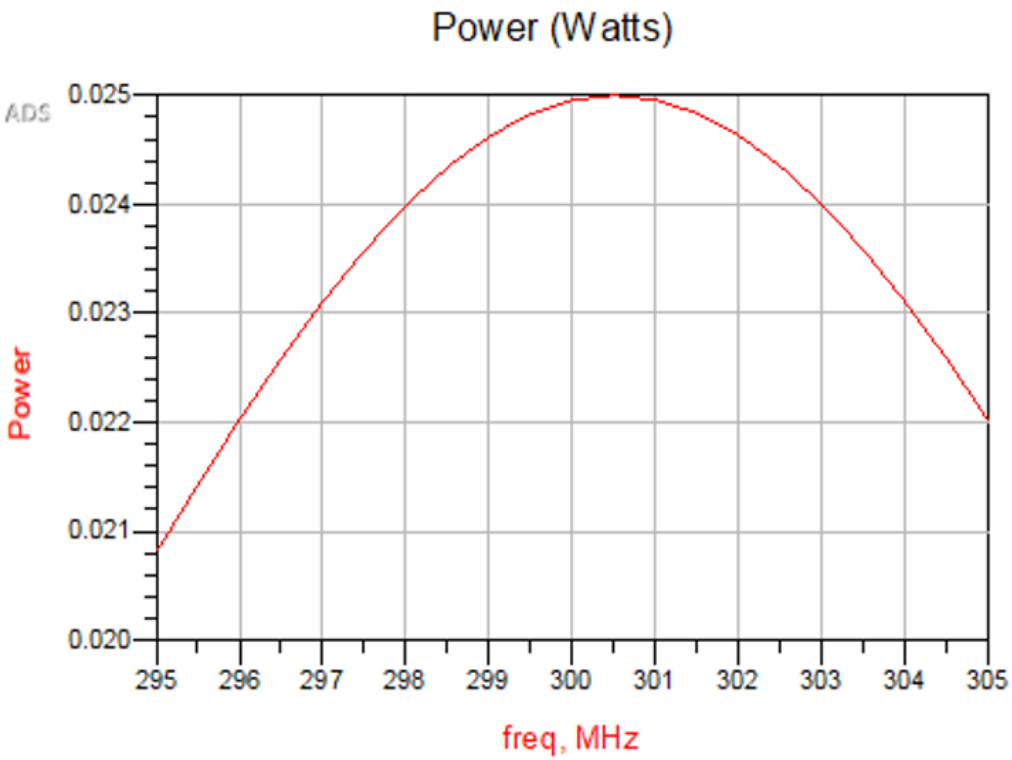

Figure 123: New sensing antenna L circuit configuration 1 (power simulation, SA source).

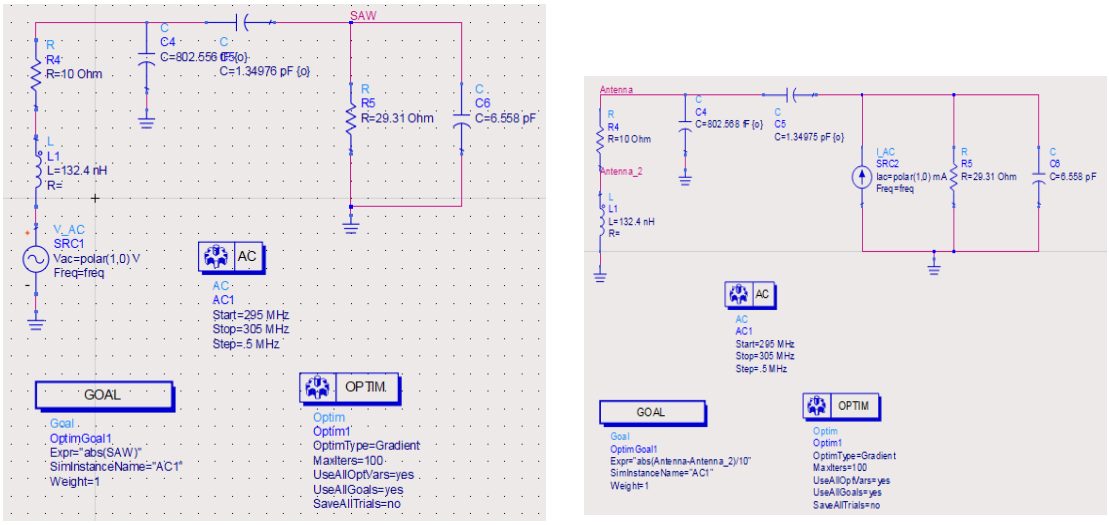

(a) (b)

Figure 124: (a) New sensing antenna L circuit configuration 2, (SA source), (b) new sensing antenna L circuit configuration 2 (SAW source).

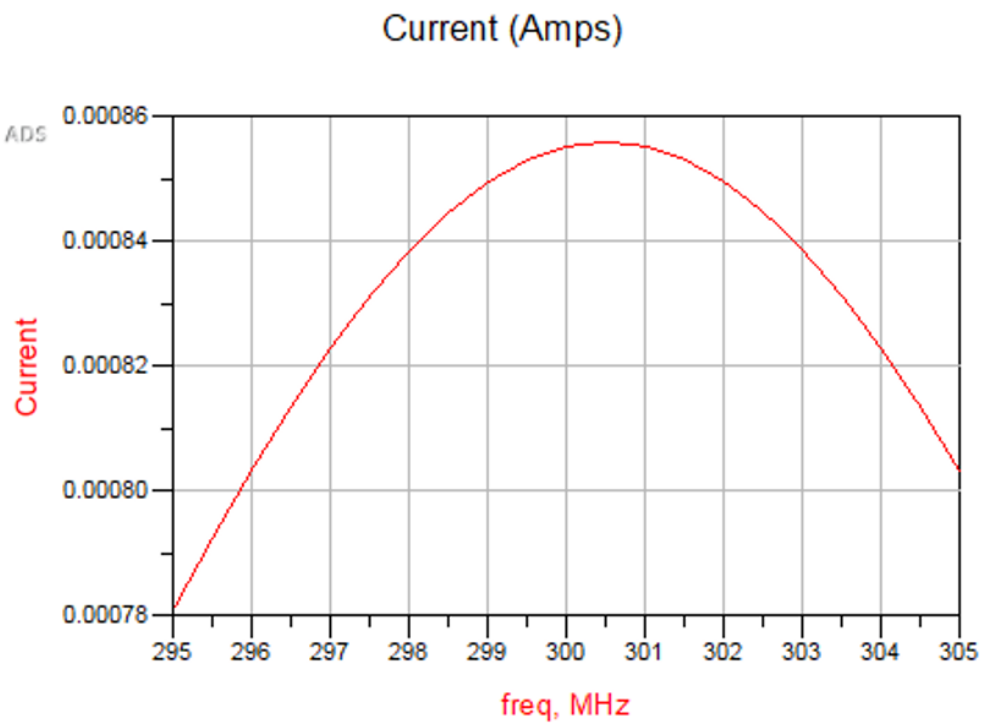

Figure 125: New sensing antenna L circuit configuration 2 (current simulation, SAW source).

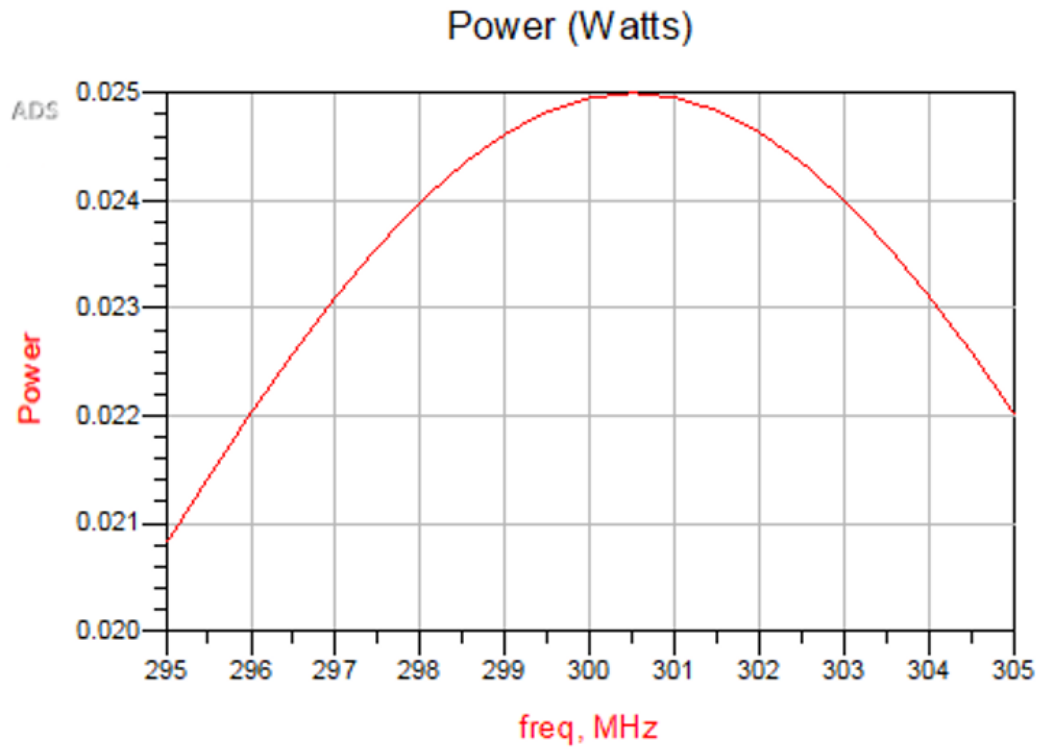

Figure 126: New sensing antenna L circuit configuration 2 (power simulation, SA source).

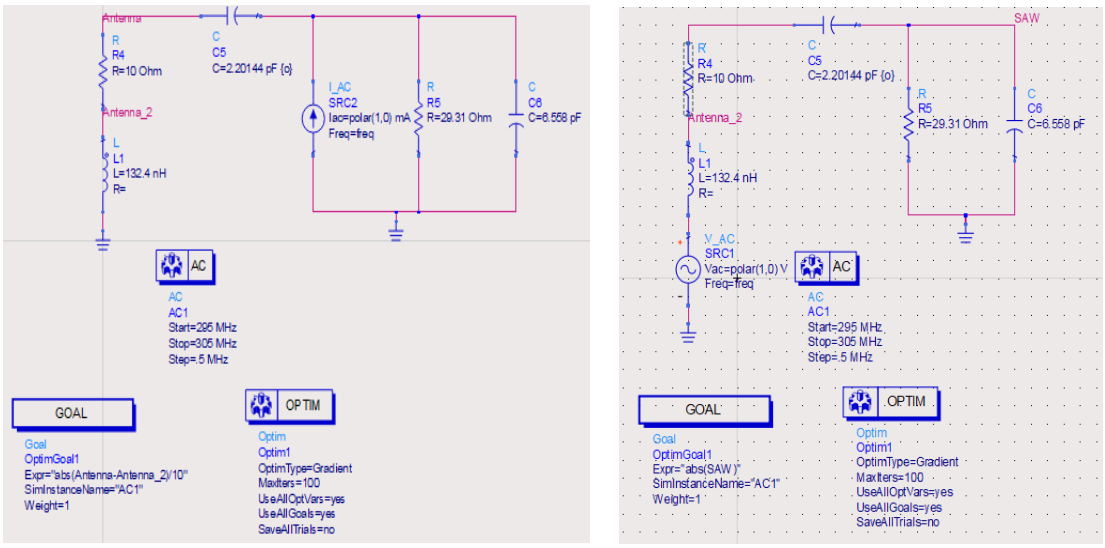

(a) (b)

Figure 127: (a) New sensing antenna series capacitance tuning, (SA source), (b) New sensing antenna series capacitance tuning (SAW Source).

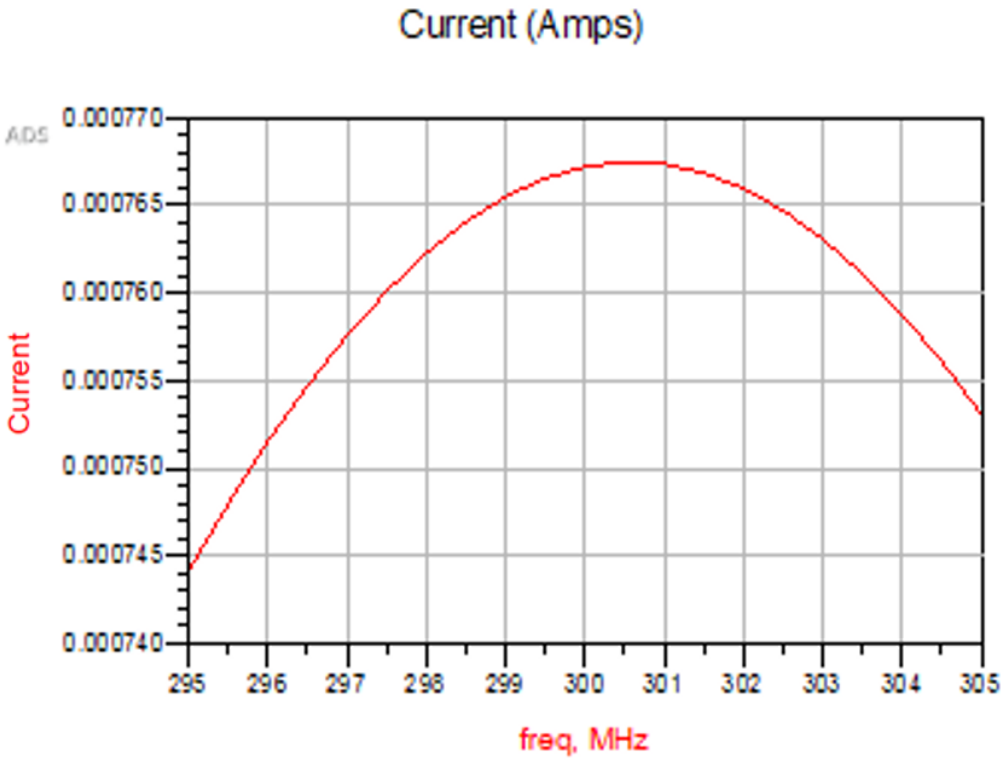

Figure 128: New sensing antenna series capacitance tuning (current simulation, SAW source).

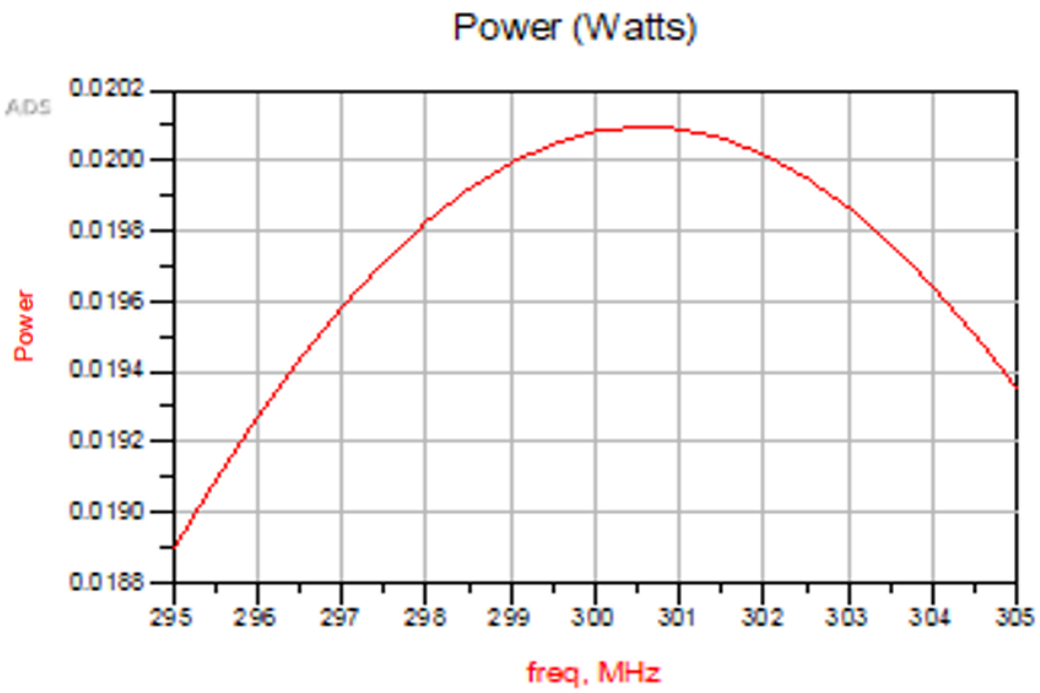

Figure 129: New sensing antenna series capacitance tuning (power simulation, SAW source).

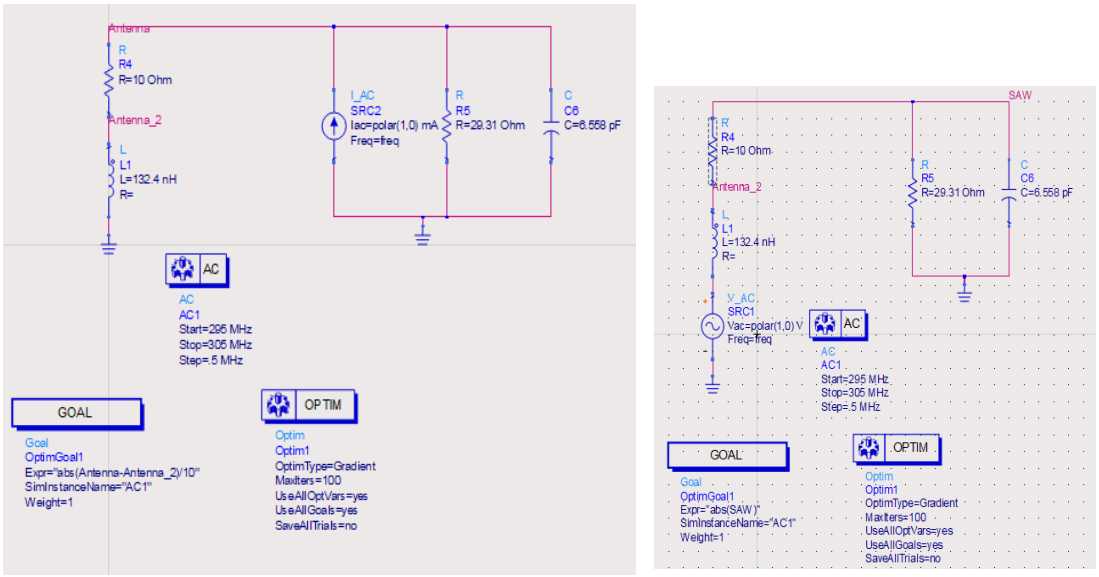

(a) (b)

Figure 130: (a) New sensing antenna no tuning, (SA source), (b) sensing antenna no tuning (SAW source).

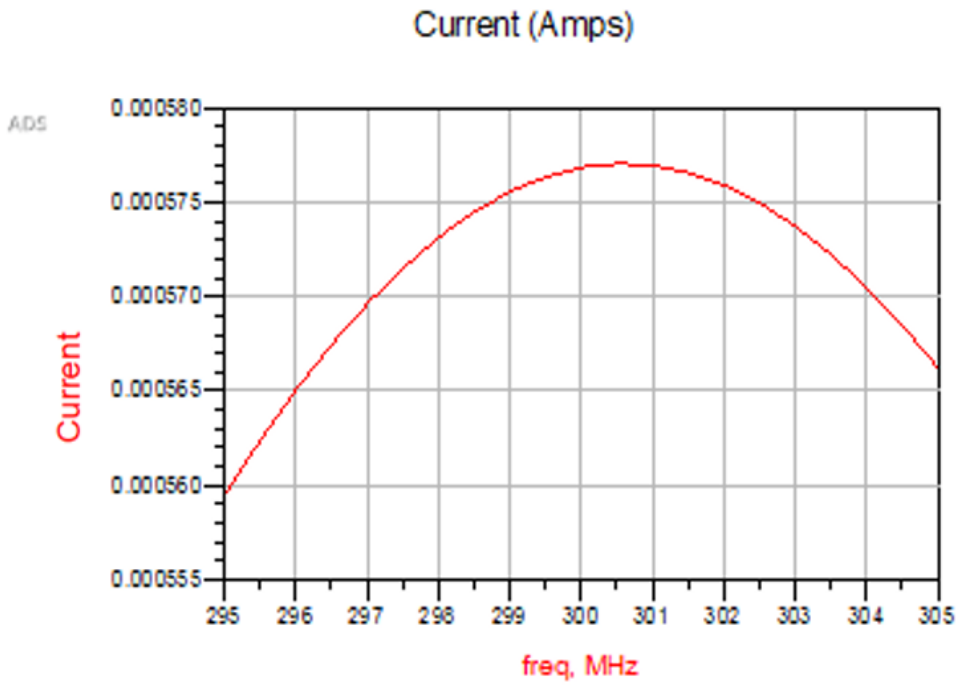

Figure 131: New sensing antenna no tuning (current simulation, SAW source).

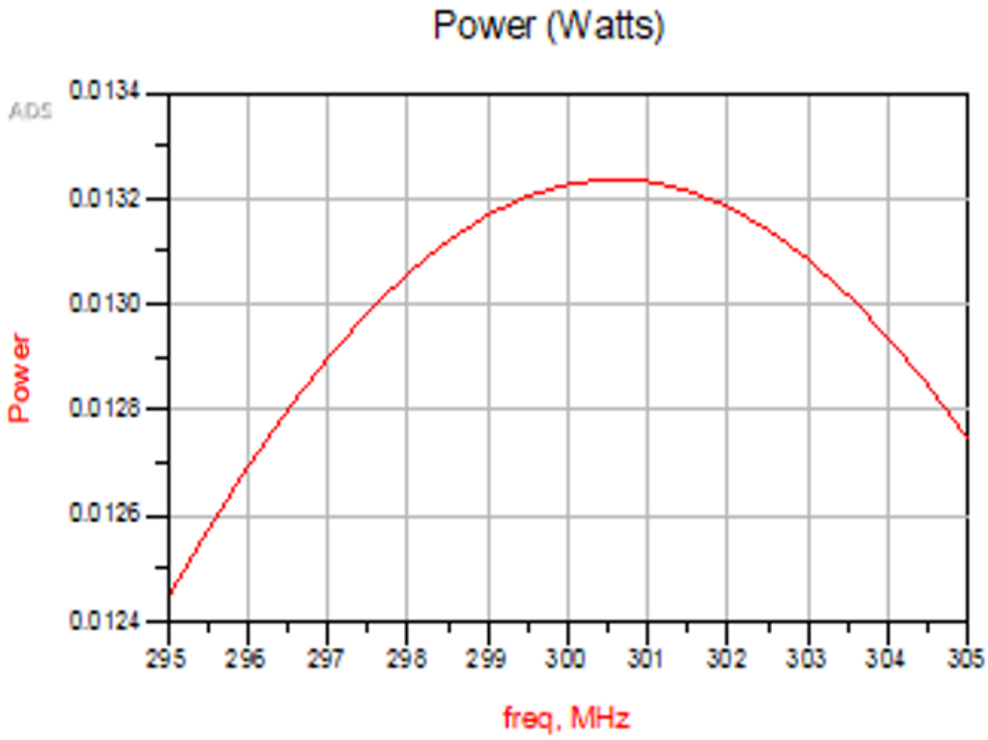

Figure 132: New sensing antenna, no tuning (power simulation SAW source).

APPENDIX F: ADS SERIES CAPACITANCE TUNING FOR 07G SAW IMPEDANCE SIMULATION RESULTS

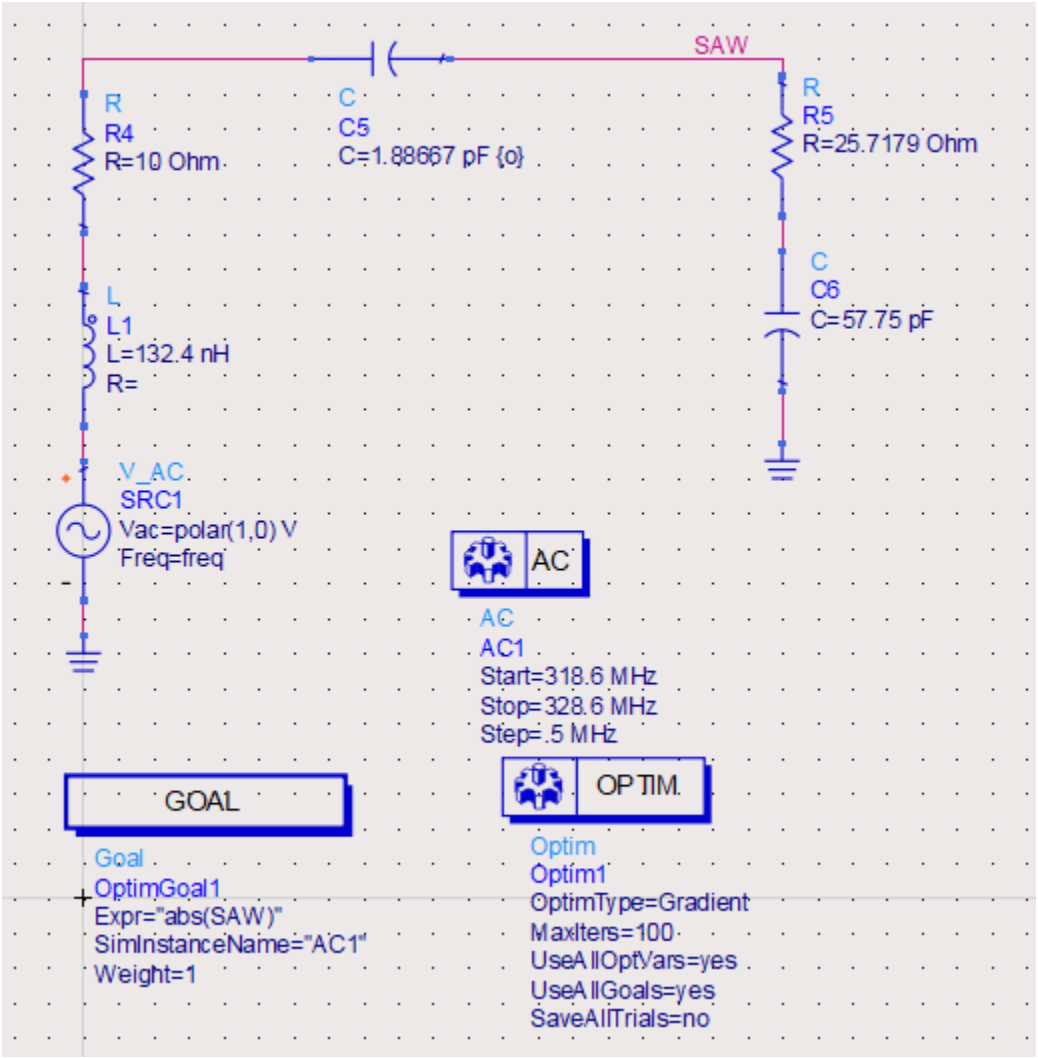

Figure 133: New sensing antenna series capacitance tuning for 07G SAW (SA source).

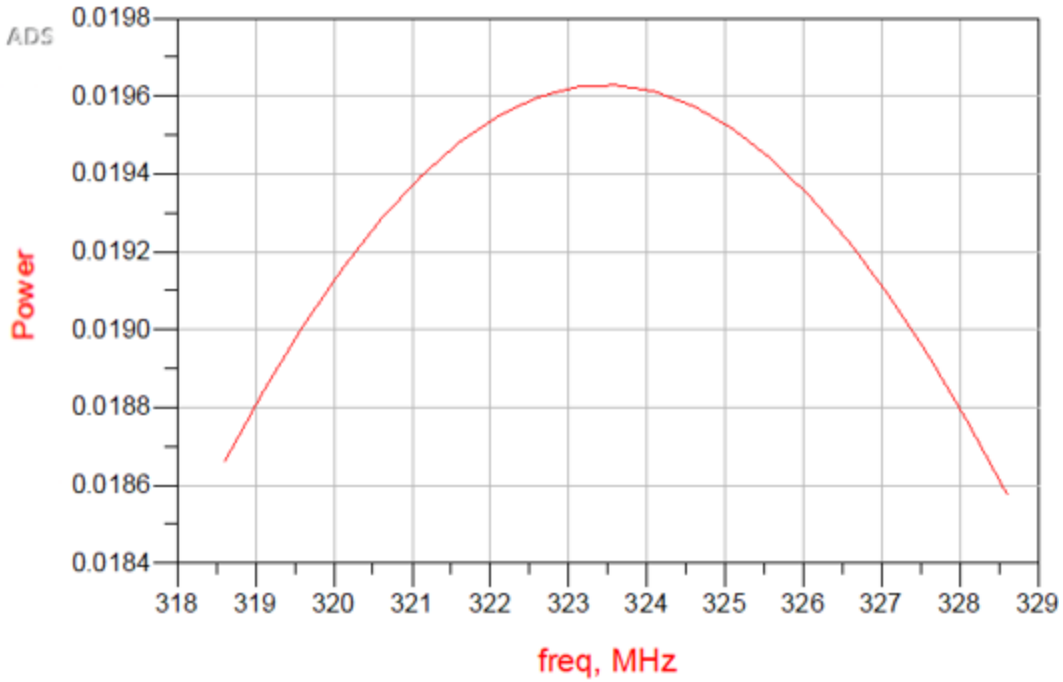

Figure 134: New sensing antenna series capacitance tuning for 07G SAW (power simulation, SA source).

AUTHORS BIOGRAPHY

Nicholas F. Aiken was born in Littleton, New Hampshire on May 19,1997. He was raised in Sheffield, Vermont and graduated from Lyndon Institute in 2015. Majoring in electrical engineering, Nicholas has a minor in mathematics. He is a member of Eta Kappa Nu, Tau Beta Pi, Phi Kappa Phi, and Sigma Phi Epsilon. He has received the Webber Undergraduate Research Scholarship, Lambert ECE Scholarship, received first place in undergraduate engineering at University of Maine's 2019 Student Research Symposium, and was a candidate for the University of Maine Valedictorian or Salutatorian.

Upon graduation, Nicholas will work as a technical engineer at Procter and Gamble in Auburn, Maine. Nicholas aspires to pursue an advanced degree in Electrical and Computer Engineering in the future.